Stability and Control Estimation Flight Test Results for the SR-71 Aircraft With Externally Mounted Experiments

Timothy R. Moes and Kenneth Iliff
NASA Dryden Flight Research Center
Edwards, California

The NASA STI Program Office…in Profile

Since its founding, NASA has been dedicated to the advancement of aeronautics and space science. The NASA Scientific and Technical Information (STI) Program Office plays a key part in helping NASA maintain this important role.

The NASA STI Program Office is operated by Langley Research Center, the lead center for NASA's scientific and technical information. The NASA STI Program Office provides access to the NASA STI Database, the largest collection of aeronautical and space science STI in the world. The Program Office is also NASA's institutional mechanism for disseminating the results of its research and development activities. These results are published by NASA in the NASA STI Report Series, which includes the following report types:

- TECHNICAL PUBLICATION. Reports of completed research or a major significant phase of research that present the results of NASA programs and include extensive data or theoretical analysis. Includes compilations of significant scientific and technical data and information deemed to be of continuing reference value. NASA's counterpart of peer-reviewed formal professional papers but has less stringent limitations on manuscript length and extent of graphic presentations.

- TECHNICAL MEMORANDUM. Scientific and technical findings that are preliminary or of specialized interest, e.g., quick release reports, working papers, and bibliographies that contain minimal annotation. Does not contain extensive analysis.

- CONTRACTOR REPORT. Scientific and technical findings by NASA-sponsored contractors and grantees.

- CONFERENCE PUBLICATION. Collected papers from scientific and technical conferences, symposia, seminars, or other meetings sponsored or cosponsored by NASA.

- SPECIAL PUBLICATION. Scientific, technical, or historical information from NASA programs, projects, and mission, often concerned with subjects having substantial public interest.

- TECHNICAL TRANSLATION. English-language translations of foreign scientific and technical material pertinent to NASA's mission.

Specialized services that complement the STI Program Office's diverse offerings include creating custom thesauri, building customized databases, organizing and publishing research results…even providing videos.

For more information about the NASA STI Program Office, see the following:

- Access the NASA STI Program Home Page at *http://www.sti.nasa.gov*

- E-mail your question via the Internet to help@sti.nasa.gov

- Fax your question to the NASA Access Help Desk at (301) 621-0134

- Telephone the NASA Access Help Desk at (301) 621-0390

- Write to:
  NASA Access Help Desk
  NASA Center for AeroSpace Information
  7121 Standard Drive
  Hanover, MD 21076-1320
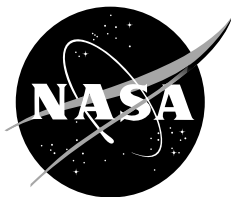
Stability and Control Estimation Flight Test Results for the SR-71 Aircraft With Externally Mounted Experiments

Timothy R. Moes and Kenneth Iliff
NASA Dryden Flight Research Center
Edwards, California

June 2002

Available from the following:

CONTENTS

TABLES

FIGURES

ABSTRACT

A maximum-likelihood output-error parameter estimation technique is used to obtain stability and control derivatives for the NASA Dryden Flight Research Center SR-71A airplane and for configurations that include experiments externally mounted to the top of the fuselage. This research is being done as part of the envelope clearance for the new experiment configurations. Flight data are obtained at speeds ranging from Mach 0.4 to Mach 3.0, with an extensive amount of test points at approximately Mach 1.0. Pilot-input pitch and yaw-roll doublets are used to obtain the data. This report defines the parameter estimation technique used, presents stability and control derivative results, and compares the derivatives for the three configurations tested. The experimental configurations studied generally show acceptable stability, control, trim, and handling qualities throughout the Mach regimes tested. The reduction of directional stability for the experimental configurations is the most significant aerodynamic effect measured and identified as a design constraint for future experimental configurations. This report also shows the significant effects of aircraft flexibility on the stability and control derivatives.

NOMENCLATURE

a_n normal acceleration (positive up), ft/sec^2

a_y lateral acceleration (positive toward the right), ft/sec^2

b reference span, 56.7 ft

BL butt line, in.

c mean aerodynamic chord, 37.7 ft

CG center of gravity, percent c

C_l coefficient of rolling moment

C_{l_b} rolling moment bias, linear coefficient estimate for $\beta = 0°$

C_{l_p} derivative of rolling moment due to nondimensional roll rate, $\partial C_l / \partial (pb/2VR)$, rad^{-1}

C_{l_r} derivative of rolling moment due to nondimensional yaw rate, $\partial C_l / \partial (rb/2VR)$, rad^{-1}

C_{l_β} derivative of rolling moment due to sideslip, $\partial C_l / \partial \beta$, deg^{-1}

$C_{l_{\delta_a}}$ derivative of rolling moment due to aileron, $\partial C_l / \partial \delta_a$, deg^{-1}

$C_{l_{\delta_r}}$ derivative of rolling moment due to rudder, $\partial C_l / \partial \delta_r$, deg^{-1}

C_m coefficient of pitching moment

C_{m_b} pitching moment bias, linear coefficient estimate for $\alpha = 0°$

C_{m_q} derivative of pitching moment due to nondimensional pitch rate, $\partial C_m / \partial (qc/2VR)$, rad^{-1}

C_{m_α} derivative of pitching moment due to angle of attack, $\partial C_m / \partial \alpha$, deg^{-1}

$C_{m_{\delta_e}}$ derivative of pitching moment due to elevon, $\partial C_m / \partial \delta_e$, deg^{-1}

C_n coefficient of yawing moment

C_{n_b} yawing moment bias, linear coefficient estimate for $\beta = 0°$

C_{n_p} derivative of yawing moment due to nondimensional roll rate, $\partial C_n / \partial (pb/2VR)$, rad^{-1}

C_{n_r} derivative of yawing moment due to nondimensional yaw rate, $\partial C_n / \partial (rb/2VR)$, rad^{-1}

C_{n_β} derivative of yawing moment due to sideslip, $\partial C_n / \partial \beta$, deg^{-1}

$C_{n_{\delta_a}}$ derivative of yawing moment due to aileron, $\partial C_n / \partial \delta_a$, deg^{-1}

$C_{n_{\delta_r}}$ derivative of yawing moment due to rudder, $\partial C_n / \partial \delta_r$, deg^{-1}

C_N coefficient of normal force

C_{N_b} normal force bias, linear coefficient estimate for $\alpha = 0°$

C_{N_q} derivative of normal force due to nondimensional pitch rate, $\partial C_N / \partial (qc/2VR)$, rad^{-1}

C_{N_α} derivative of normal force due to angle of attack, $\partial C_N / \partial \alpha$, deg^{-1}

$C_{N_{\delta_e}}$ derivative of normal force due to elevon, $\partial C_Y / \partial \delta_e$, deg^{-1}

C_Y coefficient of side force

C_{Y_b} side force bias, linear coefficient estimate for $\beta = 0°$

C_{Y_p} derivative of side force due to nondimensional roll rate, $\partial C_Y / \partial (pb/2VR)$, rad^{-1}

C_{Y_r} derivative of side force due to nondimensional yaw rate, $\partial C_Y / \partial (rb/2VR)$, rad^{-1}

C_{Y_β} derivative of side force due to sideslip, $\partial C_Y / \partial \beta$, deg^{-1}

$C_{Y_{\delta_a}}$ derivative of side force due to aileron, $\partial C_Y / \partial \delta_a$, deg^{-1}

$C_{Y_{\delta_r}}$ derivative of side force due to rudder, $\partial C_Y / \partial \delta_r$, deg^{-1}

F state derivative function

FS fuselage station, in.

g acceleration of gravity, ft/sec^2

G response function

I_x rolling moment of inertia, slug-ft^2

I_{xz} cross product of inertia, slug-ft^2

I_y pitching moment of inertia, slug-ft^2

I_z yawing moment of inertia, slug-ft^2

J(ξ) cost function

2

$KEAS$	equivalent airspeed, knots
LASRE	Linear Aerospike SR-71 Experiment
m	aircraft mass, slug
n_t	number of time history points used
n_z	number of response variables
p	roll rate, deg/sec
$\dot{p}$	roll acceleration, deg/sec^2
PID	parameter identification
q	pitch rate, deg/sec
$\dot{q}$	pitch acceleration, deg/sec^2
$\bar{q}$	dynamic pressure, lbf/ft^2
r	yaw rate, deg/sec
$\dot{r}$	yaw acceleration, deg/sec^2
R	conversion factor, 57.2958 deg/rad
S	SR-71 reference area, 1605 ft^2
SAS	stability augmentation system
t	time, sec
t_i	discrete time point at ith data point
$\mathbf{u}$	measured control input vector
V	true airspeed, ft/sec
w	weight, lb
W	response weighting matrix (used in the cost function)
WL	water line, in.
$\mathbf{x}$	state vector
$\dot{x}$	time derivative of the state vector
x_{a_n}	normal accelerometer location, ft aft of the CG
x_{a_y}	lateral accelerometer location, ft aft of the CG
x_α	angle-of-attack measurement location, ft aft of the CG

x_β	angle-of-sideslip measurement location, ft aft of the *CG*
y_{a_n}	normal accelerometer location, ft to the right of the *CG*
y_{a_y}	lateral accelerometer location, ft to the right of the *CG*
z	response vector (measurement vector)
z_{a_n}	normal accelerometer location, ft above the *CG*
z_{a_y}	lateral accelerometer location, ft above the *CG*
z_β	angle-of-sideslip measurement location, ft above the *CG*
α	wing reference plane angle of attack, deg
$\dot{\alpha}$	time rate of change of angle of attack, deg/sec
β	angle of sideslip, deg
$\dot{\beta}$	time rate of change of angle of sideslip, deg/sec
δ	control-surface deflection, deg
δ_a	aileron deflection, deg
δ_e	elevon deflection, deg
δ_r	rudder deflection, deg
η_a	lateral stick position, in.
η_e	longitudinal stick position, in.
θ	pitch angle, deg
$\dot{\theta}$	time rate of change of pitch angle, deg/sec
ξ	stability and control derivative parameter vector
ϕ	roll angle, deg
$\dot{\phi}$	time rate of change of roll angle, deg/sec
*	transpose
~	estimated response parameter

4

INTRODUCTION

A Mach 3.2–capable SR-71 airplane has completed a series of flight tests at the NASA Dryden Flight Research Center (Edwards, California). The series was performed to determine stability and control characteristics of the baseline configuration (fig. 1) and two configurations with experiments mounted on top of the fuselage. NASA Dryden previously modified the internal structure of one of its SR-71 aircraft to accommodate experiments weighing a maximum of 14,500 lb for high-speed flight research of new and unique concepts. The Linear Aerospike SR-71 Experiment (LASRE) is one example of such flight research (ref. 1) and consisted of an approximately 14,140-lb payload weight that was mounted to the SR-71 upper fuselage (fig. 2). The LASRE configuration obtained flight data at speeds to a maximum of Mach 1.75.

After the termination of the LASRE program, a four-flight test bed configuration flight program (ref. 2) was conducted to a maximum speed of Mach 3.0. The test bed configuration consists of the LASRE pod without the half-span lifting-body model (fig. 3). Because of the large size of the LASRE and test bed configurations, an incremental stability and control flight envelope expansion became necessary to ensure safe flying characteristics. The envelope expansion includes pilot-input doublet maneuvers for parameter identification (PID) of stability and control derivatives at increasing Mach numbers. Both pitch doublets and yaw-roll doublets have been performed at each Mach number condition. Data also have been obtained at low and high equivalent airspeeds to determine the effect of aircraft flexibility on the stability and control derivatives. A maximum-likelihood output-error program (ref. 3) has been used postflight to estimate stability and control derivatives from the flight data. This report presents flight-determined stability and control results for the SR-71 baseline, LASRE, and test bed configurations. Stability and control derivative predictions from the SR-71 aerodynamic model (ref. 4) also are presented for the baseline configuration.

VEHICLE DESCRIPTION

An SR-71A airplane (Lockheed Martin Corporation, Palmdale, California) is used as the carrier vehicle for the LASRE and test bed configurations. Stability and control data have been obtained for the baseline, LASRE, and test bed configurations that are described in this section. Because the SR-71 aircraft is fairly flexible, aeroelastic effects on the stability and control derivatives also have been obtained. Control surfaces are not modified for the LASRE and test bed configurations.

Baseline Configuration

The SR-71A aircraft is a two-place, twin-engine aircraft capable of cruising at speeds to a maximum of Mach 3.2 and altitudes to a maximum of 85,000 ft. The aircraft is powered by two 34,000-lbf thrust-class J58 (Pratt & Whitney, West Palm Beach, Florida) afterburning turbojet engines. Approximately 5 percent of thrust enhancement is obtained on both engines by increasing the turbine exhaust gas temperature and rotor speed (ref. 2). The engine is aligned with the wing reference plane, which has a 1.2-deg nosedown incidence compared to the fuselage centerline reference plane. The angle

of attack used herein is referenced to the wing reference plane. The engine inlet is canted slightly down and inward to obtain low local flow angles.

Control-surface actuators are powered using two independent hydraulic systems. Twin all-moving, tetrahedrally shaped, vertical fins mounted on top of the engine nacelles provide directional control; inboard and outboard elevons provide longitudinal and lateral control. The inboard and outboard surfaces simultaneously move; however, the outboard elevons are rigged with 3° more trailing-edge-up incidence than the inboard elevons. The maximum control-surface position limits, however, are the same for both inboard and outboard surfaces. Table 1 lists the SR-71 maximum control-surface position and rate limits.

Table 1. SR-71 aerodynamic control-surface position and rate limits.

Surface	Position limit, deg	Rate limit, deg/sec
Inboard elevons:		
Trailing edge down	20	30
Trailing edge up	35	30
Outboard elevons:		
Trailing edge down	35	30
Trailing edge up	35	30
Rudders:		
Trailing edge left	20	33
Trailing edge right	20	33

All control-surface positions have been measured except that of the right outboard elevon. Because the right outboard elevon position is not instrumented, only the inboard surface positions have been used to define the elevon and aileron deflections (δ_e and δ_a, respectively) for the PID analysis. The additional 3° of trailing-edge-up outboard elevon position has been verified using the left wing inboard and outboard position measurements. The control-surface deflections are defined as follows:

$$\delta_a = (\text{Left inboard } \delta - \text{Right inboard } \delta)/2$$

$$\delta_e = (\text{Left inboard } \delta + \text{Right inboard } \delta)/2$$

$$\delta_r = (\text{Right } \delta + \text{Left } \delta)/2$$

The flight control system includes three-axis auto pilot and stability augmentation systems (SASes). To minimize trim drag, the baseline longitudinal open-loop static stability is designed to be slightly positive at Mach 3.2 with the center of gravity (*CG*) at 0.25 mean aerodynamic chord (*c*) (which is the

6

operational aft *CG* limit). A redundant pitch SAS is used to provide good closed-loop handling qualities at all Mach numbers. The pitch SAS uses high-passed pitch rate to augment damping and lagged pitch rate to slightly augment stability (ref. 5). The SR-71 baseline configuration is also designed to have a minimum, but still positive, derivative of yawing moment due to sideslip $\left(C_{n_\beta}\right)$ at Mach 3.2. A yaw SAS is required to provide acceptable handling qualities at high Mach numbers and to prevent extreme sideslip transients caused by potential inlet "unstarts." The yaw SAS uses yaw-rate feedback for damping and uses lateral acceleration feedback to augment stability. The effective closed-loop directional stability provided by the yaw SAS can be computed using the following equation:

$$\text{Closed-loop } C_{n_\beta} = \text{Open-loop } C_{n_\beta} + 30 C_{n_{\delta_r}} \frac{qS}{w} C_{Y_\beta} \tag{1}$$

A roll SAS is used to provide roll damping through roll-rate feedback.

The empty weight of the SR-71 baseline configuration is approximately 60,700 lb. The SR-71 aircraft has a maximum fuel capacity of 80,000 lb. For these baseline configuration tests, fuel loads of a maximum of 62,000 lb were used.

Linear Aerospike SR-71 Experiment Configuration

The LASRE configuration was developed to obtain in-flight performance data on an aerospike rocket engine. The LASRE components mounted to the top of the SR-71 airplane are referred to as the "canoe," "kayak," "reflection plane," and "model" (fig. 4). Collectively, these structural components are referred to as the LASRE "pod." The canoe was installed on the SR-71 fuselage and was designed to contain the gaseous hydrogen fuel and liquid water needed for cooling. The kayak, located beneath the reflection plane and on top of the canoe, set the model incidence angle to 2° nosedown to align the lower part of the model with the expected local flow over the top of the SR-71 airplane. The reflection plane was mounted on top of the kayak to help promote uniform flow in the region of the model. The model was designed to approximate a half-span lifting body with a 70-deg swept cylinder leading edge and spherical nose. Liquid oxygen and igniter materials required to operate the rocket engine were stored in the model. The model was vertically mounted so that the angle of sideslip of the SR-71 airplane imparted angle of attack on the model.

With a full load of expendables, the pod weighed approximately 14,140 lb. The SR-71 fuel distribution system was adjusted to accommodate a maximum of 67,000 lb of fuel for the LASRE flights. This adjustment was made to prevent overloading the vehicle when carrying the added weight of the LASRE pod. However, actual fuel loads of a maximum of only 62,000 lb were used during the LASRE flight tests. To compensate for *CG* shifts caused by the pod weight, 5000 lb of available fuel in the forward tank was considered unusable during the flight.

The high transonic drag of the LASRE configuration showcased the ability of the SR-71 airplane to achieve stabilized data at speeds approximating Mach 1.0. Apart from the main purpose of this report, this unique capability of the SR-71 airplane to sustain nearly Mach-1 test conditions deserves emphasis. The SR-71 physical attributes (inertia, fineness ratio, control systems, and the relative characteristics of the transonic drag and propulsive forces) all combine to provide a unique platform for exposing

experimental shapes to selected stabilized transonic flow conditions in a real flight environment. These conditions can be maintained for several minutes; and because of the relatively large size of the aircraft, the candidate models can be of a respectable scale and can include significant detail.

Figure 5 shows a time history of a nearly level–altitude acceleration from Mach 0.9 to Mach 1.1. This figure shows the fairly smooth transition from subsonic to supersonic flight. Much of the acceleration was achieved using full afterburner thrust. If desired, the pilot could stabilize at any transonic speed using throttle control (with the exception of stabilizing at free-stream Mach numbers between Mach 1.010 and Mach 1.025, which is where the airdata Mach jump occurs). This capability makes the SR-71 airplane a unique and versatile transonic research facility that is currently available to the flight test community. This research capability of the SR-71 airplane represents a valuable complement to its well-known capability for flight research at high supersonic speeds to a maximum of Mach 3.2.

Test Bed Configuration

Four flights were flown with the model removed from the LASRE pod. This configuration became known as the test bed configuration because it can accommodate new model shapes for flight testing. The weight of the remaining canoe, kayak, and reflection plane is approximately 9400 lb. Fuel loads of a maximum of 66,000 lb were used for these tests.

The test bed configuration also demonstrated its excellent capability for transonic flight research. Figure 6 shows a time history of a nearly level–altitude acceleration from Mach 0.9 to Mach 1.1. As in figure 5, a smooth transition from subsonic to supersonic flight is seen. The angle-of-attack time history shows two longitudinal PID doublets performed during the acceleration. Throttle control can be used to stabilize at any transonic speed (except at the airdata Mach jump).

Mass Properties

Accurate estimates of weight, CG, and mass moments of inertia were required for each PID maneuver. Each fuel tank is instrumented to obtain fuel quantity. The total weight is simply the sum of the zero-fuel weight and the total fuel weight recorded by the six tank sensors. Because of the symmetry of the left and right sides of the aircraft, only the rolling, pitching, and yawing moment and cross product of inertias (I_x, I_y, I_z, and I_{xz}, respectively) were required. Table 2 shows a summary of zero-fuel weight, zero-fuel weight CG, and zero-fuel inertias for the three flight configurations. Figure 7 shows the body-axis mass moments of inertia for the baseline configuration (using the standard fuel burn schedule) as a function of total vehicle weight.

Fuel quantity measurements from the six fuselage fuel tanks are used to compute the CG. Each fuel tank CG is a function of both measured fuel quantity and aircraft pitch attitude. For the LASRE and test bed configurations, pod component CGs are also used to obtain the total configuration CG. Flight data were obtained at CGs ranging from 0.173 c to 0.258 c. Individual fuel quantity measurements and pod component mass distribution information are used to compute the inertias at each test condition.

Table 2. Zero-fuel weight, *CG*, and mass moment of inertia information for the three SR-71 configurations.

Configuration	Flight numbers	SR-71 zero-fuel weight, lb	SR-71 zero-fuel weight *CG*		SR-71 zero-fuel inertias, slug-ft^2
			Fuselage station, in.	Mean aerodynamic chord, percent	
Baseline	37–44	60,728	877.9	20.1	$I_x = 220,660$ $I_y = 954,850$ $I_z = 1,172,039$ $I_{xz} = 19,200$
LASRE	45–48	74,032	911.0	27.4	$I_x = 230,880$ $I_y = 1,035,140$ $I_z = 1,252,330$ $I_{xz} = 44,640$
LASRE	49–51	75,349	910.6	27.3	$I_x = 230,880$ $I_y = 1,035,520$ $I_z = 1,252,710$ $I_{xz} = 44,710$
Test bed	52–55	70,158	892.3	23.3	$I_x = 224,670$ $I_y = 992,280$ $I_z = 1,209,470$ $I_{xz} = 28,390$

METHODS OF ANALYSIS

This section describes the formulation of the output-error parameter estimation technique used to analyze the flight data. The nonlinear equations of motion used in the analysis also are defined.

Parameter Identification Formulation

The primary objective of this research is to estimate from flight test the stability and control derivatives for each of these SR-71 configurations. The actual vehicle system is described by a vector set of dynamic equations of motion that are defined in the next section. The form of these equations is assumed to be known, but the time-invariant aerodynamic stability and control parameters in these equations are unknown. The PID flight test maneuvers are designed to record the response of the aircraft system to measured control inputs. The parameter estimation program known as pEst (ref. 3) is used in postflight analysis to adjust the unknown parameter values in the model until the estimated aircraft response agrees with the measured response.

The pEst program defines a cost function that can be used to quantitatively measure the agreement between the computed response and the actual measured response of the model. The pEst program searches for the unknown parameter values to minimize the cost function.

To obtain the cost function, the pEst program must solve a vector set of time-varying ordinary differential equations of motion. The equations of motion are separated into a continuous-time state equation and a discrete-time response equation:

$$x(t) = F[x(t), u(t), \xi] \qquad (2)$$

$$z(t_i) = G[x(t_i), u(t_i), \xi] \qquad (3)$$

where F is the state derivative function, G is the response function, $\mathbf{x}$ is the state vector, x is the time derivative of the state vector, $\mathbf{z}$ is the response or measurement vector, $\mathbf{u}$ is the measured control input vector, ξ is the stability and control derivative parameter vector, and t is time. For this application of stability and control derivative estimation, state noise is assumed to not exist.

The output-error cost function, $J(\xi)$, used by the pEst program is as follows:

$$J(\xi) = \frac{1}{2n_z n_t} \sum_{i=1}^{n_t} [z(t_i) - \tilde{z}(t_i)]^* W[z(t_i) - \tilde{z}(t_i)] \qquad (4)$$

where n_t is the number of time history points used, n_z is the number of response variables, z is the estimated response vector, and W is the response weighting matrix. The superscript * denotes transpose.

For each possible estimate of the unknown parameters, a probability that the aircraft response time histories attain values approximating the observed values can be defined. The maximum-likelihood estimates are defined as those estimates that maximize this probability. Minimizing the cost function gives the maximum-likelihood estimate of the stability and control parameters.

Figure 8 shows the maximum-likelihood parameter estimation process. The measured response is compared with the estimated response, and the difference between these, called the response error, is included in the cost function. The minimization algorithm is used to find the coefficient values that minimize the cost function. Each iteration of this algorithm provides a new estimate of the unknown coefficients on the basis of the response error. These new estimates are then used to update values of the coefficients of the mathematical model, providing a new estimated response and, therefore, a new response error. Updating the mathematical model iteratively continues until a convergence criterion is satisfied (in this case, the ratio of the change in total cost to the total cost, $\Delta J(\xi)/J(\xi)$, must be less than 0.000001). The estimates resulting from this procedure are the maximum-likelihood estimates.

The estimator also provides a measure of the reliability of each estimate based on the information obtained from each dynamic maneuver. This measure of reliability is called the Cramér-Rao bound (ref. 6). The Cramér-Rao bound is a measure of relative, not absolute, accuracy. A large Cramér-Rao bound indicates poor information content in the maneuver for the derivative estimate.

Equations of Motion

The aircraft equations of motion used in the PID analysis are derived from a general system of nine coupled, nonlinear differential equations that describe the aircraft motion (ref. 4). These equations

assume a rigid vehicle and a <mark>flat, nonrotating Earth.</mark> The time rate of change of mass and inertia is assumed negligible. The SR-71 configurations studied herein, like most aircraft, are basically symmetric about the vertical-centerline plane. This symmetry is used, along with small angle approximations, to separate the equations of motion into two largely independent sets describing the longitudinal and lateral-directional motions of the aircraft. The equations of motion are written in body axes referenced to the *CG* and include both state and response equations. The applicable equations of motion are as follows for the longitudinal and lateral-directional axes:

Longitudinal state equations:

$$\dot{\alpha} = -\frac{qSR}{mV\cos\beta}C_N\cos\alpha + q - \tan\beta(p\cos\alpha + r\sin\alpha) + \frac{gR}{V\cos\beta}(\cos\phi\cos\theta\cos\alpha + \sin\theta\sin\alpha) \quad (5)$$

$$\dot{q}I_y = \bar{q}ScC_mR + [rp(I_z - I_x) + (r^2 - p^2)I_{xz}]/R \quad (6)$$

$$\dot{\theta} = q\cos\phi - r\sin\phi \quad (7)$$

Longitudinal response equations:

$$\tilde{\alpha} = \alpha + x_\alpha\frac{q}{V} \quad (8)$$

$$q = q + q_{bias} \quad (9)$$

$$\tilde{\theta} = \theta \quad (10)$$

$$\tilde{a}_n = \frac{qS}{mg}C_N - \frac{1}{gR}\left[x_{a_n}\dot{q} + y_{a_n}\dot{p}\right] - \frac{1}{gR^2}z_{a_n}(q^2 + p^2) + a_{n_{bias}} \quad (11)$$

where q_{bias} and $a_{n_{bias}}$ are estimates of instrumentation biases and *R* is a conversion factor between degrees and radians.

Lateral-directional state equations:

$$\dot{\beta} = \frac{qSR}{mV}C_Y + p\sin\alpha - r\cos\alpha + \frac{gR}{V}[\sin\phi\cos\theta\cos\beta - \sin\beta(\cos\theta\cos\phi\sin\alpha - \sin\theta\cos\alpha)] \quad (12)$$

$$\dot{p}I_x - \dot{r}I_{xz} = qSbC_lR + [qr(I_y - I_z) + pqI_{xz}]/R \quad (13)$$

$$\dot{r}I_z - \dot{p}I_{xz} = qSbC_nR + [pq(I_x - I_y) - qrI_{xz}]/R \quad (14)$$

$$\dot{\phi} = p + q\tan\theta\sin\phi + r\tan\theta\cos\phi \quad (15)$$

11

Lateral-directional response equations:

$$\tilde{\beta} = \beta + \left[z_\beta \frac{p}{V} - x_\beta \frac{r}{V} \right] + \beta_{bias} \tag{16}$$

$$p = p + p_{bias} \tag{17}$$

$$r = r + r_{bias} \tag{18}$$

$$\tilde{\phi} = \phi \tag{19}$$

$$\tilde{a}_y = \frac{qS}{mg} C_Y + \frac{1}{gR} \left[-x_{a_y} \dot{r} + z_{a_y} \dot{p} \right] - \frac{1}{gR^2} y_{a_y} (p^2 + r^2) \tag{20}$$

where β_{bias}, p_{bias}, and r_{bias} are estimates of instrumentation biases.

Equations (5)–(20) contain locally linear approximations of the aerodynamic coefficients. The longitudinal aerodynamic coefficients are expanded as follows:

$$C_N = C_{N_b} + C_{N_\alpha} \alpha + \frac{c}{2VR} C_{N_q} q + C_{N_{\delta_e}} \delta_e \tag{21}$$

$$C_m = C_{m_b} + C_{m_\alpha} \alpha + \frac{c}{2VR} C_{m_q} q + C_{m_{\delta_e}} \delta_e \tag{22}$$

The coefficients are based on a reference area of 1605 ft^2 and a mean aerodynamic chord of 37.7 ft. The coefficient with the subscript "*b*" is a linear extrapolation of the angle-of-attack derivative from the average angle of attack of the maneuver to 0° angle of attack (ref. 6). Axial force coefficients are not used in this analysis because the engine performance model is not well known, but this is not a concern because the axial force derivatives do not significantly affect flying qualities. All the longitudinal derivatives in equations (21)–(22) are estimated in the analysis.

The lateral-directional aerodynamic coefficients are expanded as follows:

$$C_Y = C_{Y_b} + C_{Y_\beta} \beta + \frac{b}{2VR} (C_{Y_p} p + C_{Y_r} r) + C_{Y_{\delta_a}} \delta_a + C_{Y_{\delta_r}} \delta_r \tag{23}$$

$$C_l = C_{l_b} + C_{l_\beta} \beta + \frac{b}{2VR} (C_{l_p} p + C_{l_r} r) + C_{l_{\delta_a}} \delta_a + C_{l_{\delta_r}} \delta_r \tag{24}$$

$$C_n = C_{n_b} + C_{n_\beta} \beta + \frac{b}{2VR} (C_{n_p} p + C_{n_r} r) + C_{n_{\delta_a}} \delta_a + C_{n_{\delta_r}} \delta_r \tag{25}$$

The reference span, b, is 56.7 ft. The coefficient with the subscript "b" is a linear extrapolation of the angle-of-sideslip derivative from the average angle of sideslip of the maneuver to 0° angle of sideslip. All the lateral-directional derivatives in equations (23)–(25) were estimated in the analysis.

INSTRUMENTATION AND DATA ACQUISITION

The SR-71 airplane is equipped with a complete set of research airdata and inertial instrumentation. Free-stream pitot-static airdata are obtained from a calibrated noseboom. Angle-of-attack and -sideslip data are obtained from a four-hole hemispherical probe doglegged to the noseboom. The angle of attack is referenced to the wing reference plane, which is 1.2-deg nosedown in incidence compared to the fuselage centerline reference plane. Angle-of-attack and -sideslip measurements are lagged on the order of 0.2 to 0.4 sec because of the pneumatic plumbing. These lags are accounted for by time skews in the data analysis. Pitch and roll attitude data are obtained from the SR-71 inertial navigation system. Three-axis angular rate and linear accelerations are measured using strapdown sensors installed at fuselage station (*FS)* 683.0, butt line (*BL)* 32.5, and water line (*WL)* 86.2.

Signal conditioning on the angular rate and acceleration measurements includes a first-order passive antialiasing filter with a 40-Hz rolloff frequency. This filter imparts a 45-deg phase lag that is equivalent to a 3-msec time lag.   This time lag is less than the sample time interval of 5 msec. Although measured at sample rates that are higher, the flight data are thinned to 20 samples/sec for the PID analysis. Angles of attack and sideslip and linear accelerations are corrected in the mathematical model of the pEst program to the *CG* using angular rate measurements and sensor position information. Vehicle weight and longitudinal *CG* location are obtained using fuel tank measurements. Laterally and vertically, the *CG* is assumed to be located at *BL* 0 and *WL* 100, respectively. All control-surface positions are measured with the exception of the right outboard elevon. For the PID analysis, only the inboard surface positions are used to define the elevon and aileron deflections.

In the PID analysis, angle of attack and normal acceleration are the primary aircraft responses used to obtain normal force coefficient estimations.   Similarly, angle of sideslip and lateral acceleration are used to obtain side force coefficient estimates. Because of uncertainties in the calibration and pneumatic lags associated with the flow angle measurements, larger weights are assigned to the acceleration response measurements in the PID analysis than to the flow angle response measurements. The response weights are constant for all configurations tested, with the exception of a few cases where temporary instrumentation problems existed.

FLIGHT TEST APPROACH

The objective of this research is to obtain baseline SR-71 stability and control derivatives from PID flight data. When the baseline derivatives are known, the aerodynamic effects of the LASRE and test bed configurations can then be obtained from further PID flight testing. An "envelope expansion" approach has been used to safely "clear" the configuration to the desired maximum Mach number. The envelope was expanded by incrementally increasing Mach number and performing PID doublet maneuvers. The pilots evaluated the airplane handling qualities in real time, and the PID maneuvers were analyzed postflight using the pEst program to obtain stability and control derivative estimates. Therefore, multiple flights were required to clear the envelope for safe operations.

Each PID maneuver consisted of pilot-performed doublet inputs. Figure 9 shows a typical longitudinal maneuver. As the figure shows, the pilot performs the pitch doublet by pushing the stick forward, pulling the stick aft, and then returning the stick to the neutral position. Figure 10 shows a typical lateral-directional maneuver. The maneuver consists of the pilot performing a yaw doublet with the rudders immediately followed by a roll doublet with lateral stick movements. The rudder pedal inputs were not measured or needed for the PID analysis. The required rudder surface deflections, however, were measured (fig. 10).

For PID analysis, the aircraft response measurement signal-to-noise ratio needs to be large enough to obtain good identifiability. Typically, signal-to-noise ratios greater than 5 are considered adequate. For SR-71 operations, structured loads constraints limited the size of the doublet maneuvers. For the LASRE and test bed configurations, the constraints were defined as angular acceleration limits and a normal acceleration limit. The angular acceleration limits were 43.0 deg/sec^2 for roll, 4.5 deg/sec^2 for yaw, and 8.0 deg/sec^2 for pitch (note that angular accelerations were not measured on the airplane, but were computed in real time in the control room from angular rate measurements). The normal acceleration constraint required the maneuver to be performed between 0.6 and 1.4 g. Because of the initially unknown aerodynamics of the LASRE configuration, two sizes of doublet maneuvers were used for the LASRE configuration testing. At each Mach condition, an initial micro-sized doublet was performed. If the pilots and the control room personnel concurred that a larger doublet would not exceed the constraints, then the pilot would execute a larger, but still small-sized, doublet.

Ideally, the doublets would be performed at a stabilized 1-g flight condition. However, for flight test efficiency reasons, many of the maneuvers were performed during accelerated flight. Typically, PID data for supersonic conditions were obtained during a 450-knots equivalent airspeed (*KEAS*) climbing acceleration to Mach 2.6 that was followed by a continuous "*KEAS* bleed" to 390 *KEAS* as the airplane climbed and accelerated to approximately Mach 3.2. The supersonic deceleration typically consisted of a 365-*KEAS* descent during which PID data were also obtained. Because of the SR-71 aeroelastic characteristics, obtaining PID data at consistent equivalent airspeeds was desirable. For the highly flexible SR-71 aircraft, the stability and control derivatives are a secondary function of dynamic pressure in many cases. This data set emphasized obtaining supersonic data at two dynamic pressure conditions to show the influence of aircraft flexibility on the derivatives. The 450-*KEAS* acceleration equated to a dynamic pressure of 686 lbf/ft^2 and the 365-*KEAS* deceleration equated to a dynamic pressure of 451 lbf/ft^2. In some cases, data also were obtained for less than 365 *KEAS* for additional envelope clearance.

After each flight test, the PID maneuvers were analyzed to obtain the flight-determined stability and control derivatives. Pilot simulations before the subsequent flight included updated aerodynamic model information from the analysis of the previous flights PID maneuvers.

RESULTS AND DISCUSSION

Extensive flight testing has been completed to assess the changes in aircraft stability and control caused by adding experiments to the top of the SR-71 airplane. Flight data to a maximum speed of Mach 3.00 for the SR-71 baseline configuration, to a maximum speed of Mach 1.75 for the LASRE configuration, and to a maximum speed of Mach 3.00 for the test bed configuration are presented herein. To obtain these results, 283 doublet maneuvers were flown and analyzed.

14

Simulation predictions of the baseline derivatives have been compared with flight data. The simulation predictions come from a workstation-based batch simulation. The aerodynamic model incorporated into the simulator came from the SR-71 baseline aerodynamic model (ref. 4). Predicted stability and control derivatives were obtained by linearizing the aerodynamic model at the flight test Mach number, altitude, and mass property conditions. Simulation predictions will be plotted only to compare with the baseline configuration flight results. Predicted increments to the stability and control derivatives caused by the LASRE pod installation were obtained in wind-tunnel tests and published in reference 7. No wind-tunnel predictions, however, were obtained for the test bed configuration.

The PID analysis was used to estimate the open-loop stability and control derivatives from pilot-input doublet maneuvers. Stability augmentation systems were used at all times in all axes to increase the closed-loop stability and damping. With the SASes remaining on, autopilots were turned off for the axes of interest during the PID maneuvers. Some of the initial flight test results for the test bed configuration have been published in reference 2 and for the baseline and LASRE configurations in reference 8.

For the LASRE configuration, both micro-sized and larger, but still small-sized, doublets were performed. In many cases, the PID analysis shows good fits of the measured and estimated response parameters for the micro-sized doublets. However, the Cramér-Rao bounds were usually larger for the micro-sized doublets than for the small-sized doublets because of smaller signal-to-noise ratios; and the parameter estimate sometimes differed from multiple estimates using the micro-sized doublet. Therefore, only small-sized doublet results are presented in this report.

Figures 11–13 show the flight envelope available for this testing and the Mach number and altitude flight conditions used for the baseline, LASRE, and test bed configurations, respectively. The flight conditions referred to as "low-*KEAS*" test points are shown in the shaded regions of figures 11–13. The remaining test points are considered "high-*KEAS*" test points. The distinction between low-*KEAS* and high-*KEAS* test points is important because, in some cases, aircraft flexibility affected the stability and control derivatives. The flexibility effects were included in the baseline aerodynamic model (ref. 2).

Flight data were obtained at *CG* values ranging between 0.173 and 0.258 *c*. All moment derivatives were estimated about the flight *CG* using the pEst program. For presentation in this report, the pitching and yawing moment derivatives were corrected to the moment reference using flight-estimated normal and side force derivatives, respectively (ref. 9). The moment reference is located at 0.25 *c* (*FS* 900).

Scatter in derivative estimates could be caused by maneuvers being performed at different weights, angles of attack, trim elevon positions, and bank angles. Slight variations in maneuver sizes, flexibility effects, and not accounting for engine gyroscopic effects (which are assumed negligible) could also result in data scatter. As stated previously, the Cramér-Rao bounds (ref. 6) are used as a measure of relative, but not absolute, accuracy. Large Cramér-Rao bounds indicate poor information content in the maneuver for the derivative estimate. The Cramér-Rao bounds plotted in this report have been multiplied by a factor of five to increase clarity.

Longitudinal Derivatives

Longitudinal stability and control derivatives were determined independently from lateral-directional derivatives. This section presents results from the SR-71 baseline, LASRE, and test bed configurations obtained using longitudinal PID pitch doublet maneuvers. A comparison of the stability and control derivatives obtained from the three configurations also will be shown.

Baseline Configuration

Figure 14 shows time histories from typical subsonic, transonic, and supersonic test points. These time histories include pilot stick inputs, elevon control-surface positions, and aircraft responses for angle of attack, pitch rate, pitch attitude, and normal acceleration. For the response parameters, the solid lines represent measured aircraft responses and the dashed lines represent the responses obtained by integrating the equations of motion using the pEst estimates of the stability and control derivatives. As figure 14 shows, the angle-of-attack response shows the worst fit between measured and pEst-estimated responses. This result is not surprising because in the pEst program, the angle-of-attack measurement is weighted less than the normal acceleration measurement because of high confidence in the normal acceleration measurement as explained in the "Instrumentation and Data Acquisition" section. Figures 15–18 show the baseline longitudinal stability and control derivatives.

Figure 15 shows coefficient of normal force and pitching moment bias (C_{N_b} and C_{m_b}) estimates. The circle symbols represent high-*KEAS* test points and the cross symbols represent low-*KEAS* test points. The solid and dashed lines are fairings of the high- and low-*KEAS* results, respectively. These fairings are based on the authors' interpretation of the trends in the flight estimates. The vertical bars on the plots represent the scaled Cramér-Rao bounds. The C_{N_b} do not show significant differences caused by flexibility. The C_{m_b} show reduced values at supersonic speeds for the low-*KEAS* test points, especially at approximately Mach 1.8. Note that these bias values are not the traditional normal force and pitching moment coefficients at 0° angle of attack with no surface deflections. The parameter estimation program, pEst, uses a maximum-likelihood technique to obtain a linear fit of the data around the trim point. The bias is simply the extrapolation of the linear fit to 0° angle of attack. For these test points, the trimmed wing reference plane angle of attack varied between 2.5° and 6°. The baseline aerodynamic model (ref. 4) contains a reasonably linear normal force coefficient over this angle-of-attack range, but the pitching moment coefficient typically was nonlinear. Also, reference 4 shows that the nonlinear effect of aircraft flexibility on pitching moment becomes increasingly significant at supersonic Mach numbers, which is consistent with the observed change in pitching moment coefficient bias estimates at supersonic speeds caused by aircraft flexibility.

Figure 16 shows the angle-of-attack derivatives. The thin solid lines are the simulation-predicted values for the high-*KEAS* test points, and the thin dashed lines are the simulation-predicted values for the low-*KEAS* test points. The flight data show reduced values for derivatives of normal force due to angle of attack, C_{N_α}, compared to the simulation values. The flight data also show the simulation-predicted flexibility effects (fig. 16(a)).

Figure 16(b) shows the derivative of pitching moment due to angle of attack, C_{m_α}. The flight data show slightly reduced static stability (that is, less negative) compared with the simulator values, and the flexibility effects at supersonic Mach numbers are not as pronounced in the flight data. Note that C_{m_α} is computed about the 0.25-*c* moment reference point. The positive values at subsonic Mach numbers do not indicate that the airplane was ever flown with negative static margins. For those test points, the *CG* was significantly forward of the 0.25-*c* reference location. As figure 16(b) also shows, the static stability tends toward zero as Mach number is increased. This tendency was expected because the SR-71 aircraft is designed to have minimum open-loop static stability at the design cruise Mach number of 3.2 to reduce trim drag (ref. 4). The design Mach 3.2 cruise *CG* location for acceptable stability and trim drag is 0.25 *c*.

Figure 17 shows the dynamic derivatives. The baseline aerodynamic model (ref. 4) assumes a zero value for the derivative of normal force due to nondimensional pitch rate, C_{N_q}. The flight data show C_{N_q} generally decreases as Mach number increases (figure 17(a)). The derivative of pitching moment due to nondimensional pitch rate, C_{m_q}, measured in flight was larger (that is, a more negative derivative) than predicted, with the exception of the data recorded at Mach 2.5 (fig. 17(b)). The reason for the variation in the derivative estimates at Mach 2.5 is suspected to be that the two test points with positive values were flown at an altitude of 65,000 ft and the two test points with negative values were flown at an altitude of 60,000 ft. Although the simulator predicted no difference in the C_{m_q} for these two conditions, open-loop damping is known to decrease as altitude increases (ref. 4). Open-loop damping is also expected to be reduced as the Mach number increases toward the Mach-3.2 design condition. The test point at Mach 3.0 was flown at an altitude of 80,000 ft and showed a negative C_{m_q} value that causes the values recorded at Mach 2.5 and an altitude of 65,000 ft to be suspect (although only one test point was obtained at Mach 3.0).

Figure 18 shows the elevator control derivatives. The flight-determined normal force derivative estimates are less than predicted (fig. 18(a)). For supersonic conditions, the flight-determined normal force derivative estimates were almost zero. The flexibility effects predicted by the simulation are evident in the flight data. The flight-estimated near-zero elevator contribution to normal force seemed anomalous to the authors; however, further scrutiny of the analysis consistently confirmed the result that deflecting the elevators had little effect on normal force. An equation-error PID technique (ref. 10) also was used to analyze these data and shows the same result. Figure 18(b) shows the pitching moment effectiveness of the elevator. The flight data and simulator predictions agree well and the flexibility effects are clearly seen, especially at supersonic-condition Mach numbers where a clear distinction exists between low- and high-*KEAS* test points. This aeroelastic effect was expected because control surfaces on flexible aircraft typically become less effective as dynamic pressure increases.

Linear Aerospike SR-71 Experiment Configuration

Figure 19 shows time histories from typical test points for the LASRE configuration at subsonic, transonic, and supersonic conditions. Good fits were obtained between the measured and pEst-estimated responses; angle-of-attack fit is the most noticeably off. The measured pitch rate (fig. 19(b)) shows a 2-Hz response that is caused by the fuselage first-bending mode. Some maneuvers not shown in figure 19 also show a 2-Hz response in the normal accelerometer output. The pEst implementation used in this research assumes rigid body motion and was expected to identify aircraft flexibility effects that result from changes in dynamic pressure. The pEst program was not expected to identify the high-frequency structural modes because no structural equations of motion are included in the formulation. Therefore, the pEst-estimated responses are not expected to match this observed 2-Hz motion.

Figures 20–23 show the LASRE configuration longitudinal stability and control derivatives. Only a few low-*KEAS* test points were obtained during the LASRE program; these points were at Mach numbers approximating 0.90, 1.20, and 1.45 (fig. 9).

Figures 20(a) and 20(b) show the C_{N_b} and C_{m_b}, respectively. A negative C_{N_b} is seen across the Mach range tested. The pitching moment coefficient bias is negative (nosedown) for subsonic conditions, shows a large positive (noseup) value for transonic conditions, and then shows a constant positive value for supersonic conditions. Flexibility effects are seen in the C_{N_b} and C_{m_b} during flight at Mach 1.45. Figure 21 shows angle-of-attack derivatives. No clear flexibility effects are evident from the flight data. Figure 22 shows the dynamic derivatives, and figure 23 shows the elevator effectiveness derivatives. As with the baseline configuration, the elevators are consistently more effective at the low-*KEAS* test points (fig. 23(b)).

Test Bed Configuration

Figure 24 shows time histories from typical test points for the test bed configuration at subsonic, transonic, and supersonic conditions. Good fits were obtained between the measured and pEst-estimated responses; angle-of-attack fit again is the most noticeably off. Figure 24(c) shows that the airplane responses at Mach 3.02 were very small, although the stick inputs and elevon deflections were approximately the same magnitude as at low-speed conditions. These small responses resulted in some of the high-speed derivative estimates having larger Cramér-Rao bounds (because of smaller response measurement signal-to-noise ratios) than low-speed test points.

Figures 25–28 show the test bed configuration longitudinal stability and control derivatives. Figure 13 shows the flight test conditions. As figure 13 shows, the majority of the low-*KEAS* points are at 365 *KEAS* and the majority of the high-*KEAS* points are at 450 *KEAS*.

Figure 25 shows the C_{N_b} and C_{m_b}. Some flexibility effects have been identified. Figure 26 shows the angle-of-attack derivatives. High-*KEAS* test points at Mach 2.10 and Mach 2.23 did show a significantly reduced C_{m_α} for the test bed configuration (fig. 26(b)). These results were obtained on the second test bed flight; the results were not repeated on the third test bed flight when doublets were flown

at similar Mach numbers. An aerodynamic explanation for these two data points likely exists because they were flown at a slightly higher normal acceleration (approximately 1.2 g), which resulted in the trim angle of attack being approximately 1° higher and the elevon trim being 1° more noseup. At these slightly different trim conditions, the shock structure is suspected to be different enough to manifest into a reduced stability. Note that these two test points also show reduced C_{m_b} values compared to other high-*KEAS* test points (fig. 25(b)).

Flexibility effects in the angle-of-attack derivatives generally were small but in the same direction as the baseline configuration. Figure 27 shows the dynamic derivatives, and figure 28 shows the elevator effectiveness derivatives. As with the baseline and LASRE configurations, the elevators are consistently more effective at the low-*KEAS* test points (fig. 28(b)), demonstrating an effect of aircraft flexibility.

Configuration Comparisons

To better assess the effects of the experimental configurations on the longitudinal aerodynamics, the derivatives from each configuration are plotted together (without Cramér-Rao bounds for clarity). Figure 29 shows the test points used for this comparison. The test points used for plotting were chosen so that the derivative plots would not be confusing because of flexibility effects (although a low-*KEAS* test point is included for the baseline configuration because no high-*KEAS* data were available at approximately Mach 3.0).

Figure 30 shows the C_{N_b} and C_{m_b} values. A significant amount of scatter exists in the bias coefficients at speeds less than Mach 0.6. At subsonic conditions, the LASRE configuration generally shows more negative normal force coefficient bias values (fig. 30(a)), which would indicate a down force caused by the LASRE pod. At supersonic conditions, no difference exists in normal force coefficient bias values.

Figure 30(b) shows the C_{m_b}. The LASRE configuration has a more negative (that is, more nosedown) C_{m_b} at subsonic speeds, and a larger C_{m_b} at the transonic Mach numbers, compared to the baseline configuration. The test bed configuration does not have as much nosedown bias at subsonic conditions, but has a similar transonic peak, as the LASRE data. The test bed C_{m_b} at Mach 1.2–1.5 is significantly less than the biases for the baseline and LASRE configurations. These trends in C_{m_b} are consistent with results documented in references 2 and 8 for the flight-measured pitching moment coefficient at 0° angle of attack and zero control surface deflections.

At subsonic conditions, the LASRE model is suspected to cause a reduction in the surface pressures on the upper surface of the SR-71 airplane at the aft model location, which results in a more negative C_{m_b}. At Mach numbers greater than 1.2, the shock from the LASRE model increased the surface

pressures on the aft fuselage, and the shock from the leading edge of the canoe increased the pressures on the fuselage forward of the *CG*. This increase resulted in no change in C_{m_b} at the low, supersonic-condition Mach numbers compared with the baseline values. However, removing the model for the test bed configuration resulted in a significant nosedown C_{m_b} increment at Mach 1.2–1.6 because the model was no longer pressurizing the upper fuselage. This effect of the canoe and model on pitching moment was identified in the preflight wind-tunnel tests (ref. 7) and quantified in flight. As discussed in references 2 and 8, these transonic pitching moment changes caused by the LASRE and test bed experiments did not result in violating any safety-of-flight margins in trimming the airplane.

Figure 31 shows the angle-of-attack derivative comparison for the three configurations. As the figure shows, the experiments mounted on the SR-71 airplane caused only minor changes in the C_{N_α} and C_{m_α}. Although not a flight safety concern, the test bed configuration was less stable in the Mach 1.3–1.6 region. What caused this reduced stability is unknown.

Figure 32 shows the pitch-rate derivative comparison. As seen previously, the C_{m_q} contains a lot of scatter but shows a general reduction in damping (that is, less negative values) as Mach number increases. Also, the pitch damping for the experimental configurations was reduced from the baseline configuration values for Mach 0.9–2.5. The elevon derivative estimates (fig. 33) show excellent agreement for the three configurations with only some scatter at the low subsonic speeds. This agreement demonstrates that no significant effect exists of the upper fuselage–mounted experiments on the pitch control effectiveness of the elevons.

The data in figures 30–33 indicate that the experiments mounted on the back of the SR-71 airplane primarily affect the normal force and pitching moment coefficient bias values. No flight safety or handling quality concerns have been identified because of experiment effects on longitudinal stability, pitch damping, or elevon control effectiveness. Some reduced longitudinal stability was seen for the test bed configuration at Mach 1.3–1.6, and the pitch damping for the LASRE and test bed configurations was reduced at Mach 0.9–2.5.

Lateral-Directional Derivatives

Lateral-directional stability and control derivatives were determined independently from longitudinal derivatives. This section presents results from the SR-71 baseline, LASRE, and test bed configurations obtained using lateral-directional PID doublet maneuvers. A comparison of the stability and control derivatives obtained from the three configurations is also shown.

Baseline Configuration

Figure 34 shows time histories from typical subsonic, transonic, and supersonic test points for the SR-71 baseline configuration. These time histories include pilot lateral stick inputs, rudder and aileron control-surface positions, and airplane responses for angle of sideslip, roll rate, yaw rate, roll attitude, and

lateral acceleration. For the response parameters, the solid lines represent measured airplane responses, and the dashed lines represent the responses obtained by integrating the equations of motion using the pEst estimates of the stability and control derivatives. Good fits between the measured and pEst-estimated responses were obtained for all of the response parameters. Figures 35–40 show the lateral-directional stability and control derivatives for the baseline configuration.

Figure 35 shows the coefficients of side force, rolling moment, and yawing moment biases, C_{Y_b}, C_{l_b}, and C_{n_b}. The SR-71 aircraft is basically symmetrical about the vertical-centerline plane and all maneuvers were trimmed at almost 0° angle of sideslip. Because the PID maneuvers were done with only small variations in angle of sideslip about 0° and because the aerodynamics are almost linear at these small sideslip angles, the bias values were expected to be approximately zero. For the most part, the flight data did show bias values at approximately zero (fig. 35).

Figure 36 shows the angle-of-sideslip derivatives. The estimated derivative of side force due to sideslip, C_{Y_β}, was typically 25-percent less than predicted (figure 36(a)). The trends with Mach number and the lack of flexibility effects agree with the simulation. The derivative of rolling moment due to sideslip, C_{l_β}, agrees well with predictions (figure 36(b)). The C_{l_β} is more negative at the low-*KEAS* test points compared to the high-KEAS test points, as was predicted by the simulation and as was expected for a flexible aircraft. The C_{n_β} estimated in flight agrees very well with predictions (fig. 36(c)), with the only difference being an improvement in stability (that is, more positive value) at Mach 2. The SR-71 aircraft was designed to have minimum directional static stability at the design cruise speed of Mach 3.2 (ref. 4) to save tail weight and drag.

Figure 37 shows the dynamic derivatives due to roll rate. The derivative of rolling moment due to nondimensional roll rate, C_{l_p}, is less than predicted and shows an aeroelastic effect (figure 37(b)). Figure 38 shows the dynamic derivatives due to yaw rate. The derivative of yawing moment due to nondimensional yaw rate, C_{n_r}, was higher (that is, a more negative value) than predicted for Mach numbers less than 2.5 (fig. 38(c)). As Mach number increases beyond 2.5, the flight data suggests negative open-loop yaw damping (that is, positive values of C_{n_r}). Reduced yaw damping is seen for some of the low-*KEAS* test points at supersonic conditions. The combination of low aerodynamic yaw damping and low directional stability (fig. 36(c)) at high-supersonic conditions resulted in the requirement for a yaw-axis SAS for adequate closed-loop handling qualities (refs. 4 and 5).

Figure 39 shows the rudder derivatives. Generally, slightly lower side force and higher rolling moment effectiveness values were seen in flight compared to predictions. The flight data agree well with the predicted yawing moment effectiveness values of the rudders, with the exception of lower flight-determined values at subsonic conditions.

Figure 40 shows the aileron derivatives. The simulation uses zero for the derivative of side force due to aileron. The flight data estimated a small number slightly greater than zero (fig. 40(a)). The flight data agree well with the predicted derivative of rolling moment due to aileron, $C_{l_{\delta_a}}$, except at approximately

Mach 0.9 where the flight-determined effectiveness is higher than predicted (fig. 40(b)). As predicted and expected for a flexible aircraft, the flight data show increased rolling moment effectiveness for the low-*KEAS* test points. The flight data show significantly lower derivatives of yawing moment due to aileron than predicted (fig. 40(c)).

Linear Aerospike SR-71 Experiment Configuration

Figure 41 shows time histories from typical test points for the LASRE configuration at subsonic, transonic, and supersonic conditions. Good fits between the measured and pEst-estimated responses were obtained for all of the response parameters.

Figures 42–47 show the LASRE configuration lateral-directional stability and control derivatives. Only three low-*KEAS* test conditions were available for the LASRE configuration data. This lack of data makes it difficult to assess flexibility effects for this configuration.

Figure 42 shows C_{Y_b}, C_{l_b}, and C_{n_b}. These biases were expected to be almost zero because of the symmetry of the LASRE pod. The flight data show these to be almost zero except at Mach 0.9 for the high-*KEAS* test point and the C_{l_b} values at subsonic conditions. The LASRE configuration would normally trim at approximately $0°$ angle of sideslip. At the high-*KEAS* Mach-0.9 test points, the configuration trimmed at –0.5° angle of sideslip, which was a result of using the rudders to trim out the large positive C_{n_b} shown in figure 42(c). What nonsymmetry in the geometry or aerodynamic flow caused this large C_{n_b} value is uncertain.

The low-*KEAS*, Mach-0.9 test point did not show this large C_{n_b} value and trimmed at approximately $0°$ angle of sideslip. In this case, the low- and high-*KEAS* test points were only separated by 26 kn. The high-*KEAS* test point was flown at an altitude of 27,300 ft (349 *KEAS*), and the low-*KEAS* test point was only 3,800 ft higher at an altitude of 31,100 ft (323 *KEAS*). That such a large change in C_{n_b} and trim angle of sideslip would occur over such a small change in equivalent airspeeds is interesting. The C_{l_b} value at Mach 0.4 is also of interest (figure 42(b)). For this test point, the trim angle of sideslip was 0.5°, which was the result of trimming out the positive C_{l_b}.

Figure 43 shows the angle-of-sideslip derivatives. The C_{l_β} becomes less negative as the Mach number increases throughout the subsonic range, and then becomes fairly constant for supersonic conditions (fig. 43(b)). Figure 43(c) shows that C_{n_β} decreases slightly with Mach number and remains stable (that is, positive). Figure 43(c) also shows an increase in C_{n_β} for the high-*KEAS* test points at Mach 0.9, at which the vehicle trimmed at –0.5° angle of sideslip as stated above.

Figures 44 and 45 show the dynamic derivatives due to roll rate and yaw rate, respectively. The C_{l_p} is constant throughout the Mach range studied (fig. 44(b)). The C_{n_r} starts at approximately zero and then increases (that is, becomes more negative) as Mach number increases (fig. 45(c)). A significant increase

in yaw damping occurs as the airplane transitions from subsonic to supersonic flight. Also, aeroelastic effects caused a reduction in yaw damping for the low-*KEAS* test points at supersonic conditions.

Figure 46 shows the rudder derivatives. The most variation in the derivatives occurs between Mach 0.9 and Mach 1.0. The yawing moment effectiveness of the rudders remains constant throughout the Mach range except at approximately Mach 0.9, at which the effectiveness is increased (fig. 46(c)). Figure 47 shows the aileron derivatives. The rolling moment effectiveness of the ailerons decreases with increasing Mach number (figure 47(b)). As expected for a flexible aircraft, the low-*KEAS* test points indicate higher rolling moment effectiveness values than existed for the high-*KEAS* test points. Figure 47(c) shows proverse yaw throughout the Mach range with the curious exception at Mach 1.05.

Test Bed Configuration

Figure 48 shows time histories from typical test points for the test bed configuration at subsonic, transonic, and supersonic conditions. Good fits between the measured and pEst-estimated responses were obtained for all of the response parameters. Figures 49–54 show the test bed configuration lateral-directional stability and control derivatives.

Figure 49 shows C_{Y_b}, C_{l_b}, and C_{n_b}. The values in general are approximately zero for all three derivatives, with the exception of slightly positive C_{l_b} values at subsonic conditions. Figure 50 shows the angle-of-sideslip derivatives. The C_{l_β} decreases toward zero between Mach 2.0 and 3.0 as seen in figure 50(b). The C_{n_β} values (fig. 50(c)) show a sharp decrease beginning at Mach 2.2, level off at slightly positive values at Mach 2.5, and remain constant to Mach 3.0. Aeroelastic effects are seen in the C_{l_β} and C_{n_β} data at speeds less than Mach 2.

Figures 51 and 52 show the dynamic derivatives due to roll rate and yaw rate, respectively. The C_{l_p} values are negative and fairly constant to a maximum of Mach 2.5, at which point they becomes less negative and then slightly positive at Mach 3.0 (fig. 51(b)). The C_{n_r} values have moderate scatter but remain negative throughout the Mach range (fig. 52(c)).

Figure 53 shows the rudder derivatives. The yawing effectiveness of the rudders reaches its maximum at almost Mach 1, then decreases as Mach number increases to Mach 3.0. Some aeroelastic effects are shown in the rolling and yawing moment rudder derivatives. Figure 54 shows the aileron derivatives. The $C_{l_{\delta_a}}$ decreases with increasing Mach number (fig. 54(b)). As with the baseline and LASRE configurations, the low-*KEAS* test points indicate higher aileron rolling moment effectiveness values than those for the high-*KEAS* test points. Figure 54(c) shows mostly proverse yaw at the low Mach numbers; slight adverse yaw begins at Mach 2.3.

Configuration Comparisons

To assess the effects of the experimental configurations on the lateral-directional aerodynamics, the derivatives from each configuration are plotted together (with Cramér-Rao bounds not included for clarity). Figure 55 shows the test points used for this comparison. The test points used for plotting were chosen so that the derivative plots would not be confusing because of flexibility effects (although a low-*KEAS* test point is included for the baseline configuration because no high-*KEAS* data were available at approximately Mach 3.0).

Figure 56 shows a comparison of the lateral-directional coefficient bias values. No significant differences in the biases were expected because the LASRE and test bed configurations are symmetric about the vertical-centerline plane. Differences did occur, however, at subsonic-condition Mach numbers and particularly at Mach 0.9 for the C_{l_b} and C_{n_b} (figs. 56 (b) and (c)). These differences are caused by some unknown geometric or aerodynamic asymmetry.

Figure 57 shows the angle-of-sideslip derivatives. The C_{l_β} is reduced for the LASRE and test bed configurations compared to the baseline configuration (fig. 57(b)). Why C_{l_β} would decrease for configurations with the experiments on top is not intuitive; especially with the LASRE configuration, which essentially includes an additional vertical surface. Wind-tunnel tests (ref. 8) did predict the reduction in C_{l_b} for the LASRE configuration. Because the test bed configuration saw a similar reduction in C_{l_b}, the canoe is suspected to be the significant contributor to the reduction. The test bed dihedral effect values approach zero as Mach number increases.

The C_{n_β} was also significantly affected by the LASRE and test bed configurations. At transonic conditions, both experimental configurations show a reduction in C_{n_β} compared to the baseline configuration. This reduction again was not intuitive; especially for the LASRE configuration, which includes the "vertical-like" surface. The test bed configuration directional stability decreased significantly beginning at Mach 2.2 and leveled out at Mach 2.5 with a slightly positive value (fig. 57(c)). This concern was significant during the envelope expansion phase of the test bed program.

Piloted simulations were done to determine the effect of reduced open-loop stability derivatives on handling qualities and aircraft responses caused by failures of a single engine (for example, inlet unstarts). With reduced directional stability, an engine failure could result in significant sideslip leading to aircraft structural failure. Simulations were done to demonstrate the open-loop directional stability level at which point an engine failure would result in exceeding the aircraft sideslip limit. With the additional closed-loop stability provided by the yaw SAS (eq. (1)), the determination was made that flight tests could safely proceed to Mach 3.2. A new mission rule was created, however, requiring the *CG* to be forward of 23 percent for flight at speeds faster than Mach 2.5 (ref. 2).

Figure 58 shows a comparison of the roll-rate dynamic derivatives. For the most part, significant differences in the data scatter are difficult to see. Some evidence exists that the C_{l_p} decreases (that is, the derivative becomes less negative) at speeds faster than Mach 2.5 for the test bed configuration, and even shows positive values at speeds faster than Mach 2.9 (fig. 58(b)). Figure 59 shows a comparison of the yaw-rate dynamic derivatives. The C_{n_r} (fig. 59(c)) tends to indicate that yaw damping for the test bed configuration increases at speeds faster than Mach 2.5 compared to the baseline configuration.

Figure 60 shows the rudder control derivatives. The LASRE configuration shows reduced side force, rolling moment, and yawing moment derivatives at high subsonic–condition and low supersonic–condition Mach numbers compared to the baseline configuration. This reduction is especially true at Mach 0.9, at which C_{n_b} and C_{l_b} were known to be affected by the LASRE experiment. At speeds greater than Mach 1.5, no difference exists in rudder control effectiveness for the three configurations.

Figure 61 shows the aileron control derivatives. The aileron derivative of primary interest is the $C_{l_{\delta_a}}$ (fig. 61(b)). As can be seen, the LASRE and test bed configurations had little to no effect on the rolling moment effectiveness of the ailerons. The LASRE model, however, did have large effects on the side force and yawing moment derivatives that show significantly more proverse yaw at speeds less than Mach 1.8, except at approximately Mach 1.05.

The data in figures 56–61 indicate that the experiments mounted on the back of the SR-71 airplane did affect lateral-directional stability and control. The primary concern for the project was the reduced static stability and reduced dihedral effects at high Mach numbers for the test bed configuration. The LASRE configuration also demonstrated reduced directional control effectiveness at transonic-condition Mach numbers, but this was not a concern to the project because the SR-71 tails were sized for the Mach-3.2 design cruise condition and thus were very effective at the transonic speeds.

CONCLUDING REMARKS

Longitudinal and lateral-directional stability and control derivatives were obtained from flight test of the SR-71 baseline aircraft and from SR-71 configurations with the Linear Aerospike SR-71 Experiment (LASRE) and test bed experiment hardware mounted on the SR-71 upper fuselage. A maximum-likelihood output-error parameter estimation program was used to analyze a total of 283 pilot-input doublet maneuvers. This work has resulted in a significant database of parameter identification maneuvers for a large, flexible aircraft over a range from Mach 0.4 to Mach 3.0. Many test points were obtained at transonic speeds because of the ability of the SR-71 aircraft to stabilize at flight conditions at almost Mach 1.0. Also, the aeroelastic characteristics of the aircraft were studied by obtaining flight data at different dynamic pressures. Longitudinal and lateral-directional stability and control flight tests of the three SR-71 configurations showed the results detailed in the following sections.

Longitudinal Derivatives

The SR-71 baseline flight estimates of the longitudinal stability and control derivatives were compared with the simulation predictions. The flight-determined normal force derivative caused by angle of attack was less than predicted, but did show the predicted flexibility effects. The flight data showed slightly reduced derivatives of pitching moment due to angle of attack, C_{m_α}, compared to predictions and did not show significant variation in static stability caused by flexibility. The flight data showed larger derivative values of pitching moment due to nondimensional pitch rate, C_{m_q}, than predicted. The derivative of normal force due to elevon was significantly less than predicted, but showed predicted flexibility effects. The derivative of pitching moment due to elevon, $C_{m_{\delta_e}}$, agreed well with predictions and showed increased control effectiveness at low dynamic pressures, as expected for a flexible wing.

The LASRE and test bed configuration flight data were compared with the baseline configuration data to assess the effects of the experimental hardware on the longitudinal stability and control derivatives. The results obtained are as follows:

- The LASRE experiment induced a more nosedown pitching moment bias at subsonic-condition Mach numbers compared to the baseline and test bed configurations. Both the LASRE and test bed configurations showed larger noseup values at approximately Mach 1. The test bed configuration showed a large nosedown increment at low supersonic Mach numbers.

- Mounting of the LASRE and test bed hardware did not significantly affect the open-loop C_{m_α}. Some reduced stability was seen for the test bed configuration at Mach 1.3–1.6.

- The C_{m_q} for the LASRE and test bed configurations was reduced at Mach 0.9–2.5.

- The $C_{m_{\delta_e}}$ showed excellent agreement for the three configurations and had only some scatter at low subsonic speeds.

In general, the experimental hardware of the LASRE and test bed configurations resulted in no significant stability, control, trim, handling quality, or safety-of-flight concerns in the longitudinal axis.

Lateral-Directional Derivatives

The SR-71 baseline flight estimates of the lateral-directional stability and control derivatives were compared with the simulation predictions. The flight-determined side force derivatives caused by angle of sideslip were approximately 25-percent lower than predicted at all Mach numbers. The derivative of rolling moment due to sideslip, C_{l_β}, agreed well with predictions, including the prediction of increased dihedral effect at low dynamic pressures. The derivative of yawing moment

due to sideslip, C_{n_β}, agreed well with predictions except at Mach 2, at which flight data showed higher stability than predicted. As predicted in the simulation, no change in stability caused by flexibility effects existed. The flight data showed less roll damping than predicted and showed some aeroelastic effects. The yaw damping was higher than predicted for speeds less than Mach 2.5. As Mach number increased beyond Mach 2.5, the flight data showed negative open-loop yaw damping. The flight data agreed well with predictions of the yawing moment due to rudder except at subsonic speeds, at which the flight data showed less effectiveness than predicted. The flight data agreed well with the predicted derivative of rolling moment due to aileron, $C_{l_{\delta_a}}$, except at approximately Mach 0.9, at which the flight-determined effectiveness was higher than predicted. As predicted and expected for a flexible aircraft, the flight data showed increased rolling moment effectiveness for the low–knots-equivalent-airspeed test points. The flight data also showed significantly lower yawing moment due to aileron than predicted.

The LASRE and test bed configuration flight data were compared with the baseline configuration data to assess the effects of the experimental hardware on the lateral-directional stability and control derivatives. The results are as follows:

- The LASRE rolling moment and yawing moment coefficient bias values were significantly different than the test bed and baseline configuration values at Mach 0.9.

- The LASRE and test bed configurations demonstrated a reduced C_{l_β} compared to the baseline configuration values.

- The LASRE and test bed C_{n_β} showed reductions at transonic flight conditions compared to the baseline configuration. At approximately Mach 2.2, the test bed open-loop directional stability began decreasing rapidly toward zero. At Mach 2.5, the stability leveled off and remained relatively constant to Mach 3.0. This reduced stability was of great concern during the envelope expansion phase; however, simulations showed enough margins to fly safely at these high Mach numbers with the test bed configuration and with stability augmentation systems fully operational.

- The LASRE model had a significant effect on the rudder derivatives at transonic speeds. The side force, rolling moment, and yawing moment derivatives caused by rudder deflection were all smaller than the test bed and baseline derivatives at transonic speeds. In addition, at Mach 0.9, the LASRE rolling and yawing moment rudder derivatives showed significant negative peaks caused by some unknown transonic interaction. None of these rudder derivative variations resulted in safety-of-flight concerns.

- The $C_{l_{\delta_a}}$ was unaffected by the LASRE and test bed configurations.

- The LASRE model did have a large effect on the sideforce and yawing moment aileron derivatives. The LASRE data showed significantly more proverse yaw than the baseline and test bed configurations, except at approximately Mach 1.05.

The most significant lateral-directional effect of the experimental hardware was the reduction of directional stability of the test bed configuration at speeds greater than Mach 2.2. Flight tests to Mach 3.0 and simulation of emergency situations showed that even with the reduced stability, the test bed configuration could be safely flown. In general, the LASRE and test bed experimental configurations showed acceptable stability, control, trim, and handling qualities throughout the Mach regimes tested.

As a concluding remark, future potential SR-71 "piggyback" flight test experiments can use the results presented in this report to "size" and locate experimental hardware on the back of the SR-71 airplane to ensure adequate stability and control capability. For example, any reasonably aerodynamically shaped hardware mounted at the aft end of the canoe should improve the directional stability above that seen for the test bed configuration.

REFERENCES

1. Corda, Stephen, Bradford A. Neal, Timothy R. Moes, Timothy H. Cox, Richard C. Monaghan, Leonard S. Voelker, Griffin P. Corpening, Richard R. Larson, and Bruce G. Powers, *Flight Testing the Linear Aerospike SR-71 Experiment (LASRE)*, NASA TM-1998-206567, 1998.

2. Corda, Stephen, Timothy R. Moes, Masashi Mizukami, Neal E. Hass, Daniel Jones, Richard C. Monaghan, Ronald J. Ray, Michele L. Jarvis, and Nathan Palumbo, *The SR-71 Test Bed Aircraft: A Facility for High-Speed Flight Research*, NASA TP-2000-209023, 2000.

3. Murray, James E. and Richard E. Maine, *pEst Version 2.1 User's Manual*, NASA TM-88280, 1987.

4. Lockheed Aircraft Corporation, *Handling Qualities of the SR-71*, SP-508, Oct. 1964.

5. DeGrey, R. P., R. L. Nelson, and J. E. Meyer, "SR-71 Digital Automatic Flight and Inlet Control System," SAE-851977, Oct. 1985.

6. Maine, Richard E. and Kenneth W. Iliff, *Application of Parameter Estimation to Aircraft Stability and Control: The Output-Error Approach*, NASA RP-1168, 1986.

7. Moes, Timothy R., Brent R. Cobleigh, Timothy R. Conners, Timothy H. Cox, Stephen C. Smith, and Norm Shirakata, *Wind-Tunnel Development of an SR-71 Aerospike Rocket Flight Test Configuration*, NASA TM-4749, 1996 (also published as AIAA-96-2409).

8. Moes, Timothy R., Brent R. Cobleigh, Timothy H. Cox, Timothy R. Conners, Kenneth W. Iliff, and Bruce G. Powers, *Flight Stability and Control and Performance Results from the Linear Aerospike SR-71 Experiment (LASRE)*, NASA TM-1998-206565, 1998 (also published as AIAA-98-4340).

9. Gainer, Thomas G. and Sherwood Hoffman, *Summary of Transformation Equations and Equations of Motion Used in Free Flight and Wind Tunnel Data Reduction and Analysis*, NASA SP-3070, 1972.

10. Morelli, Eugene A., "Real-Time Parameter Estimation in the Frequency Domain," AIAA-99-4043, Aug. 1999.

Figure 1. SR-71 baseline configuration in flight.
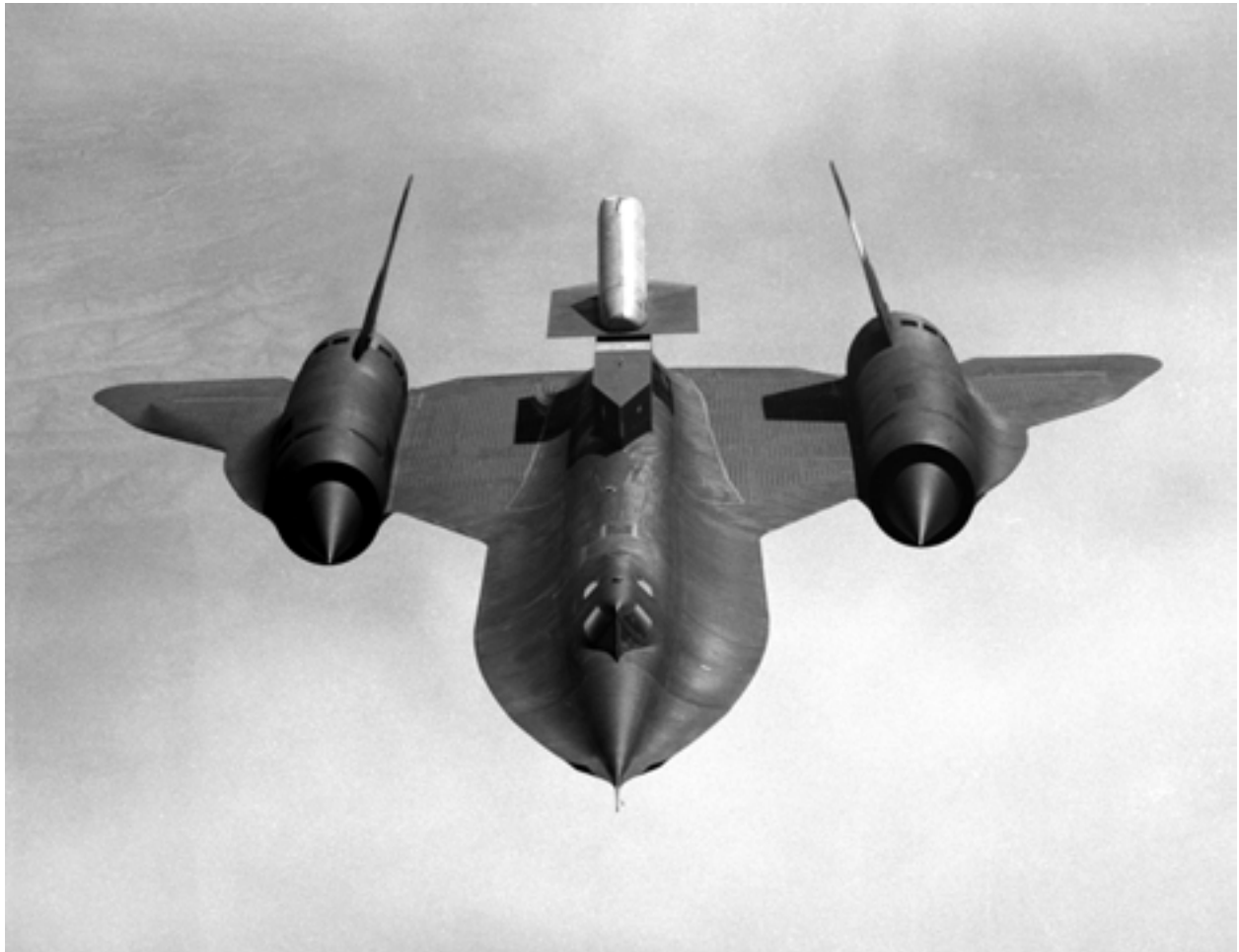
Figure 2. LASRE configuration in flight.

Figure 3. Test bed configuration in flight.
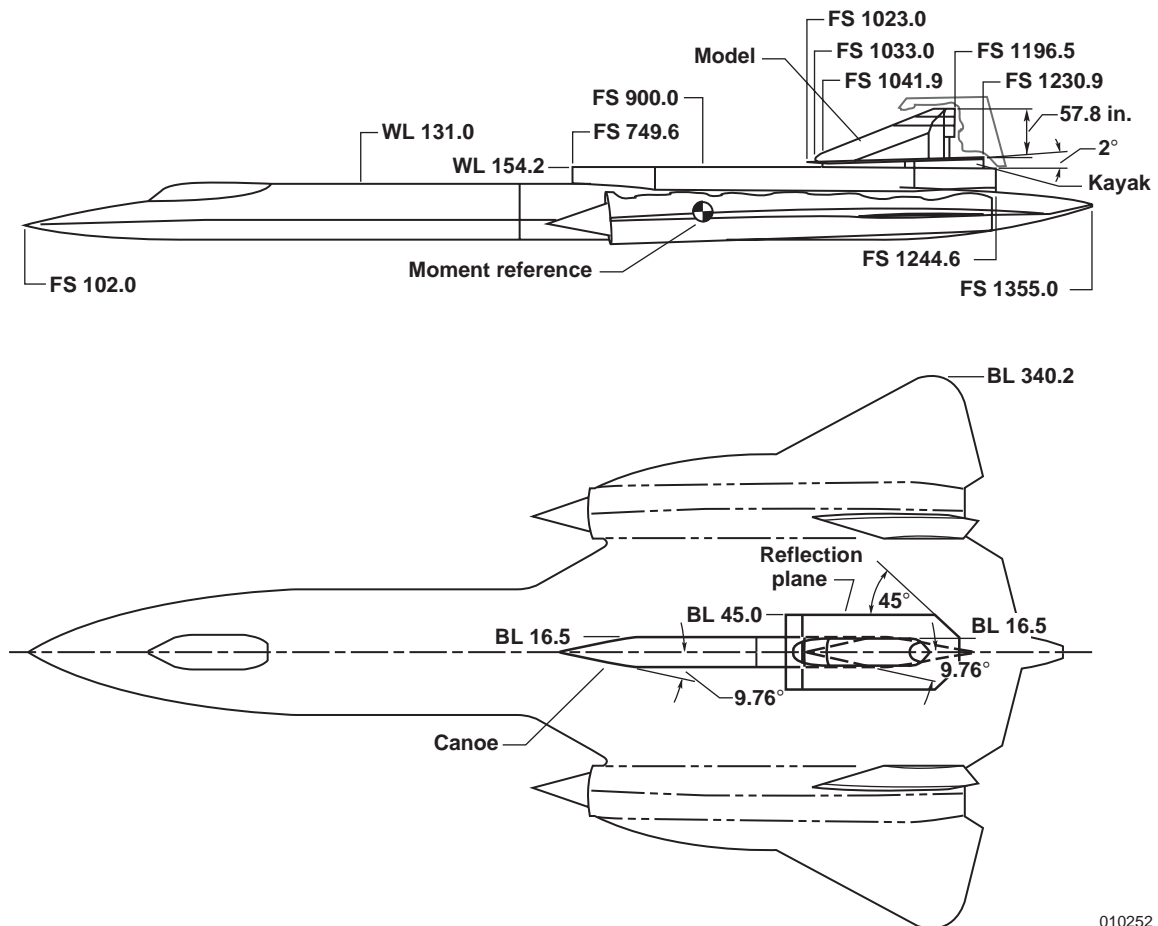
Figure 4. Side and planform views of the LASRE configuration.
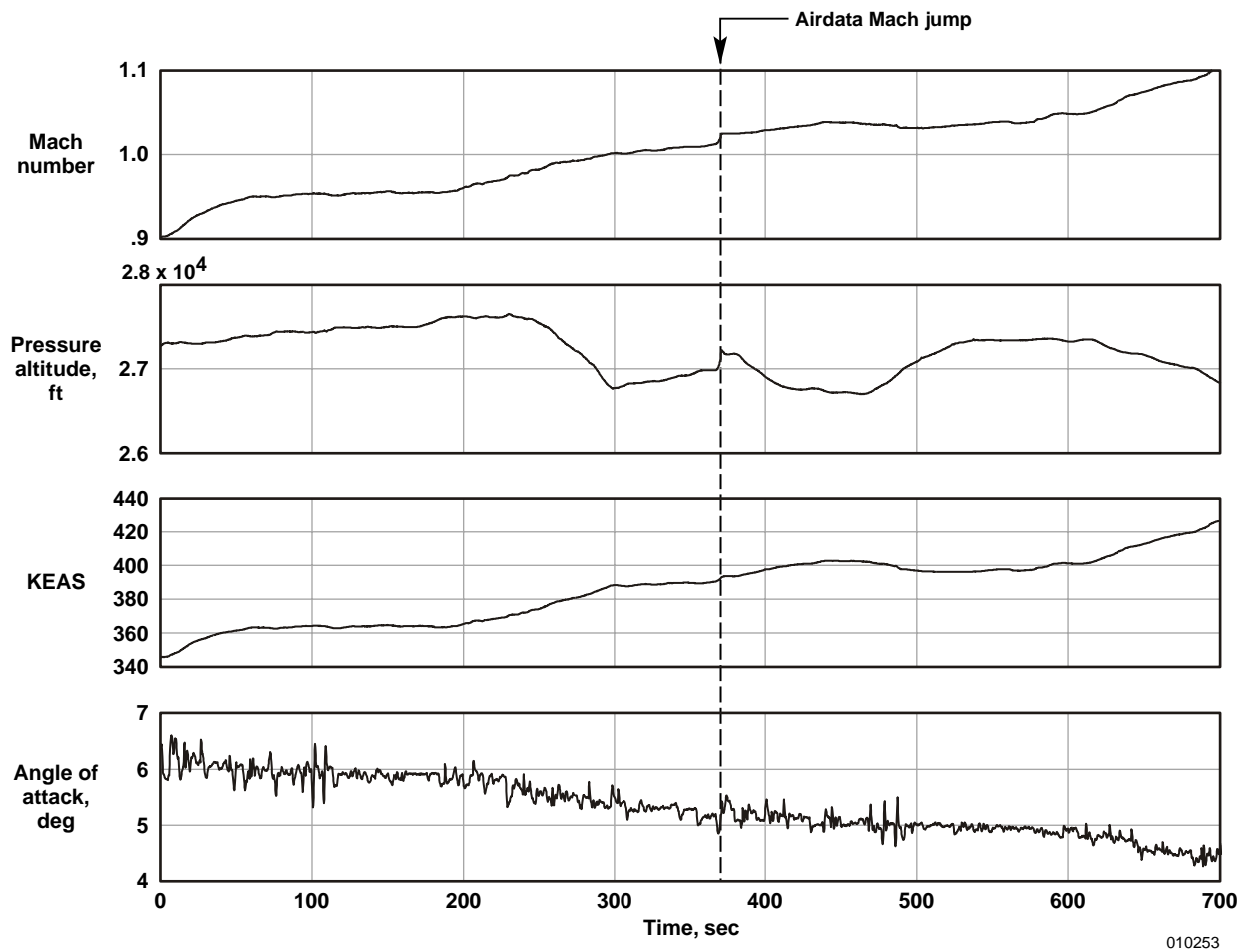
Figure 5. Time history of an acceleration from subsonic to supersonic flight (LASRE configuration).
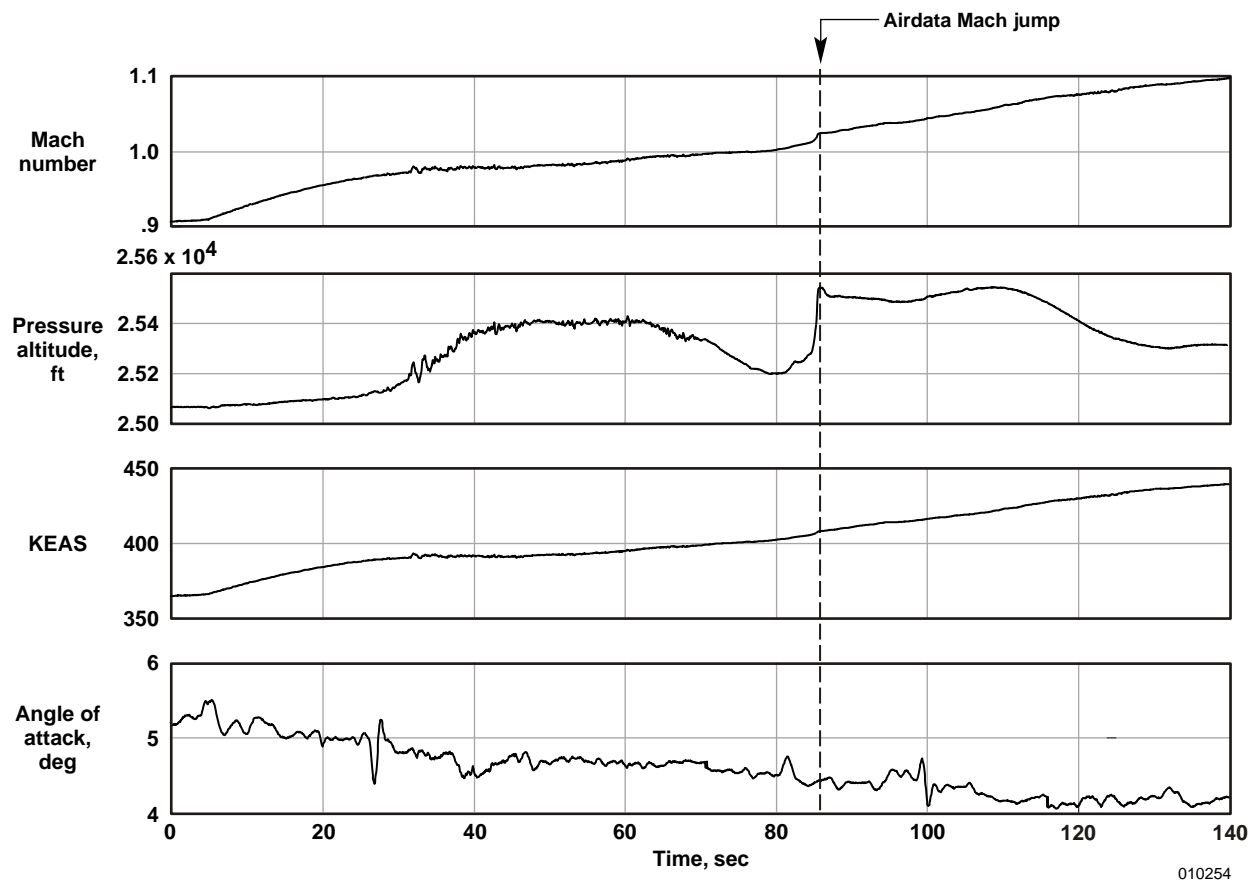
Figure 6. Time history of an acceleration from subsonic to supersonic flight (test bed configuration).
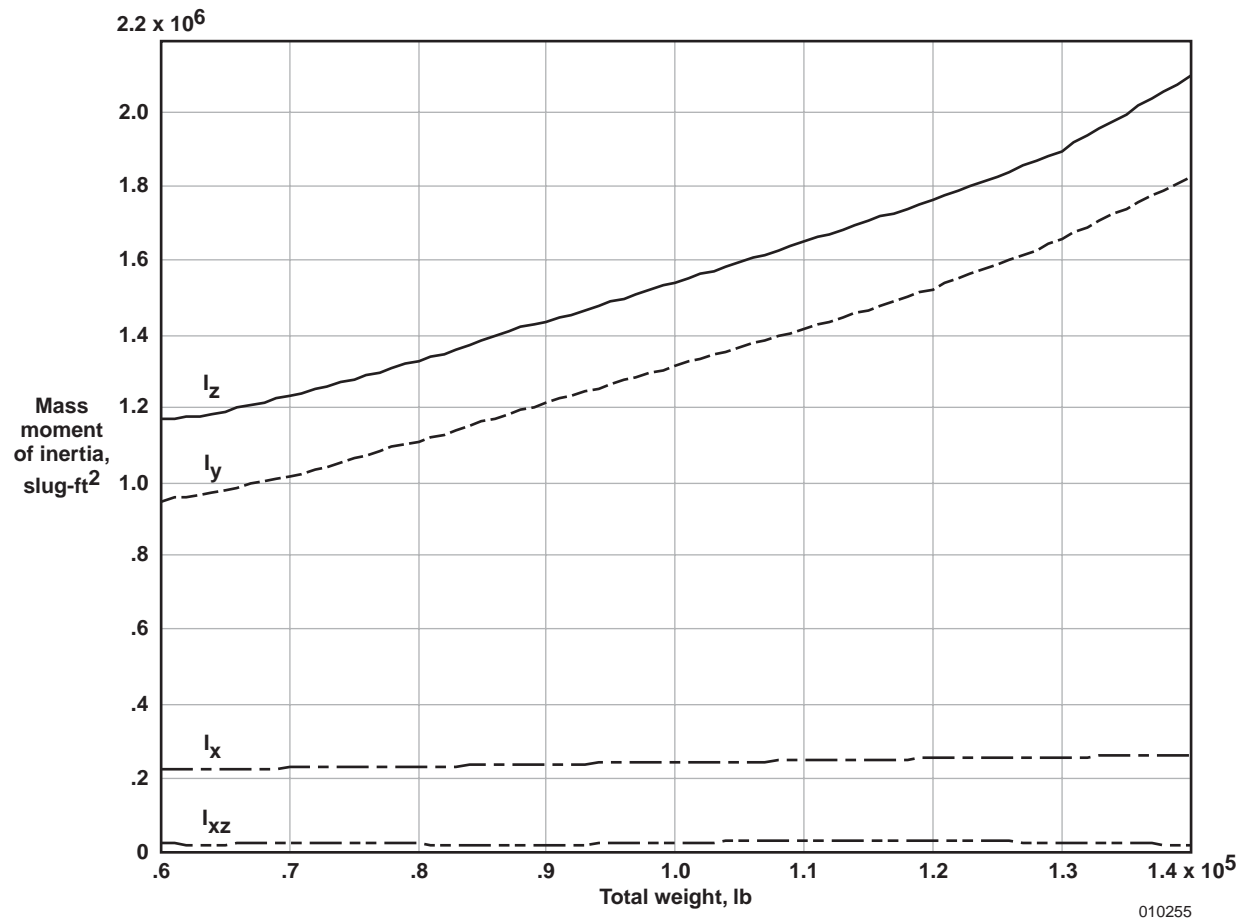
Figure 7. Body-axis mass moments of inertia for the baseline configuration using the standard fuel burn schedule.
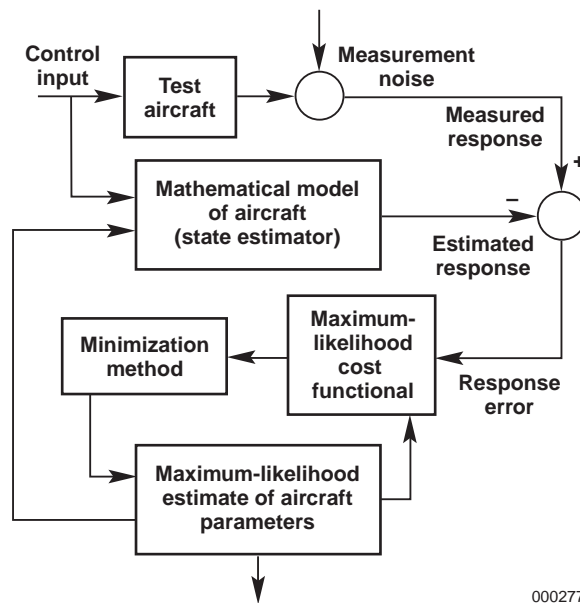
Figure 8. Maximum-likelihood parameter estimation process.
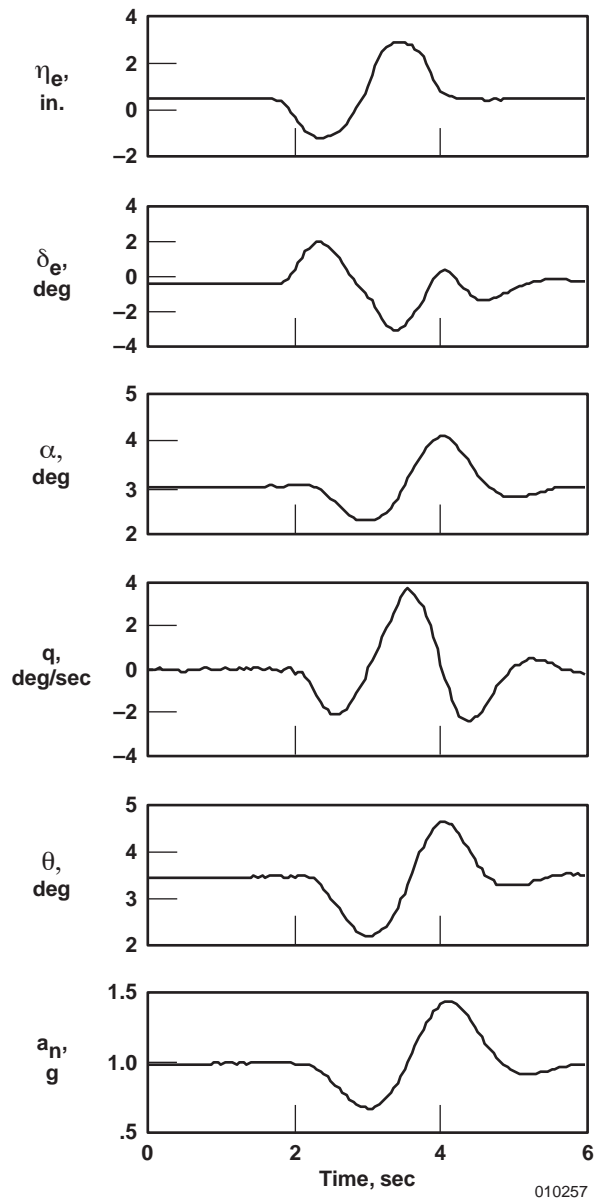
Figure 9. Typical pitch doublet time history (Mach 1.06 and an altitude of 27,900 ft).
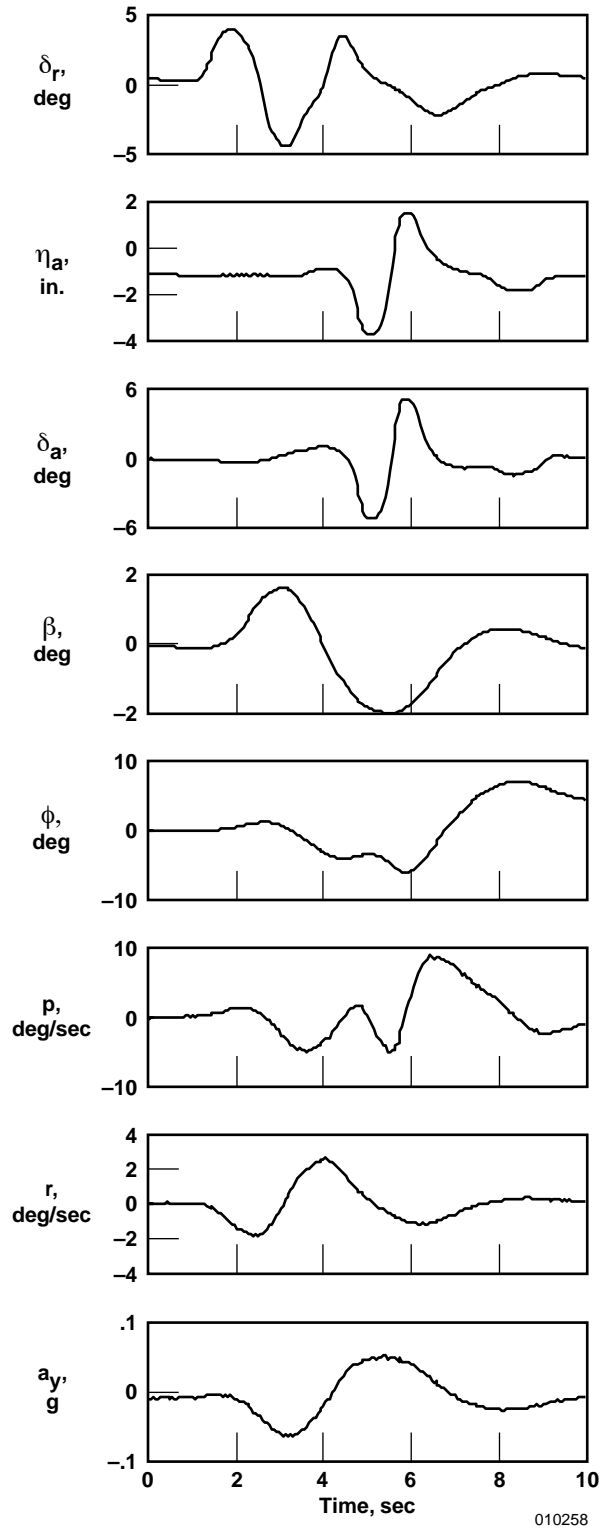
Figure 10. Typical yaw-roll doublet time history (Mach 2.79 and an altitude of 79,800 ft).
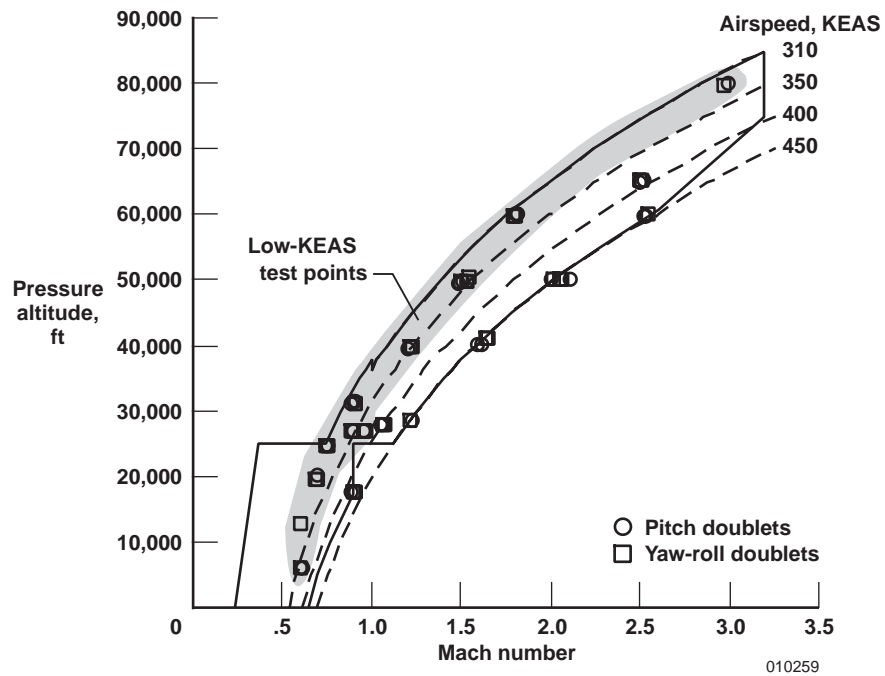
Figure 11. Flight conditions for stability and control test points (baseline configuration).
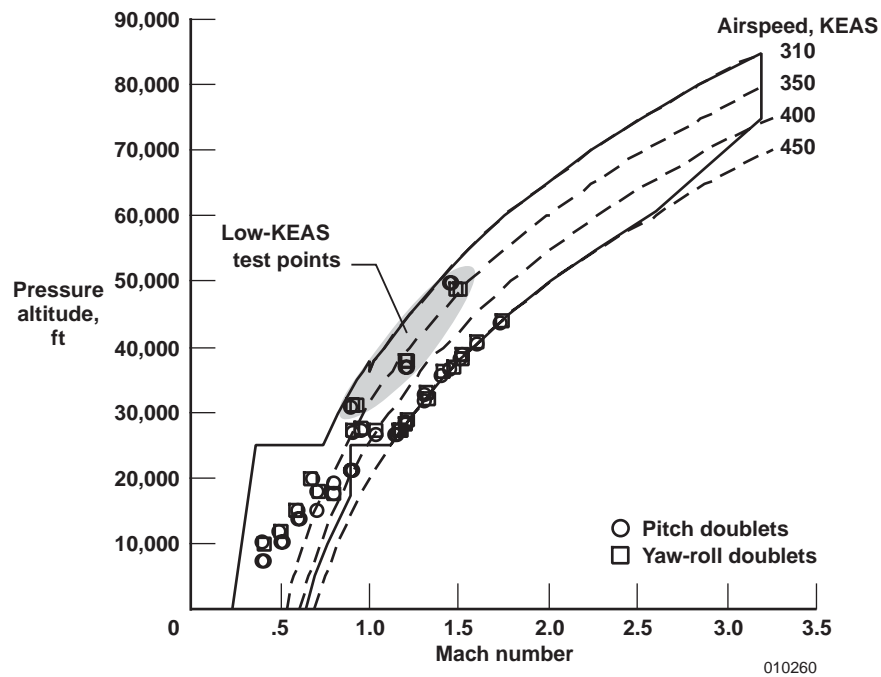
Figure 12. Flight conditions for stability and control test points (LASRE configuration).
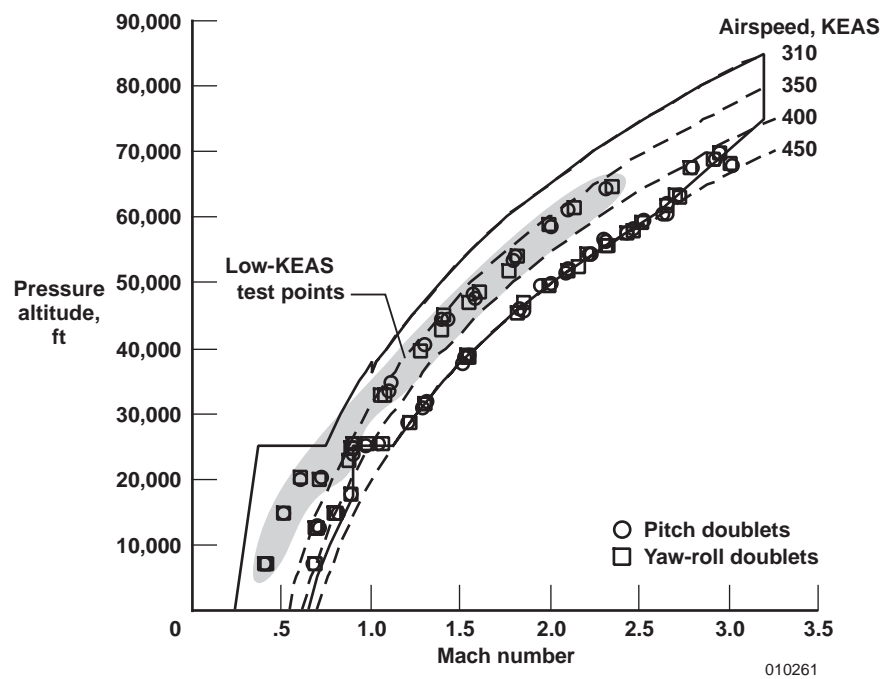
Figure 13. Flight conditions for stability and control test points (test bed configuration).
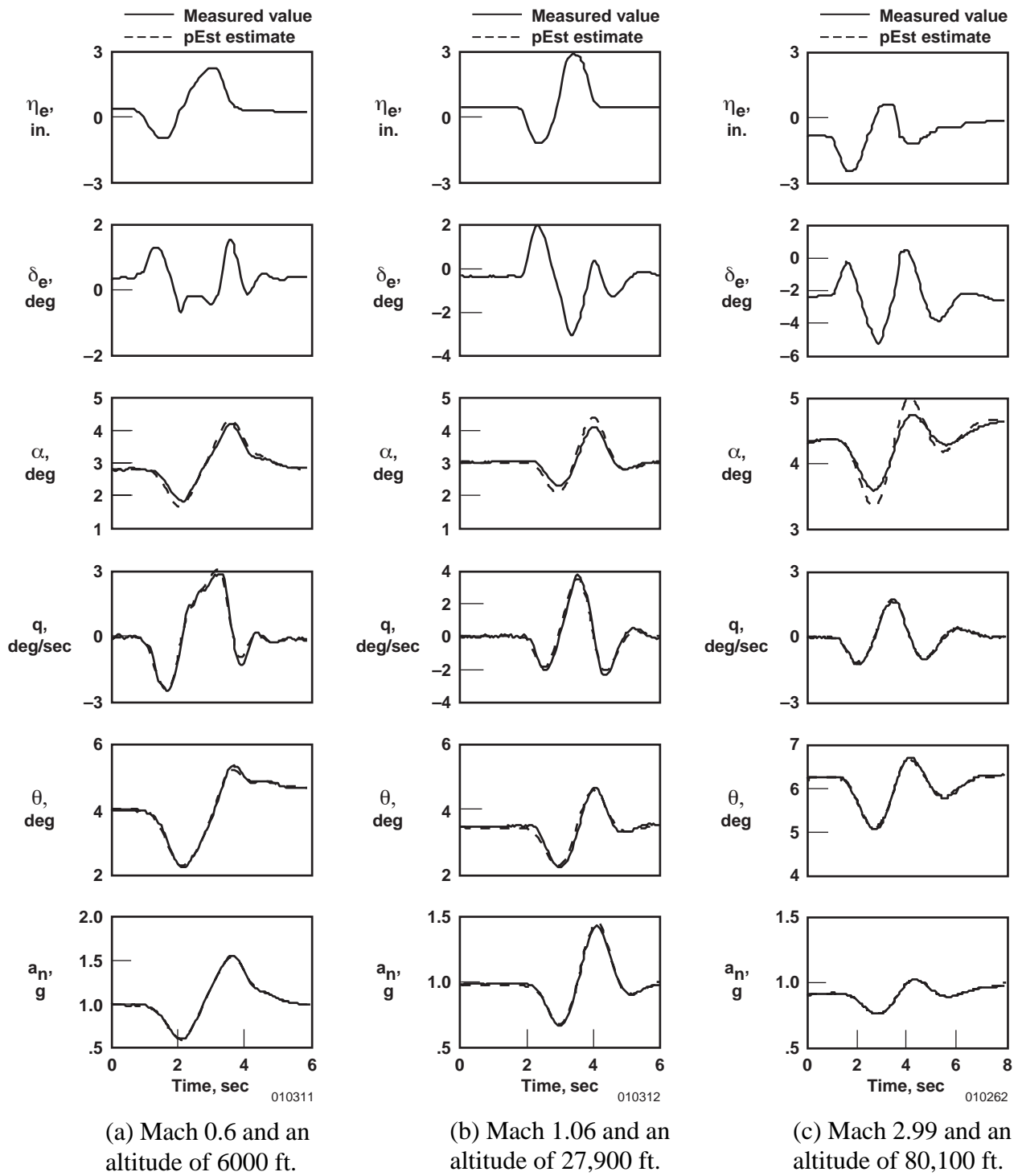
Figure 14. Baseline configuration longitudinal maneuver time histories.

(a) C_{N_b}.

(b) C_{m_b}.
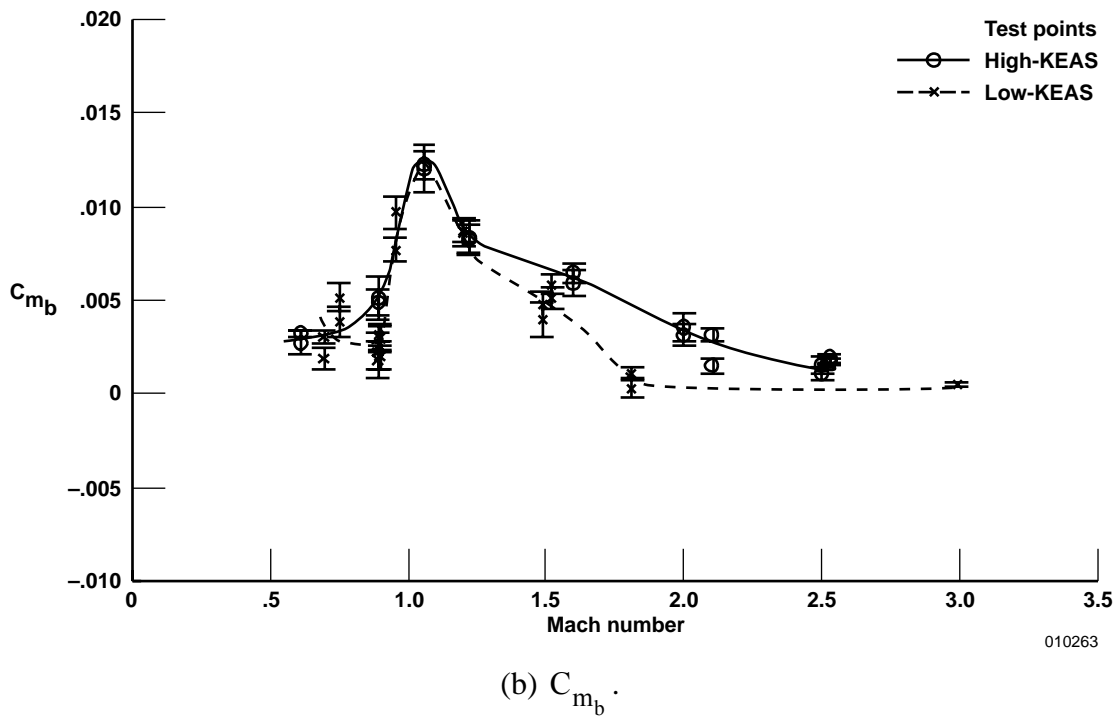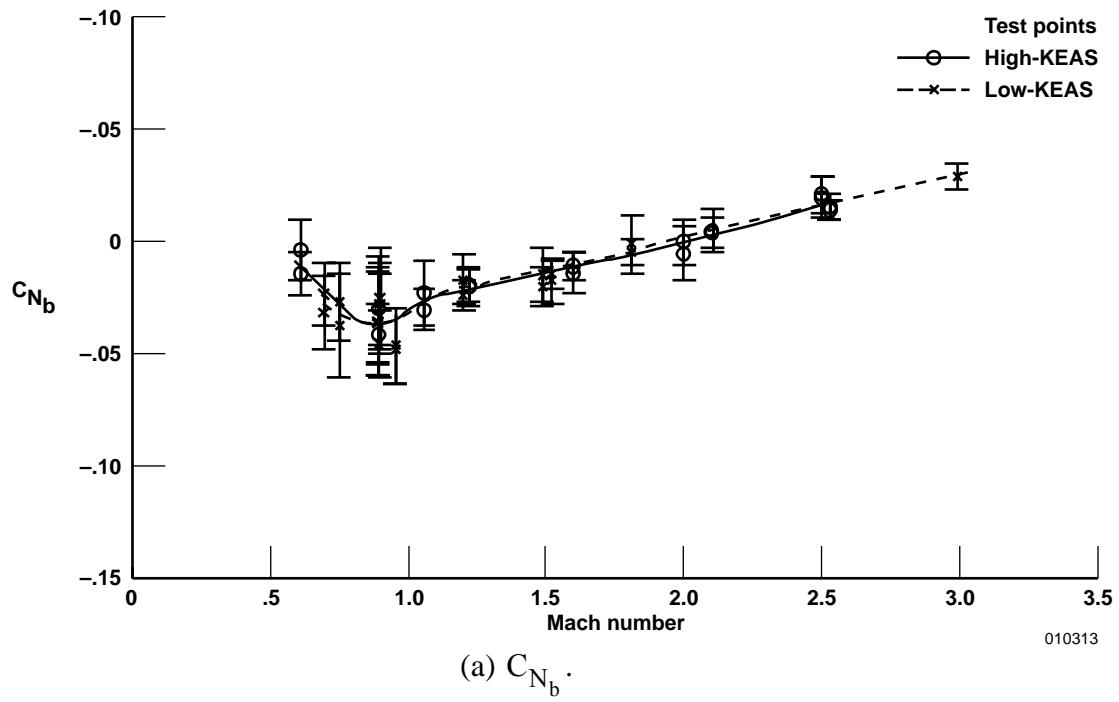
Figure 15. Flight-determined longitudinal coefficient biases (baseline configuration).

(a) C_{N_α}.
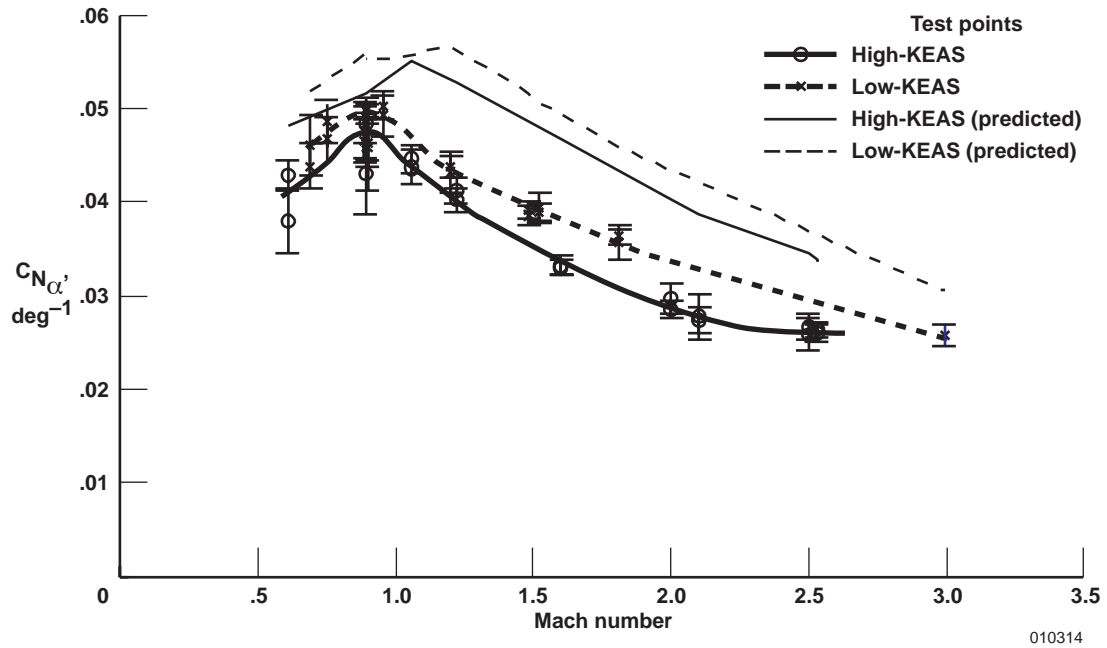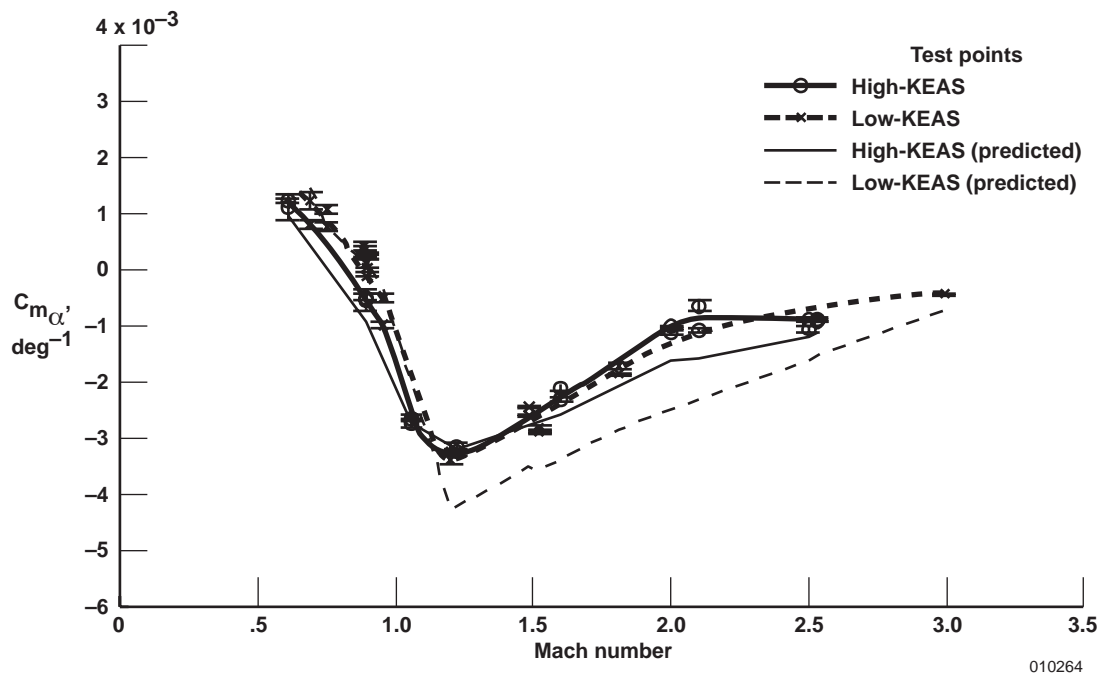
(b) C_{m_α} (moment reference at $0.25\,c$).

Figure 16. Predicted and flight-determined angle-of-attack derivatives (baseline configuration).
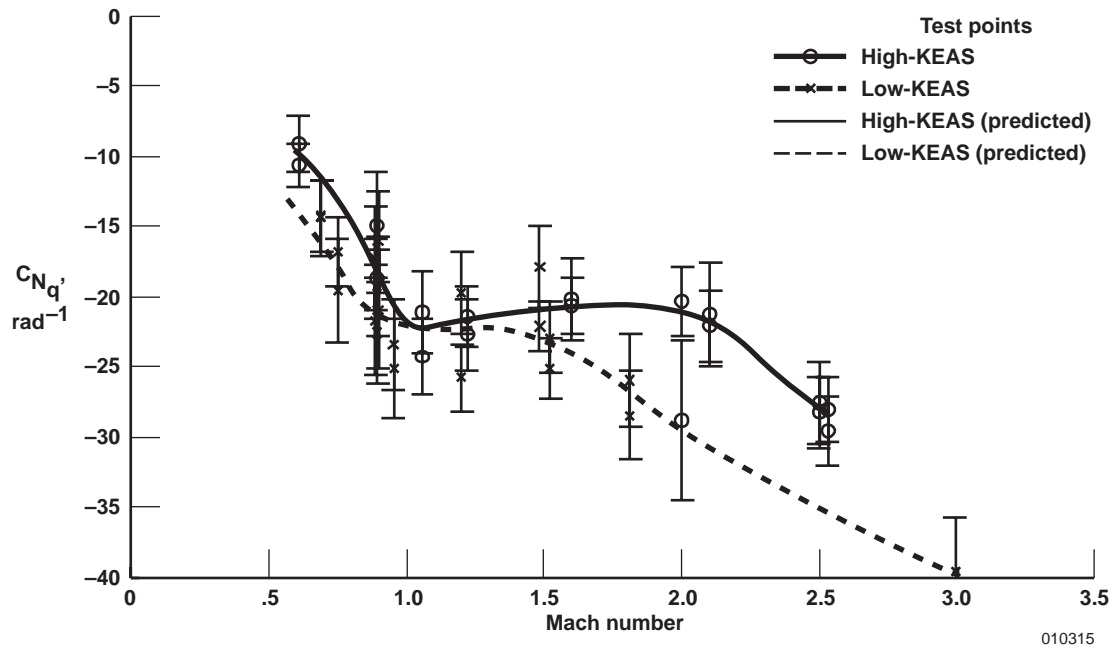
(a) C_{N_q}.
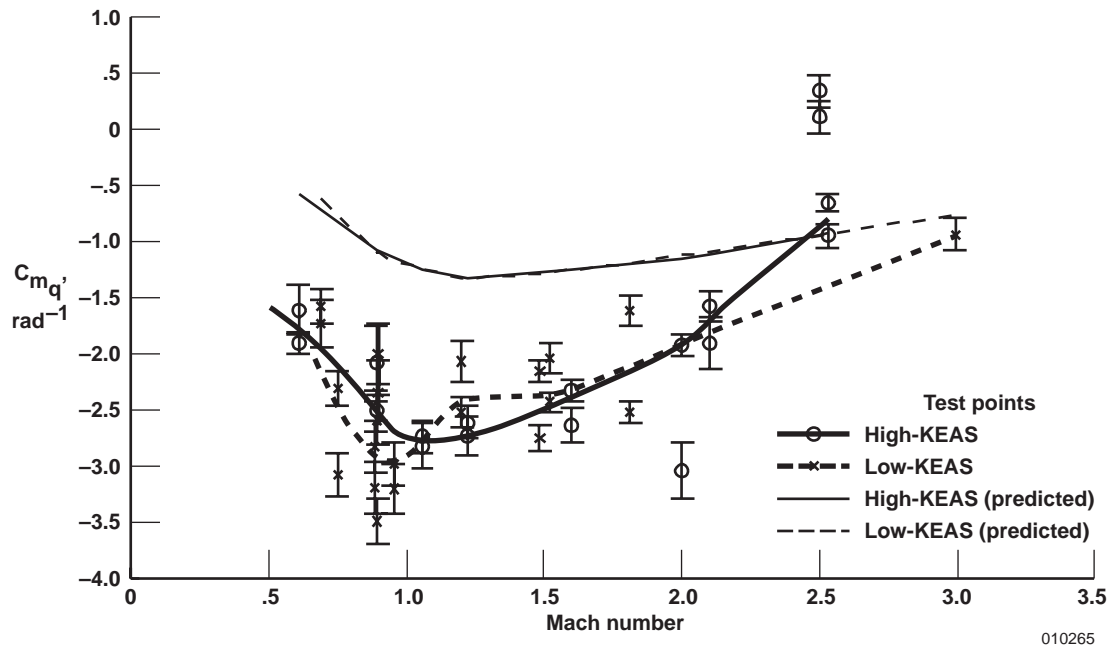
(b) C_{m_q} (moment reference at 0.25 c).

Figure 17. Predicted and flight-determined pitch-rate derivatives (baseline configuration).

43
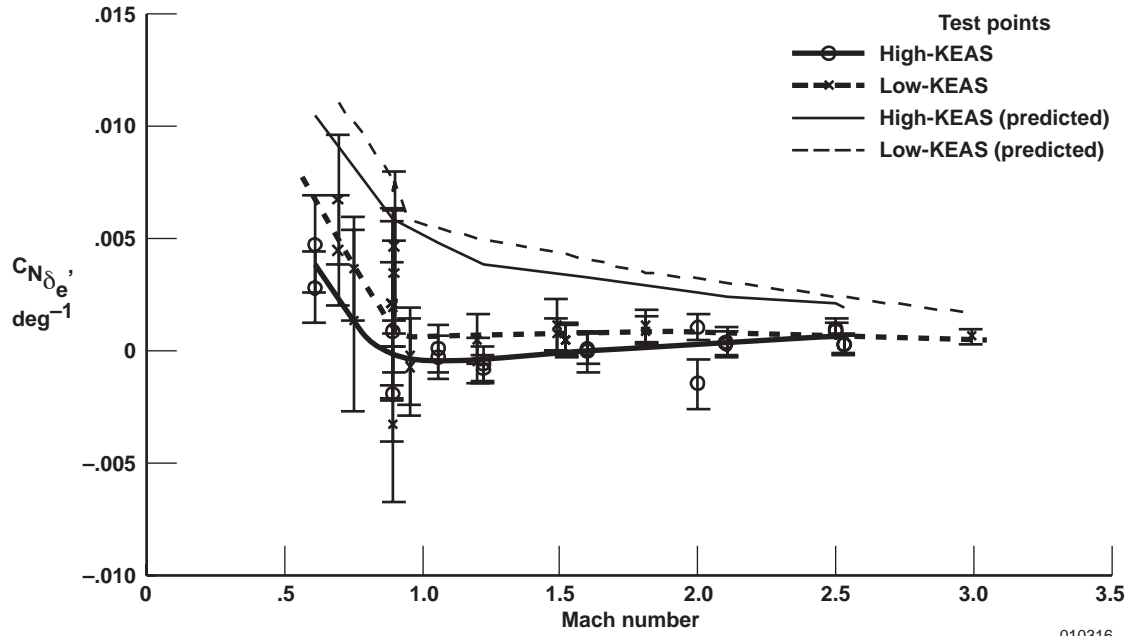
(a) $C_{N_{\delta_e}}$.
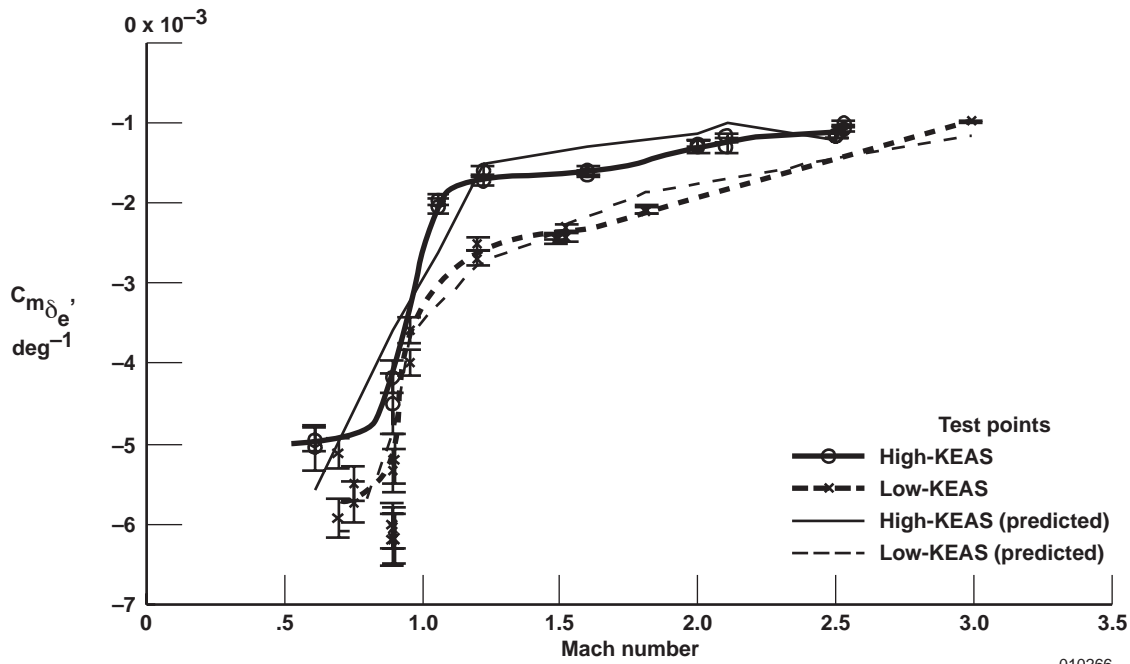
(b) $C_{m_{\delta_e}}$ (moment reference at 0.25 c).

Figure 18. Predicted and flight-determined elevator derivatives (baseline configuration).
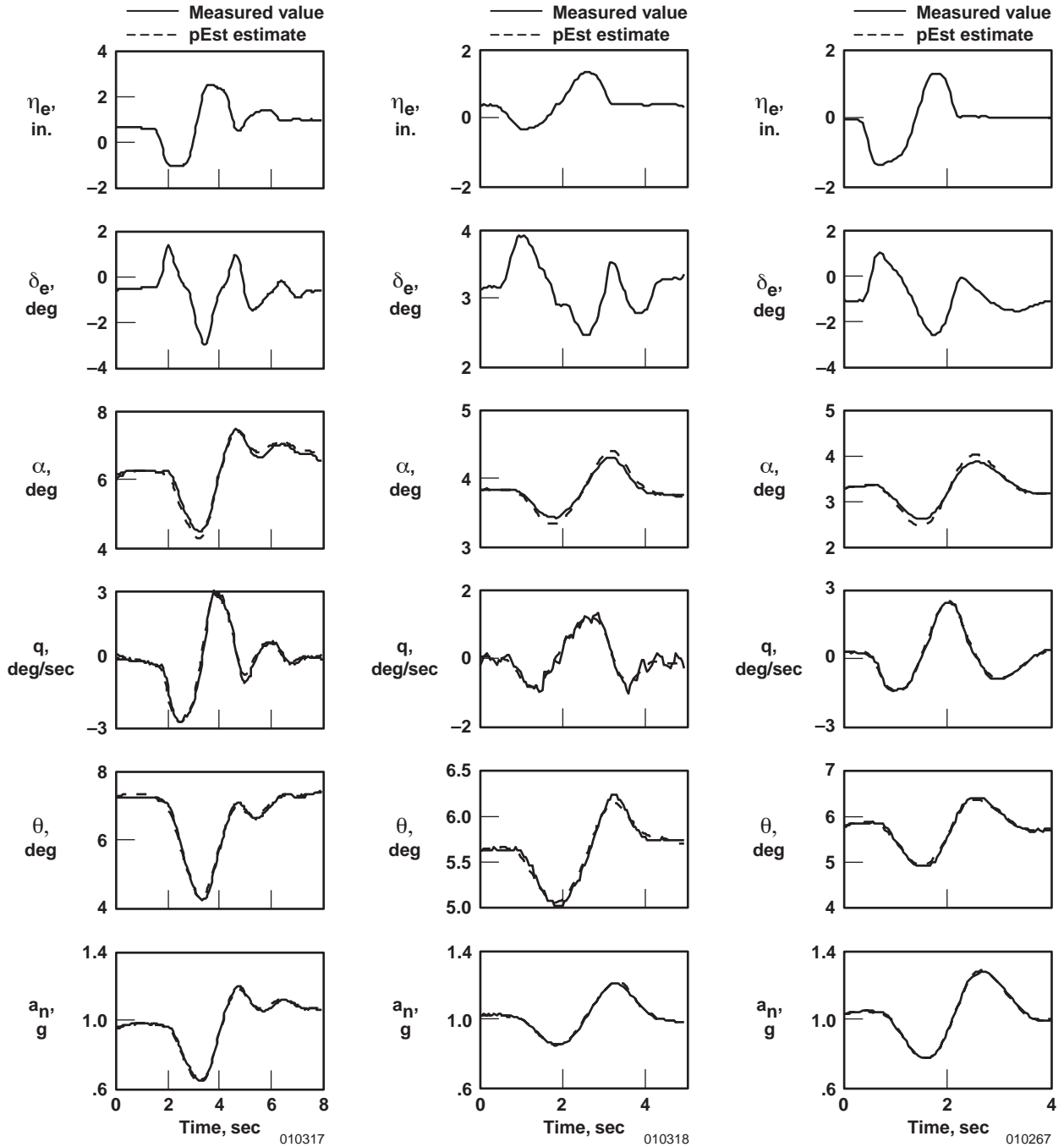
(a) Mach 0.5 and an altitude of 12,000 ft.

(b) Mach 1.03 and an altitude of 26,800 ft.

(c) Mach 1.73 and an altitude of 43,600 ft.

Figure 19. LASRE configuration longitudinal maneuver time histories.

45
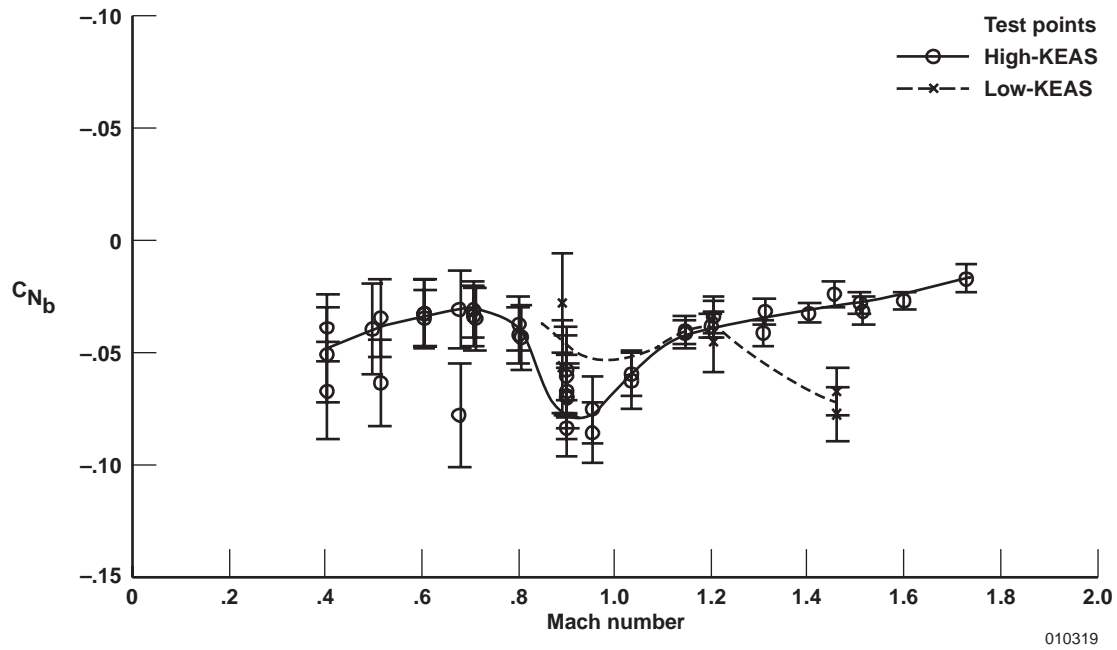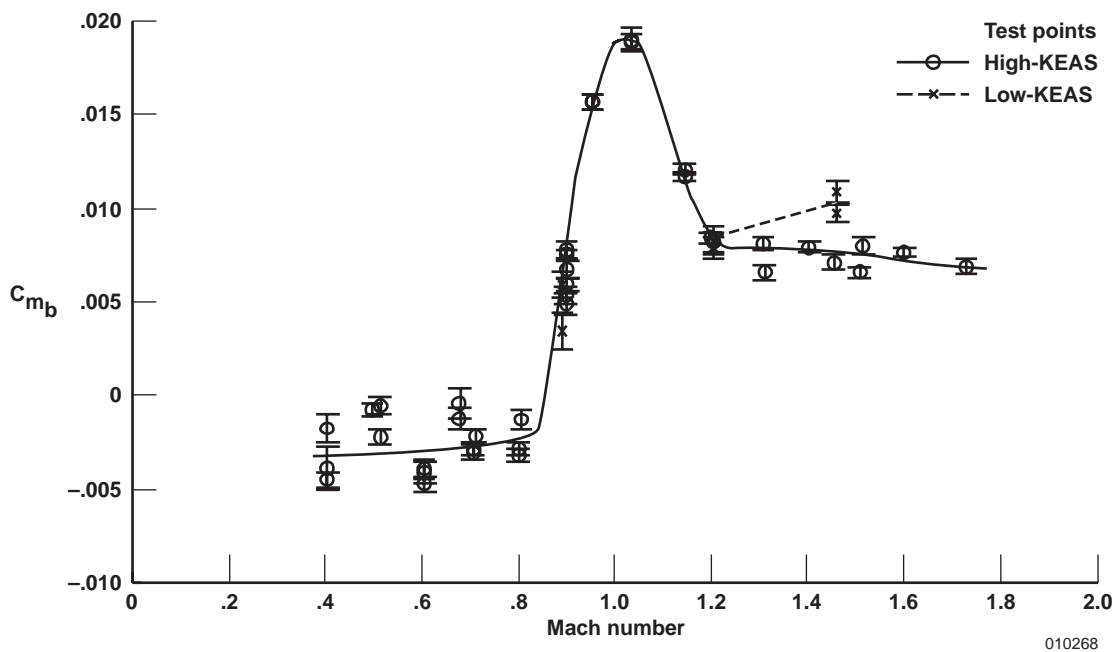
(a) C_{N_b}.

(b) C_{m_b}.

Figure 20. Flight-determined longitudinal coefficient biases (LASRE configuration).

(a) C_{N_α}.
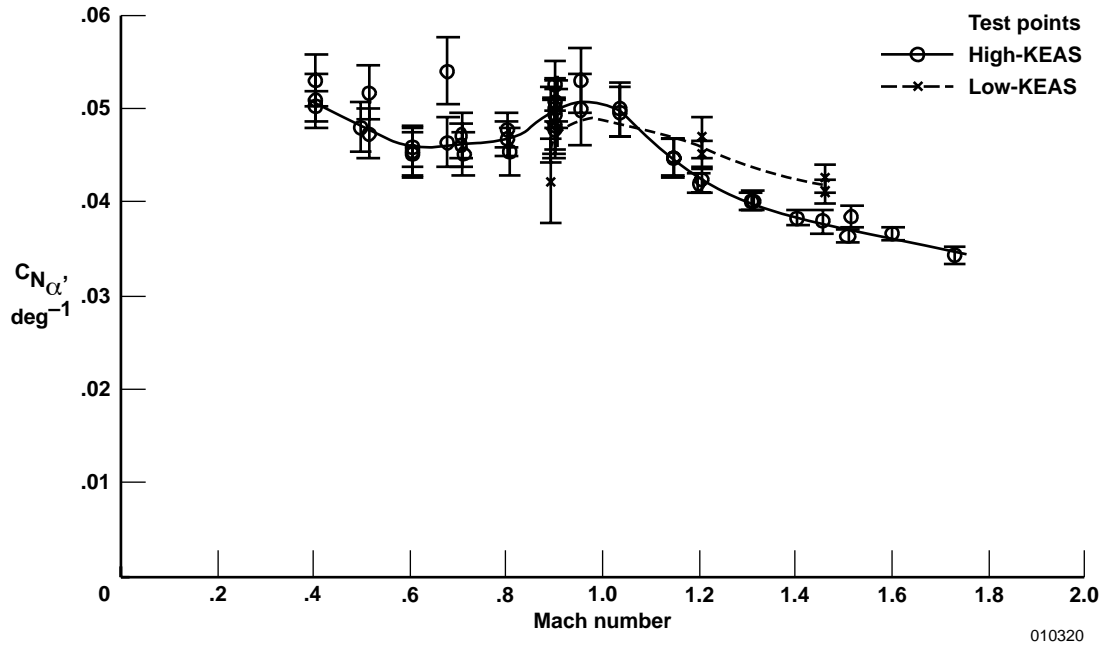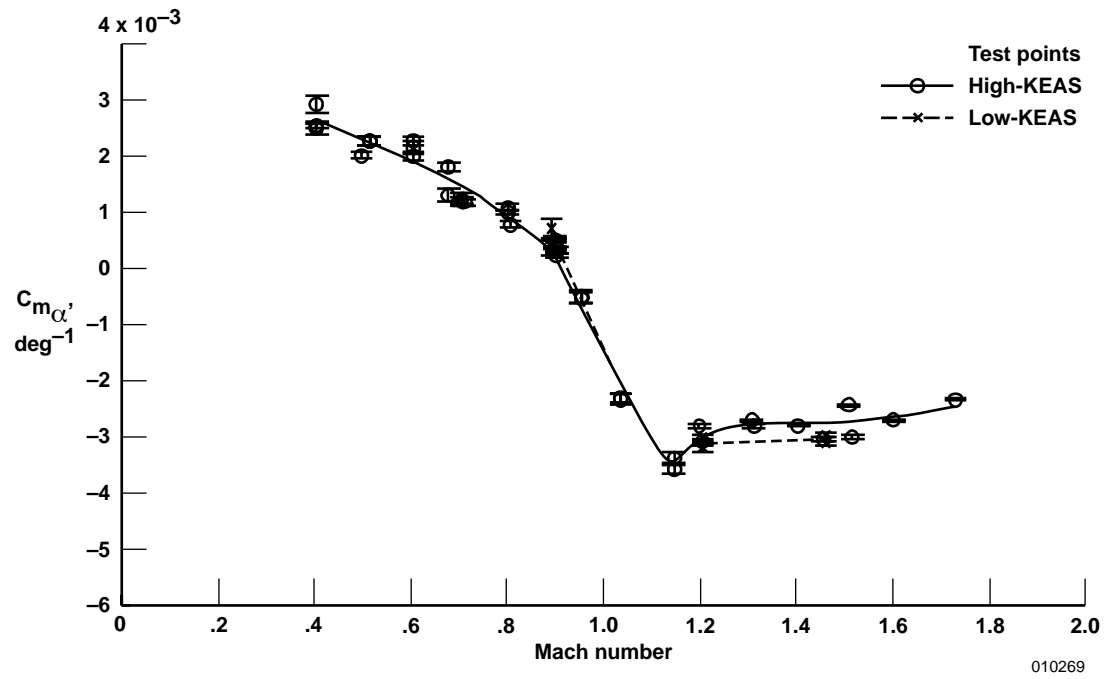
(b) C_{m_α} (moment reference at 0.25 c).

Figure 21. Flight-determined angle-of-attack derivatives (LASRE configuration).
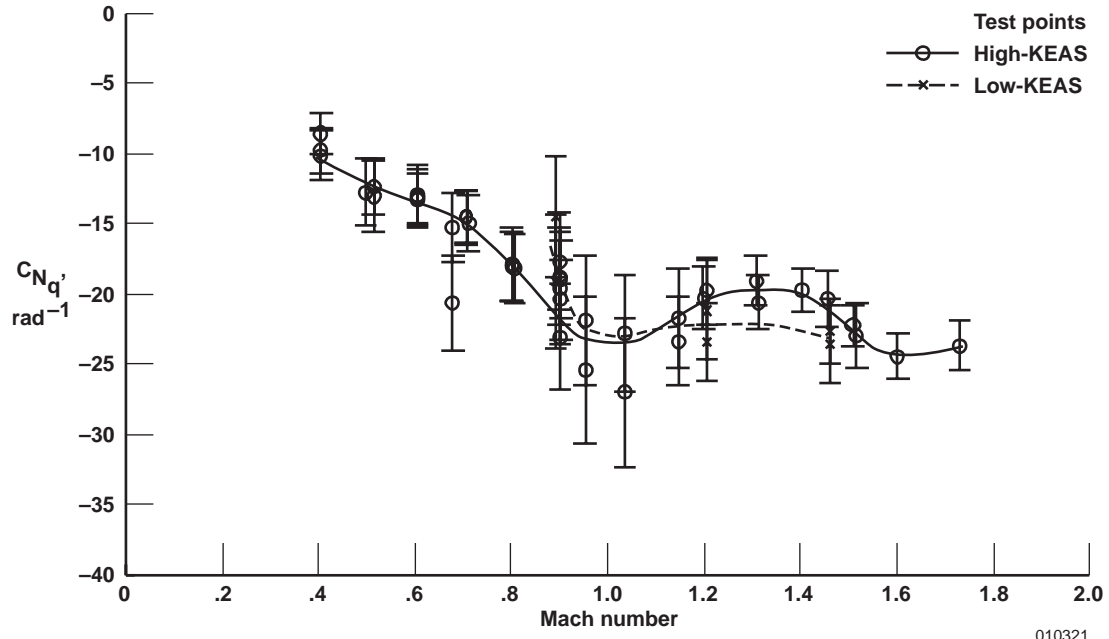
(a) C_{N_q}.
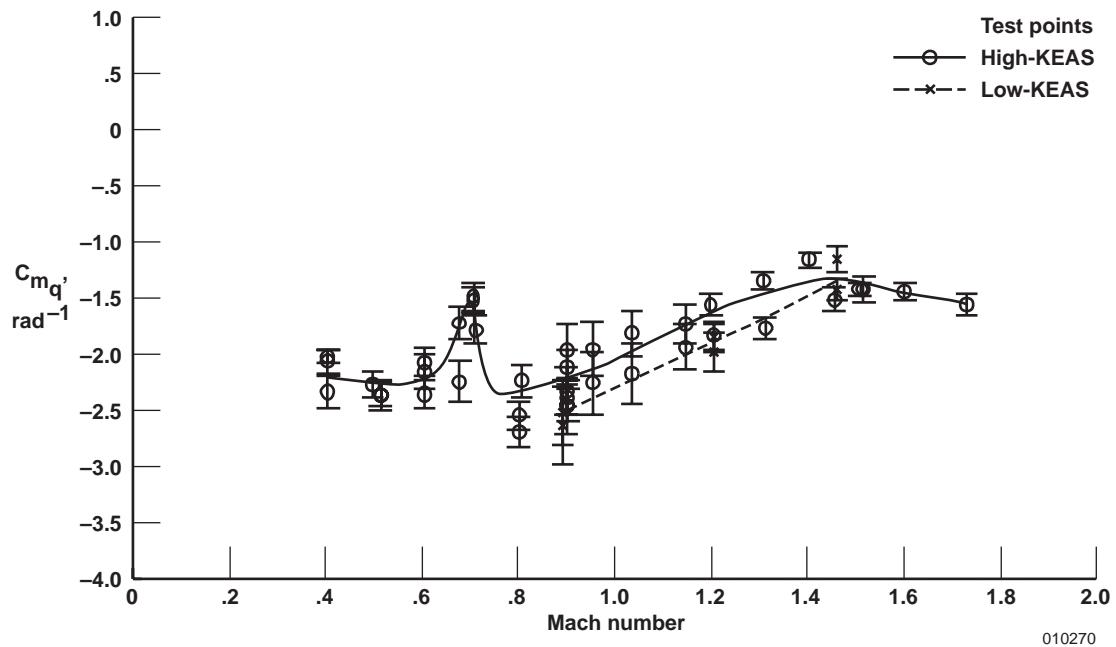
(b) C_{m_q} (moment reference at 0.25 c).

Figure 22. Flight-determined pitch rate derivatives (LASRE configuration).
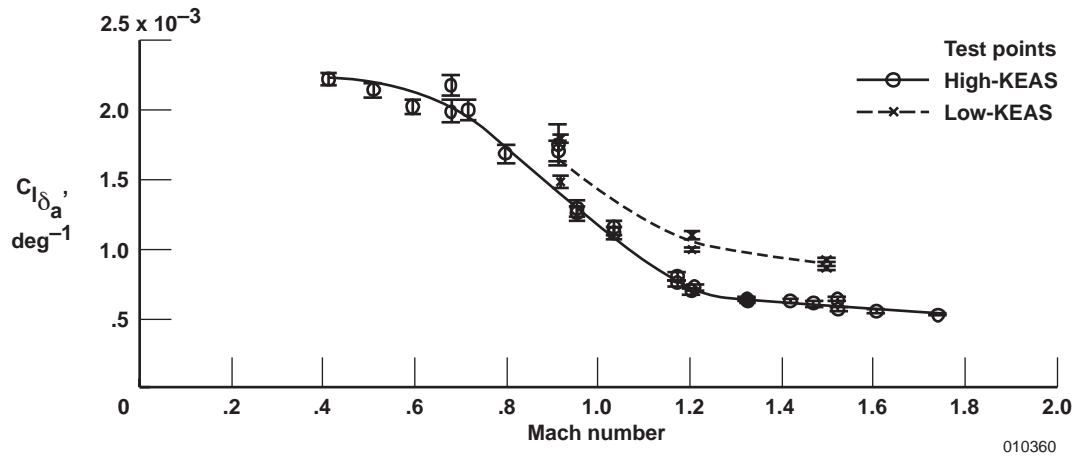
(a) $C_{N_{\delta_e}}$.

(b) $C_{m_{\delta_e}}$ (moment reference at 0.25 c).
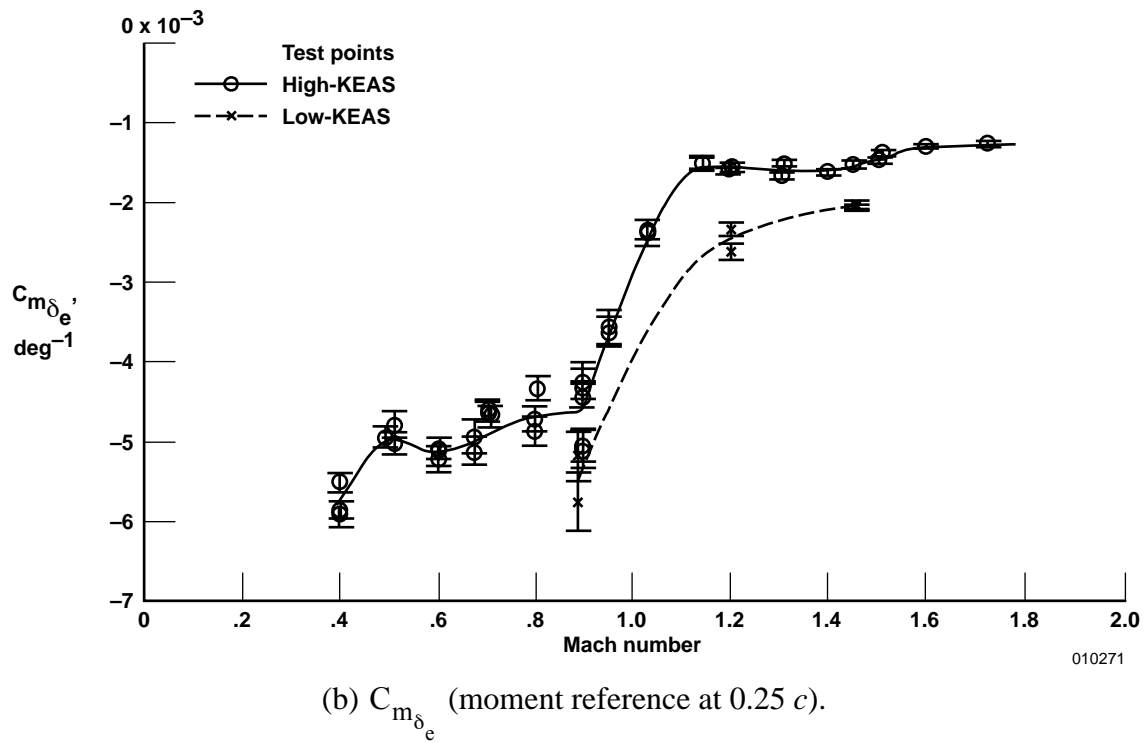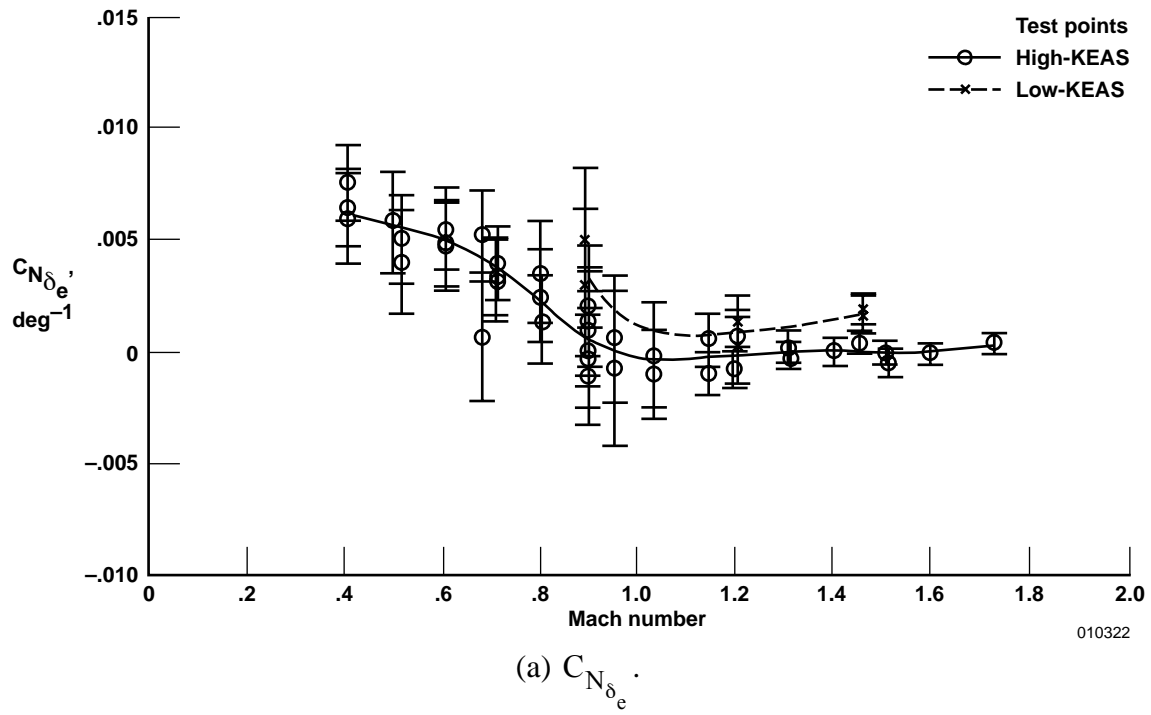
Figure 23. Flight-determined elevator derivatives (LASRE configuration).
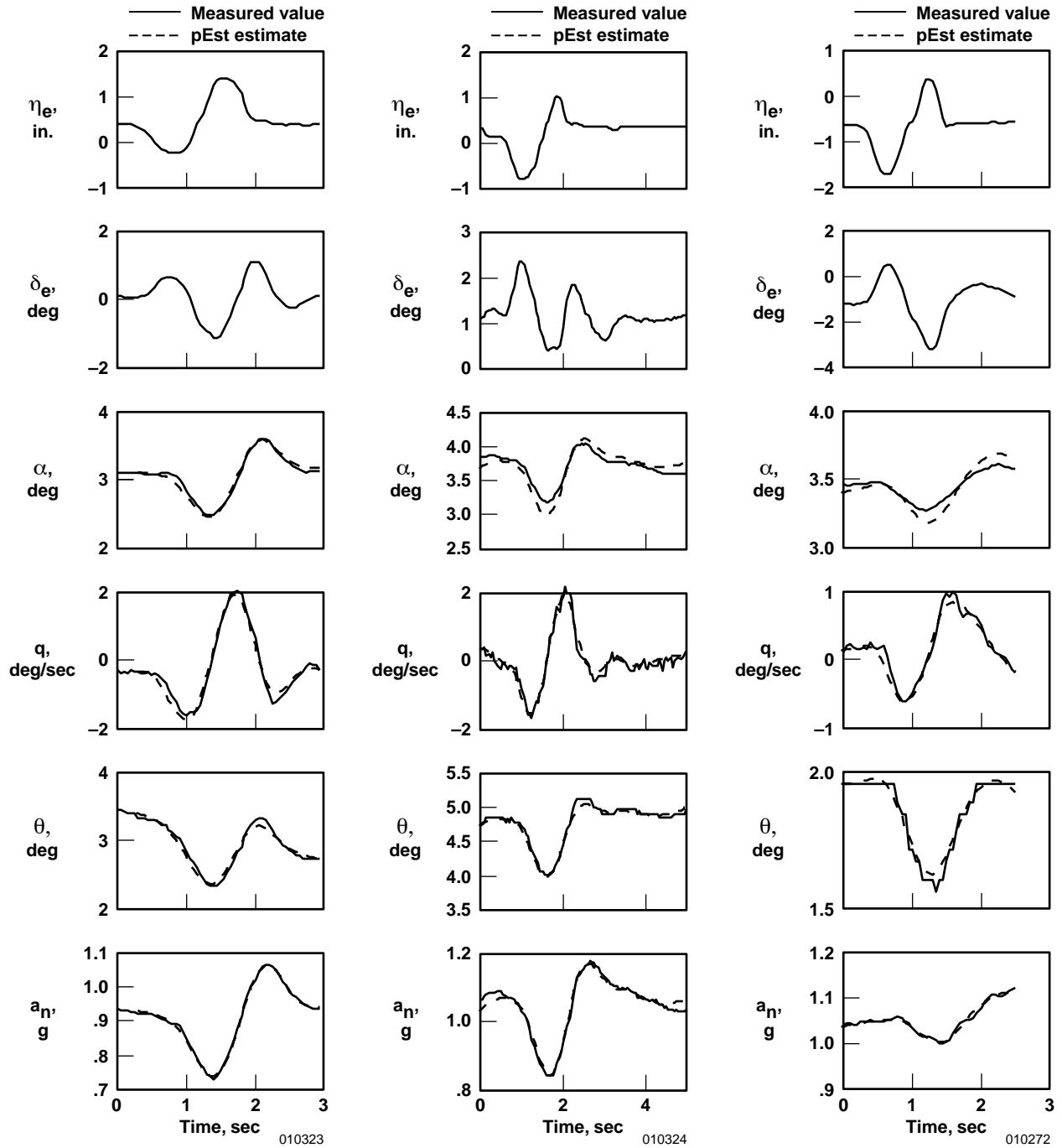
(a) Mach 0.67 and an altitude of 7,100 ft.

(b) Mach 0.97 and an altitude of 25,100 ft.

(c) Mach 3.02 and an altitude of 67,900 ft.

Figure 24. Test bed configuration longitudinal maneuver time histories.
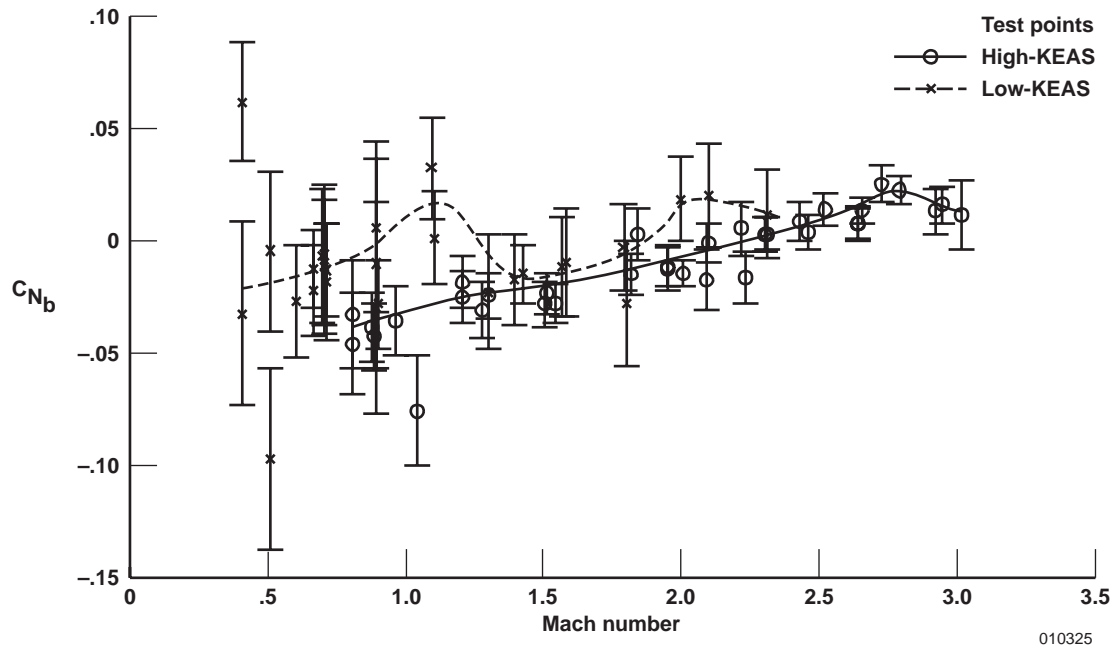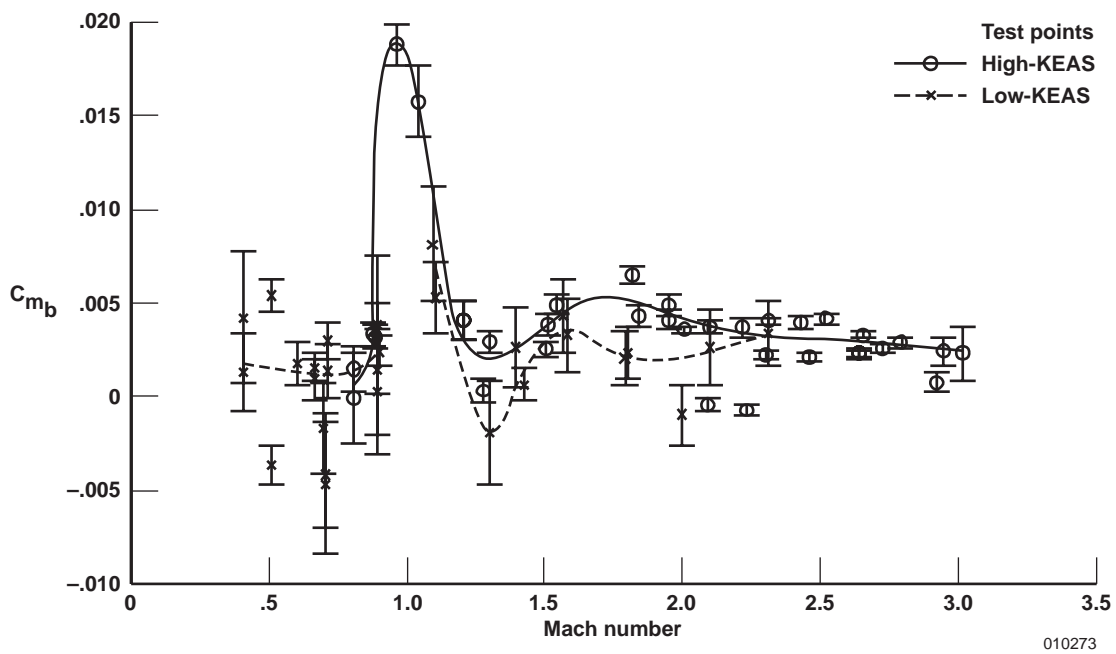
(a) C_{N_b}.

(b) C_{m_b}.

Figure 25. Flight-determined longitudinal coefficient biases (test bed configuration).

(a) C_{N_α}.
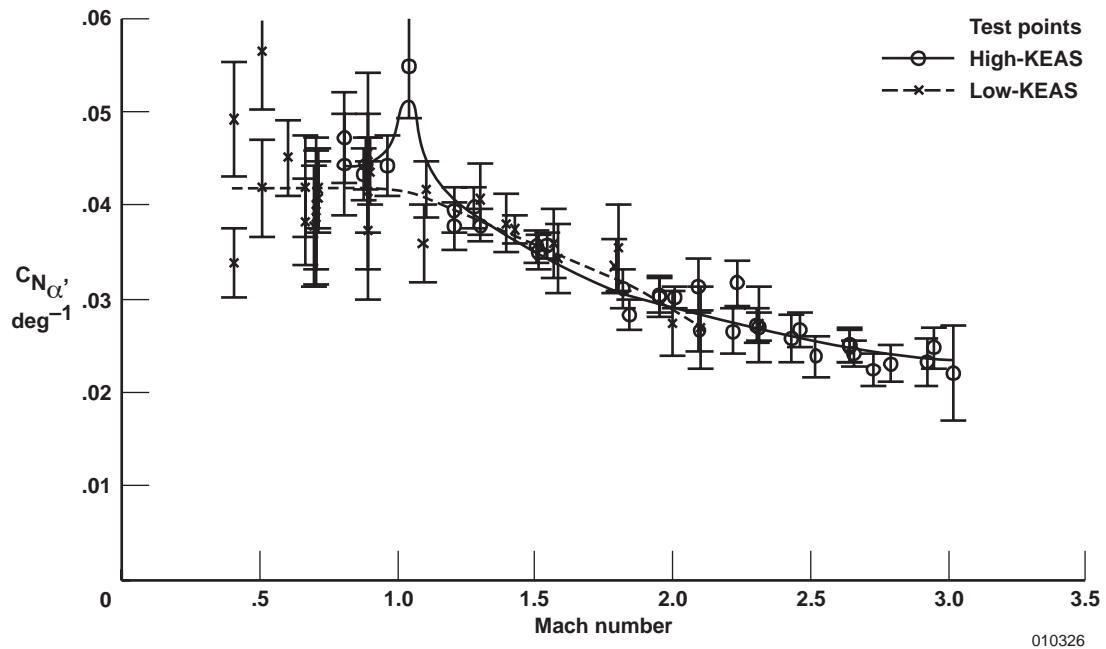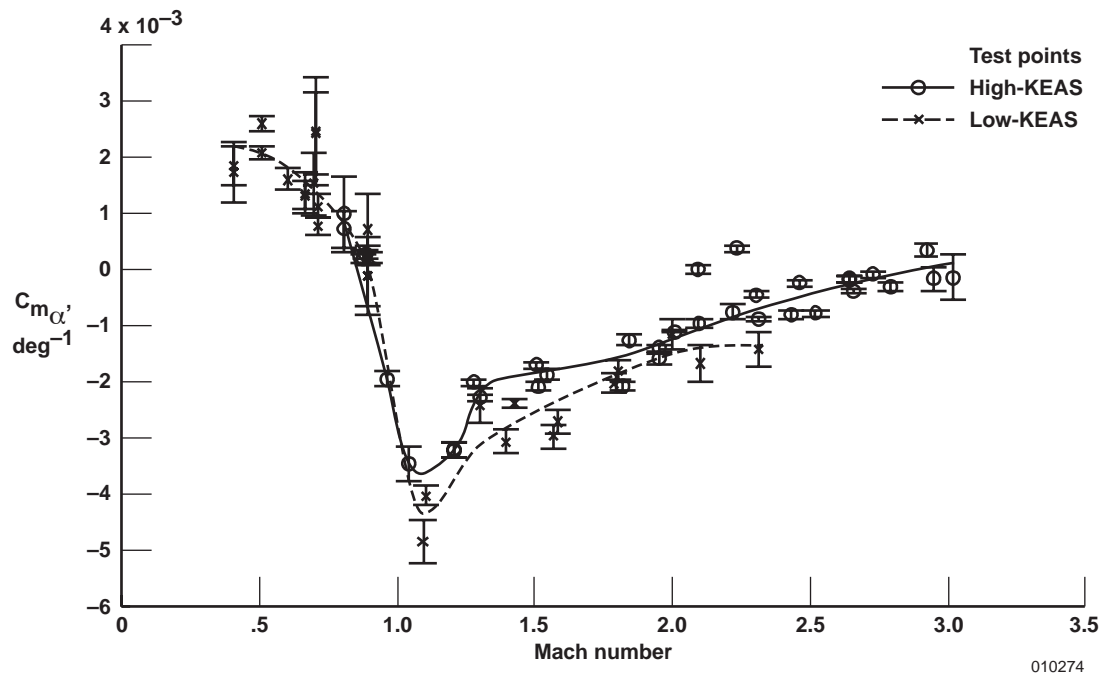
(b) C_{m_α} (moment reference at 0.25 c).

Figure 26. Flight-determined angle-of-attack derivatives (test bed configuration).
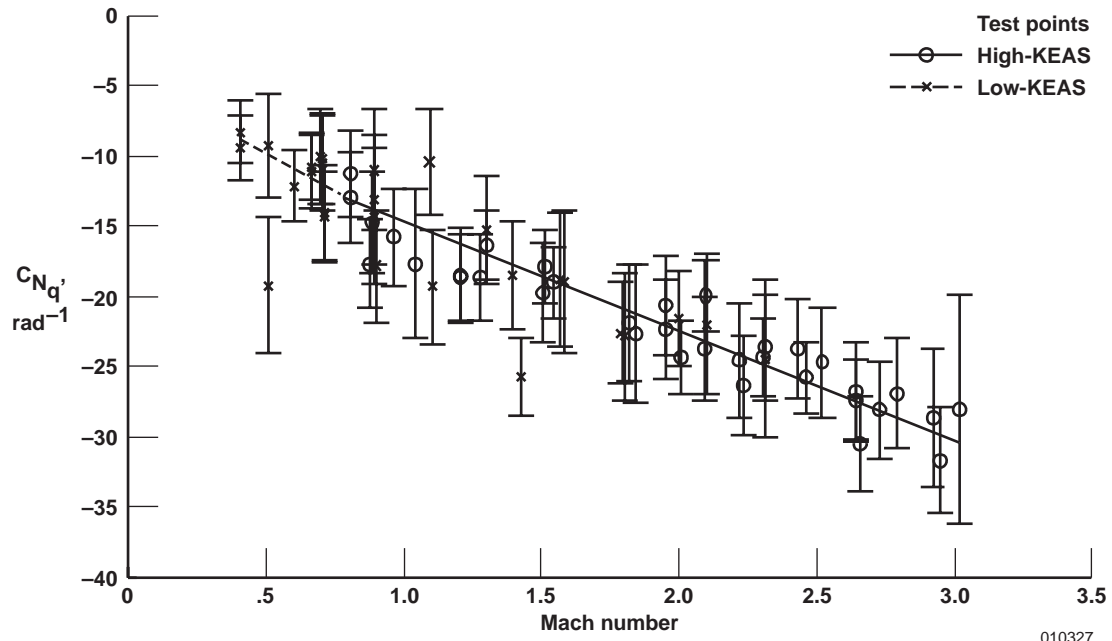
(a) C_{N_q}.
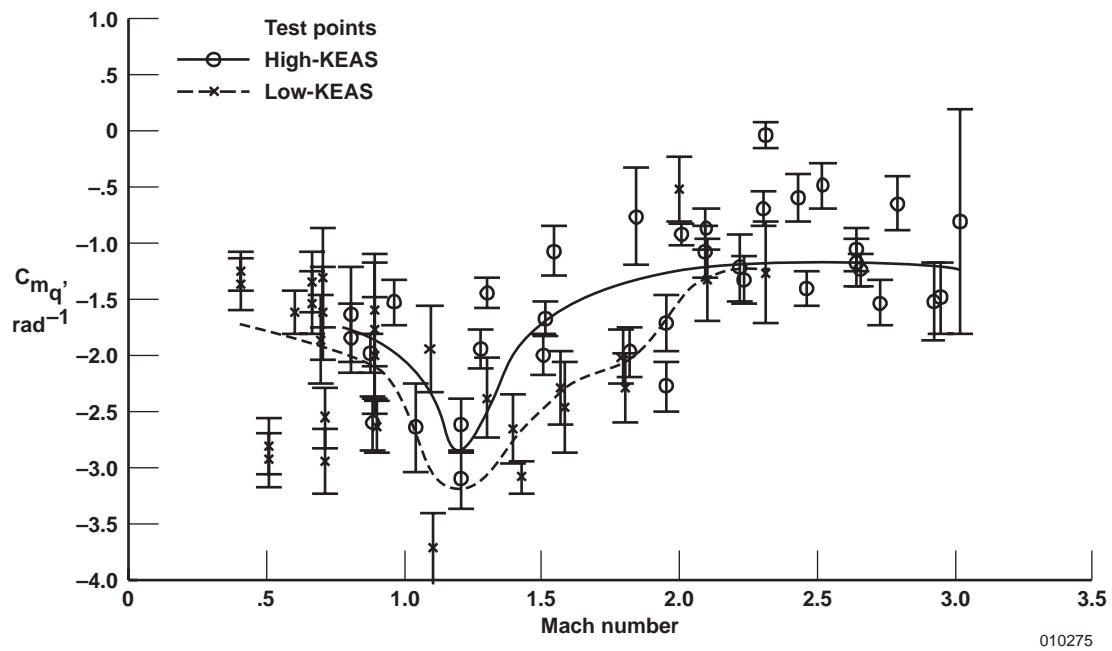
(b) C_{m_q} (moment reference at 0.25 c).

Figure 27. Flight-determined pitch-rate derivatives (test bed configuration).
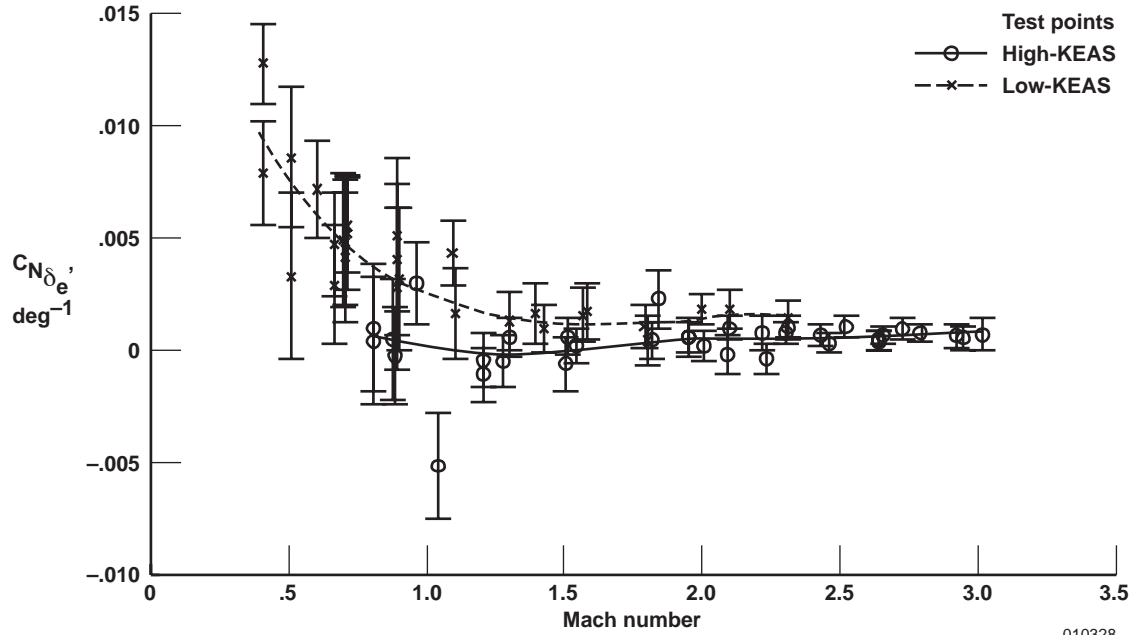
(a) $C_{N_{\delta_e}}$.
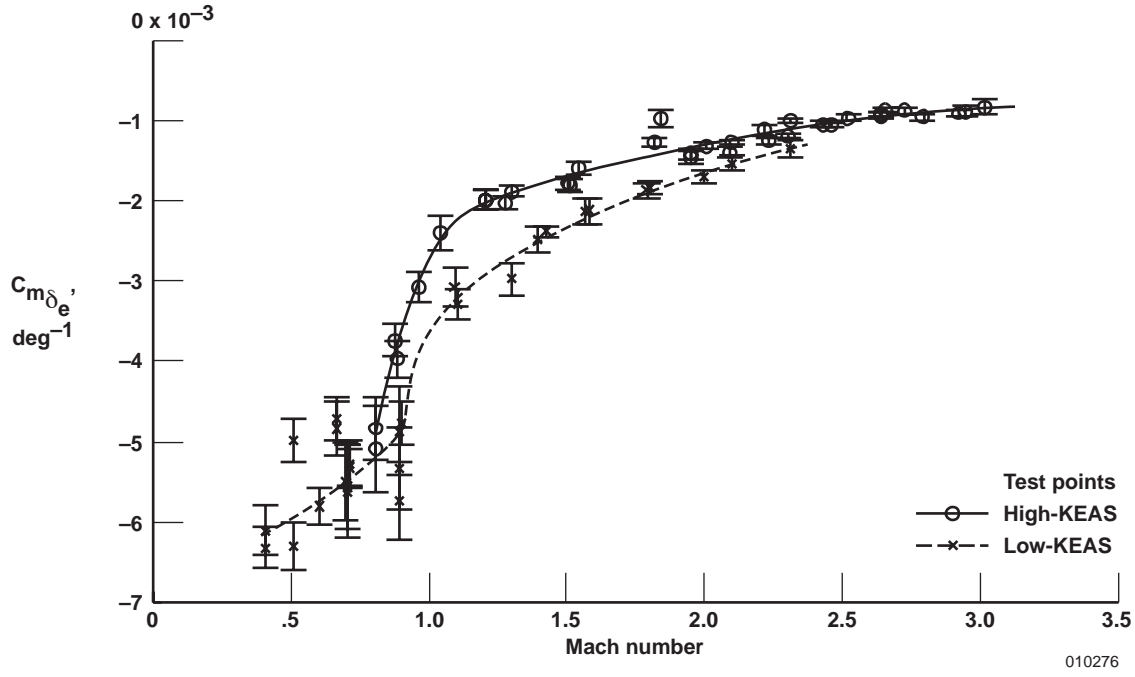
(b) $C_{m_{\delta_e}}$ (moment reference at 0.25 c).

Figure 28. Flight-determined elevator derivatives (test bed configuration).
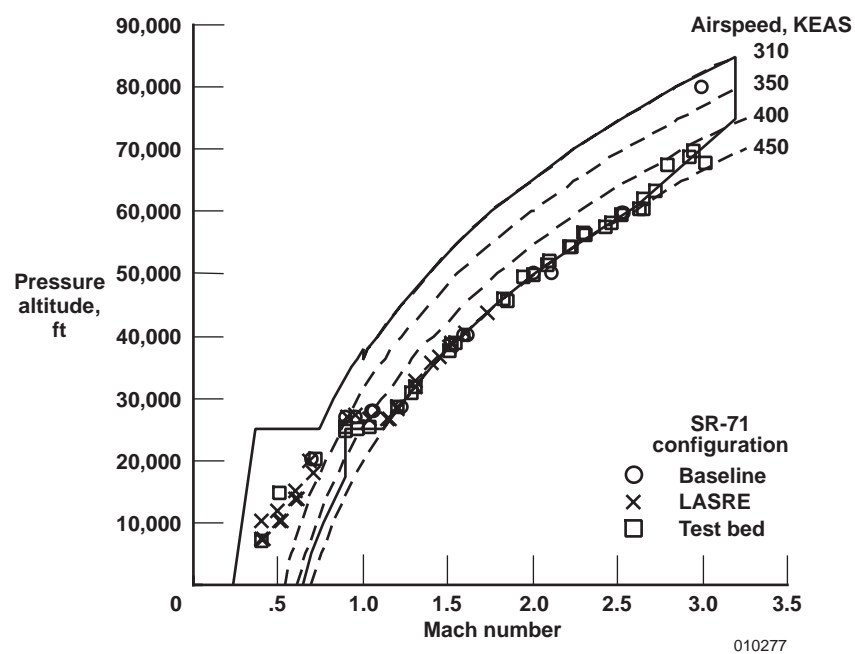
Figure 29. Flight conditions for comparison of configuration longitudinal stability and control derivatives.
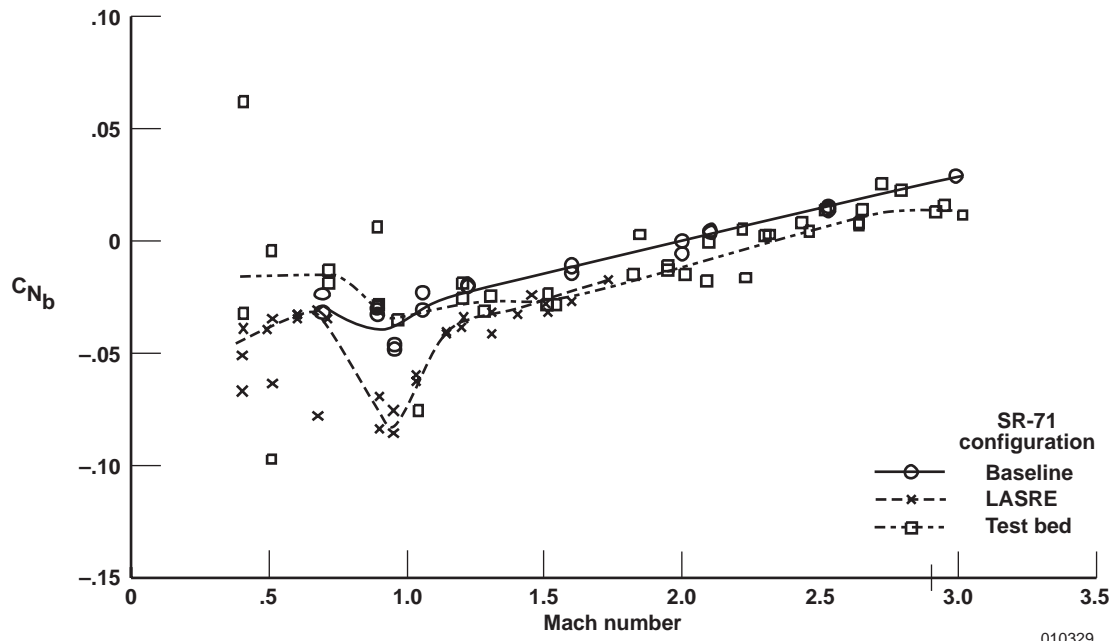
(a) C_{N_b}.
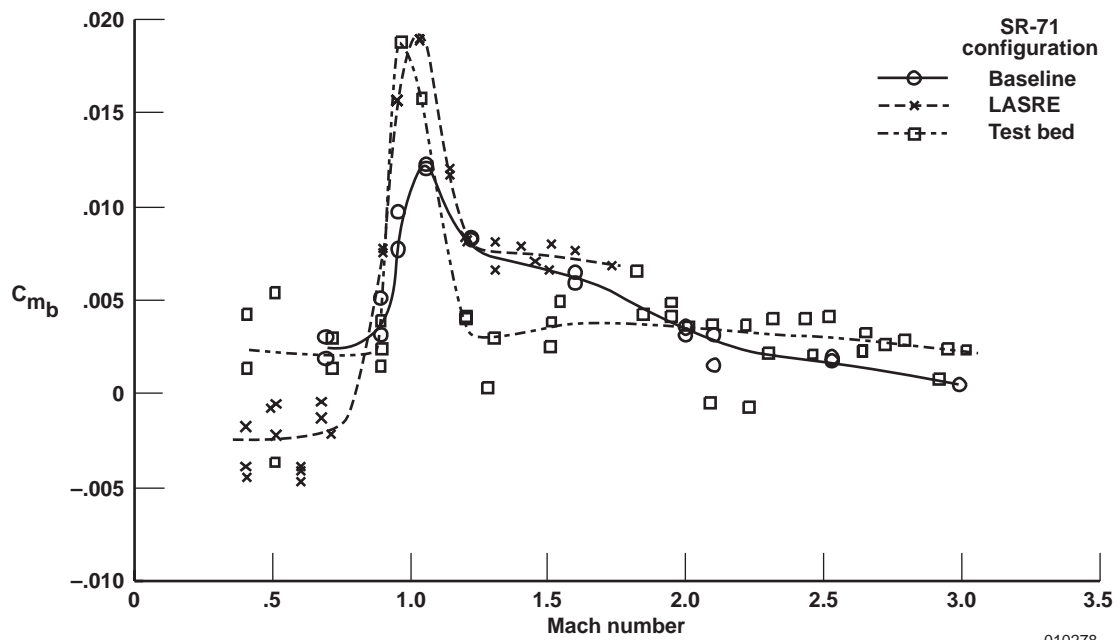
(b) C_{m_b}.

Figure 30. Flight-determined longitudinal coefficient biases (all three configurations).

(a) C_{N_α}.

(b) C_{m_α} (moment reference at 0.25 c).
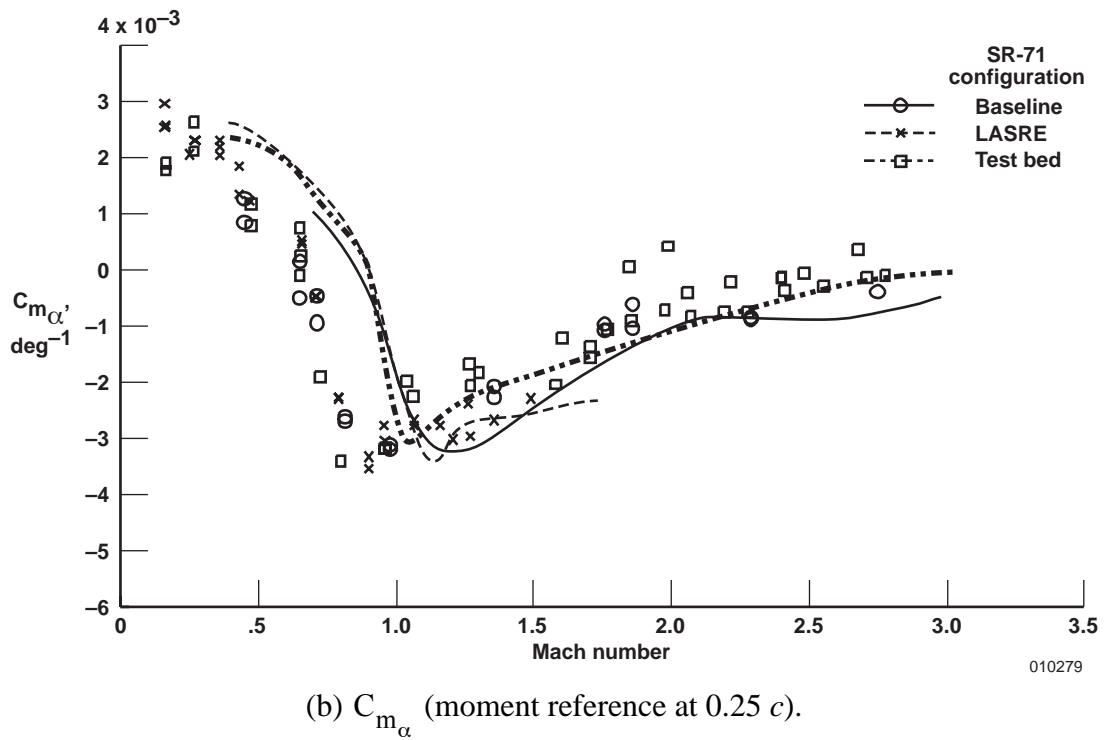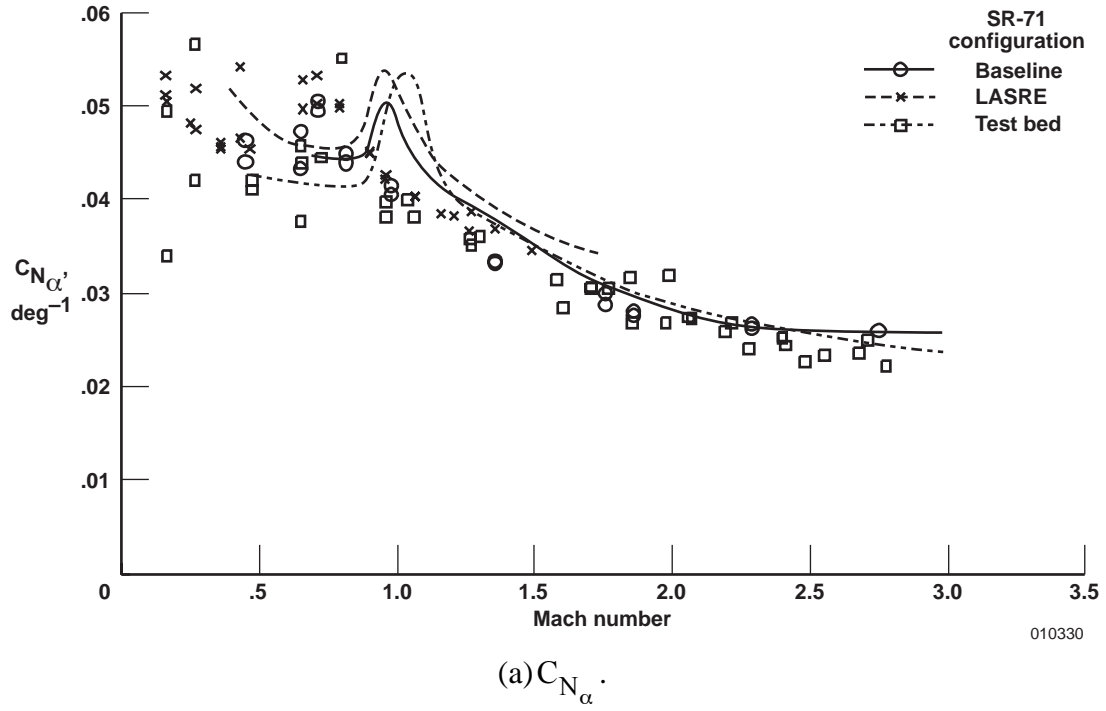
Figure 31. Flight-determined angle-of-attack derivatives (all three configurations).
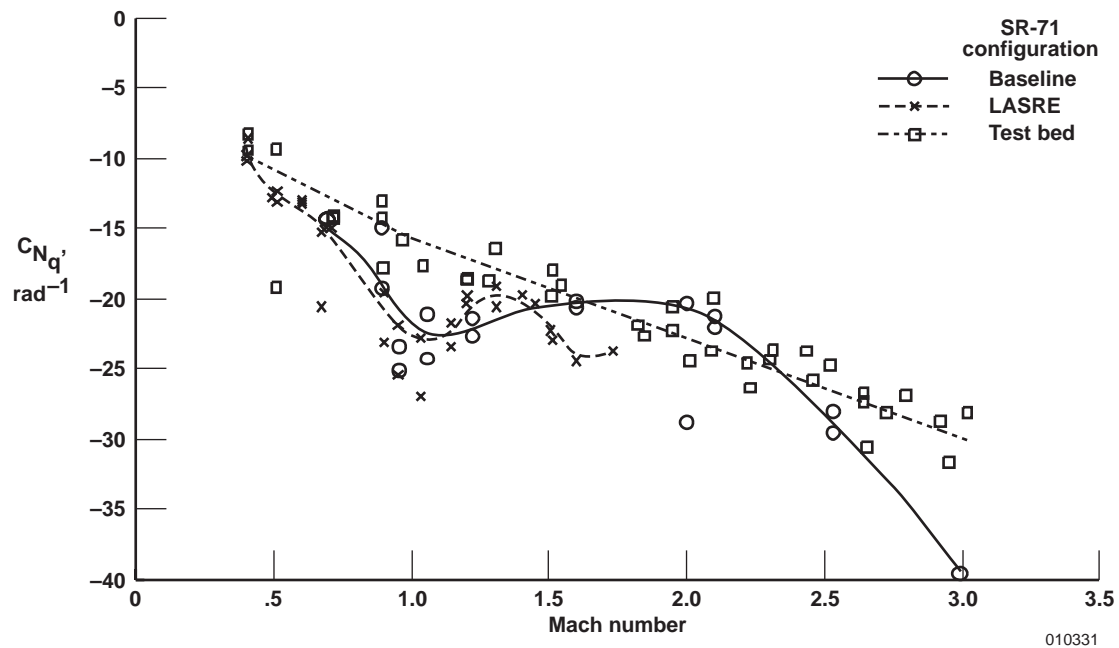
(a) C_{N_q}.
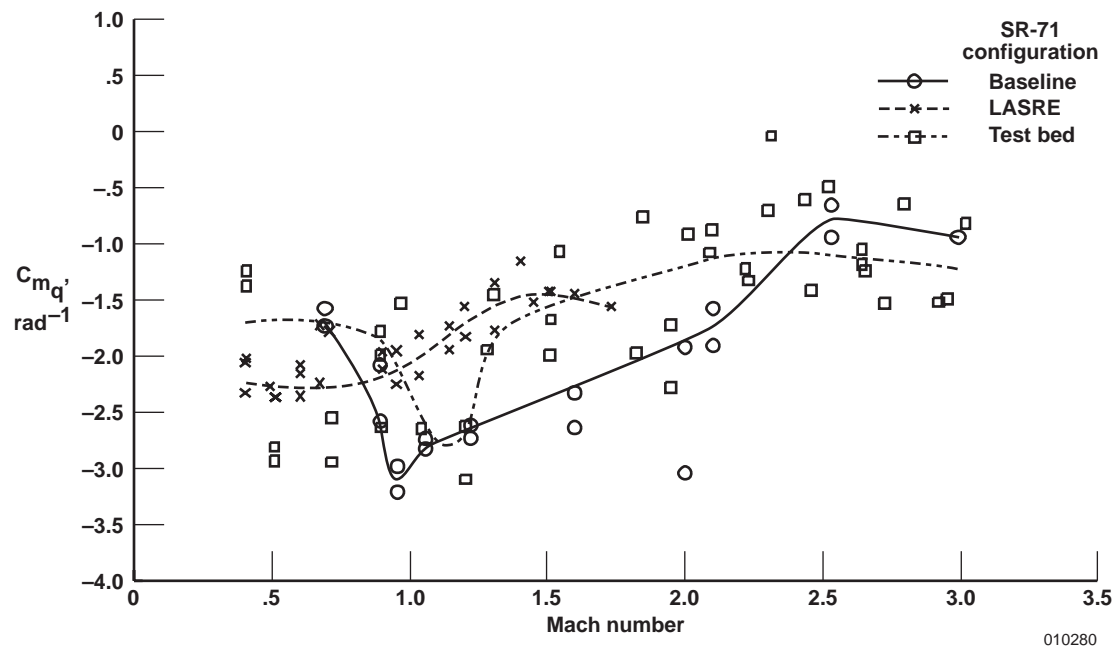
(b) C_{m_q} (moment reference at 0.25 c).

Figure 32. Flight-determined pitch-rate derivatives (all three configurations).
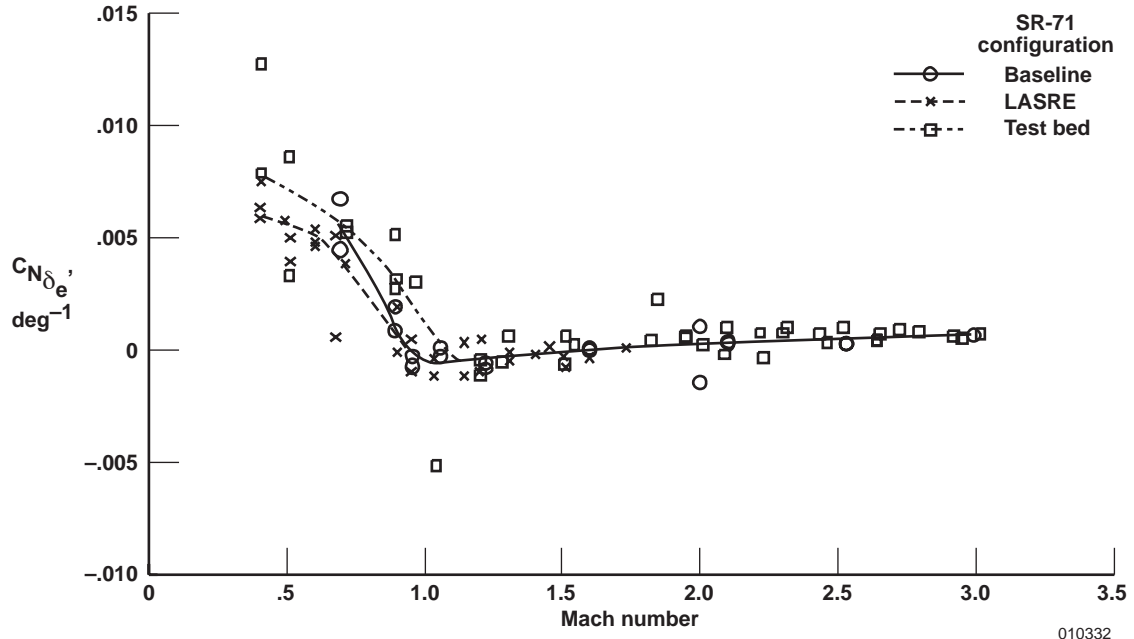
(a) $C_{N_{\delta_e}}$.
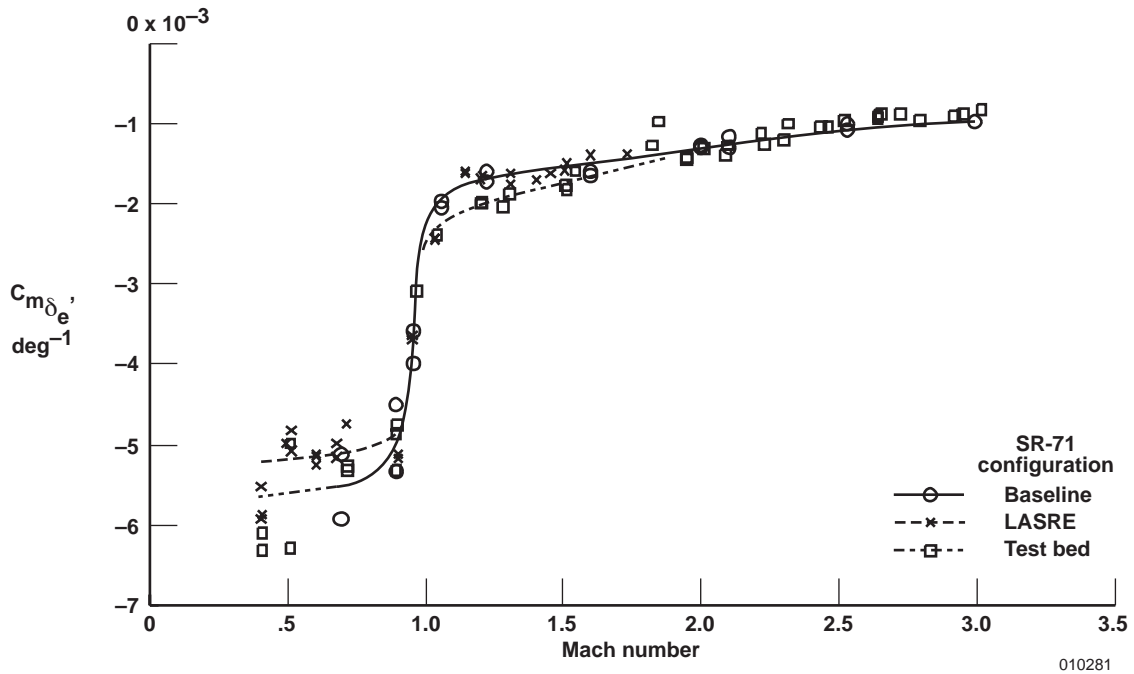
(b) $C_{m_{\delta_e}}$ (moment reference at $0.25\ c$).

Figure 33. Flight-determined elevator derivatives (all three configurations).

(a) Mach 0.61 and an altitude of 6,100 ft.

(b) Mach 1.07 and an altitude of 27,900 ft.

(c) Mach 2.97 and an altitude of 79,800 ft.
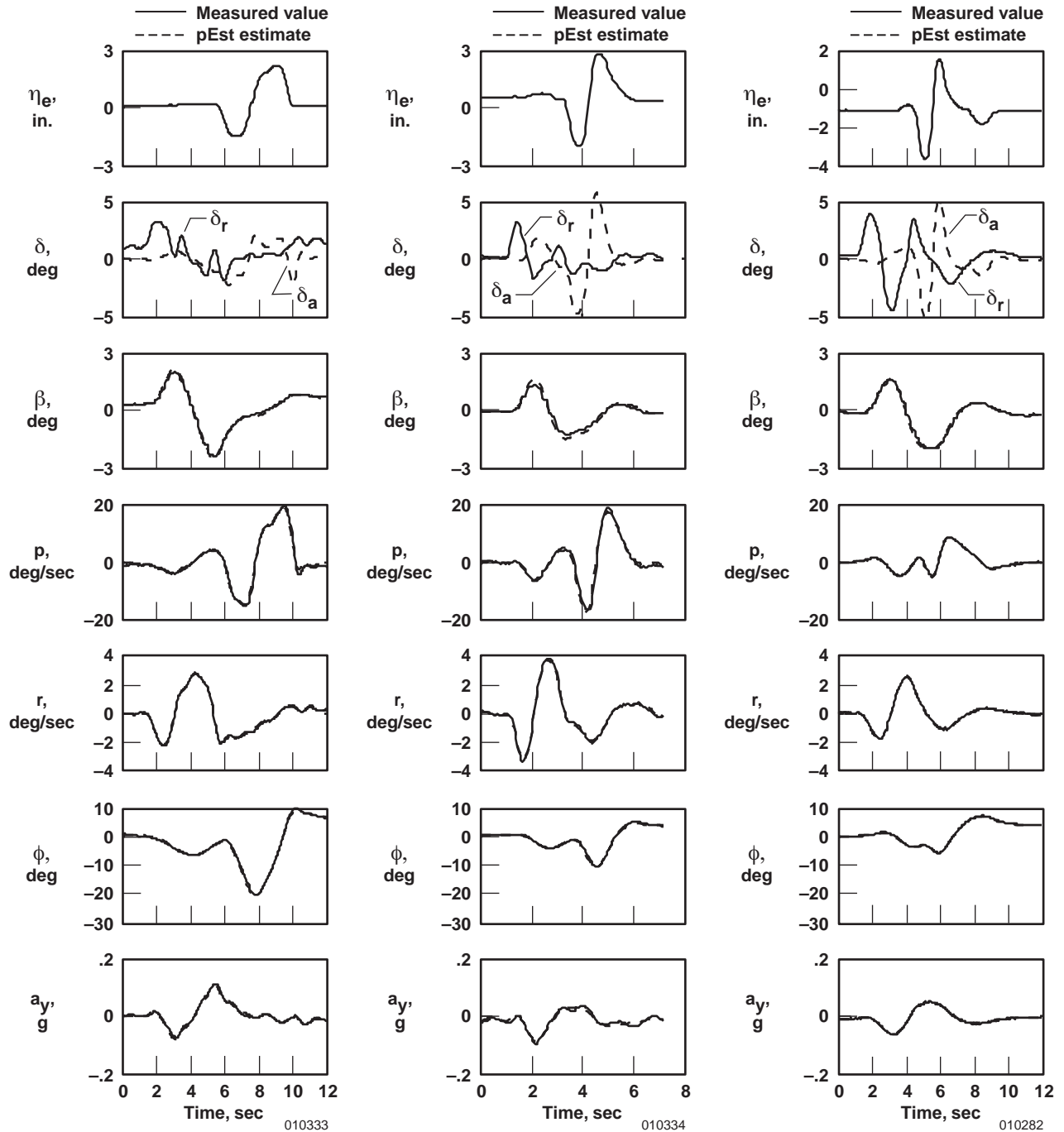
Figure 34. Baseline configuration lateral-directional maneuver time histories.
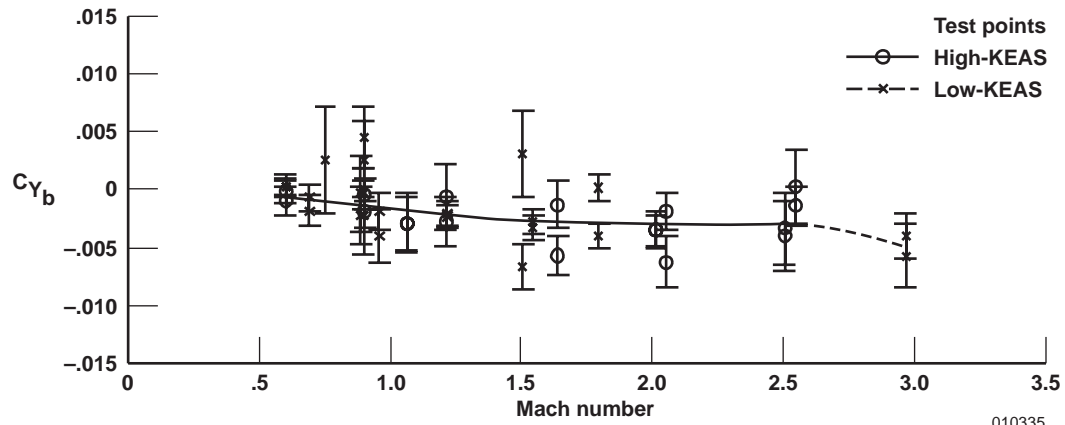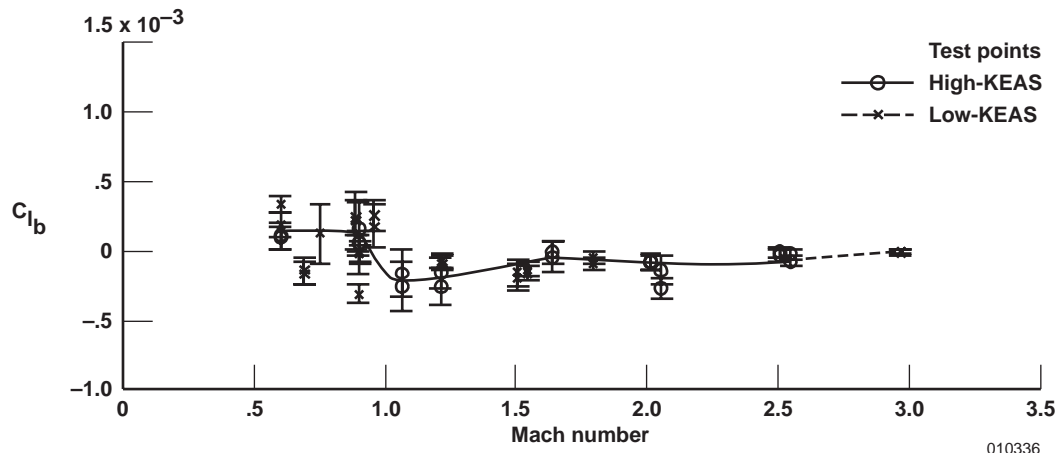
(a) C_{Y_b}.

(b) C_{l_b}.
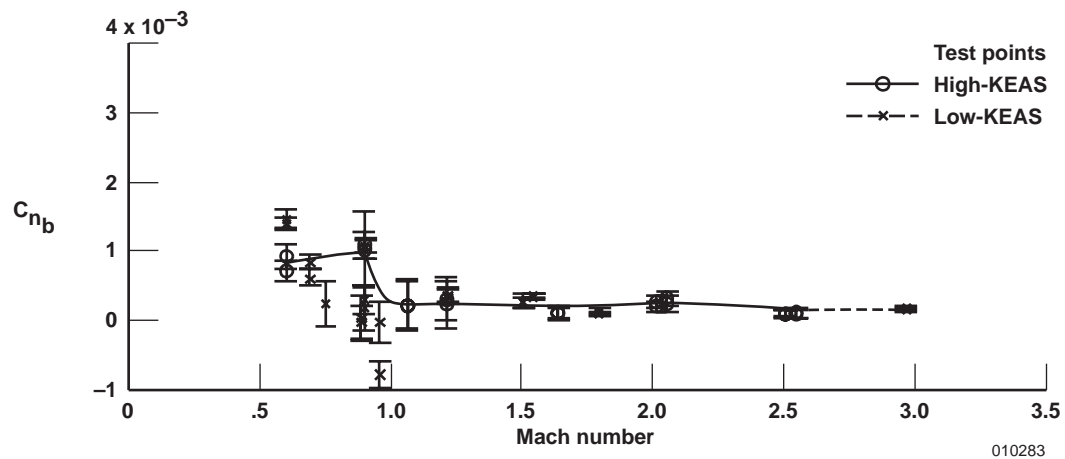
(c) C_{n_b}.

Figure 35. Flight-determined lateral-directional coefficient biases (baseline configuration).

(a) C_{Y_β}.

(b) C_{l_β}.
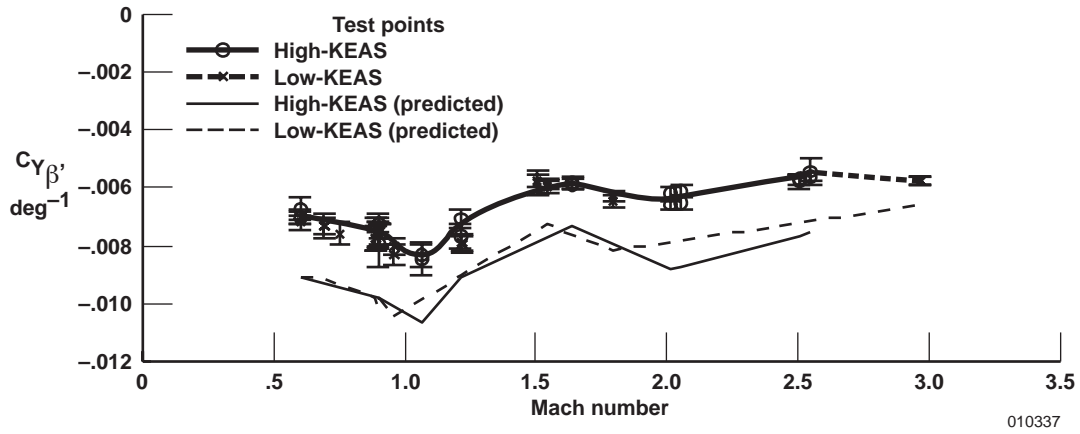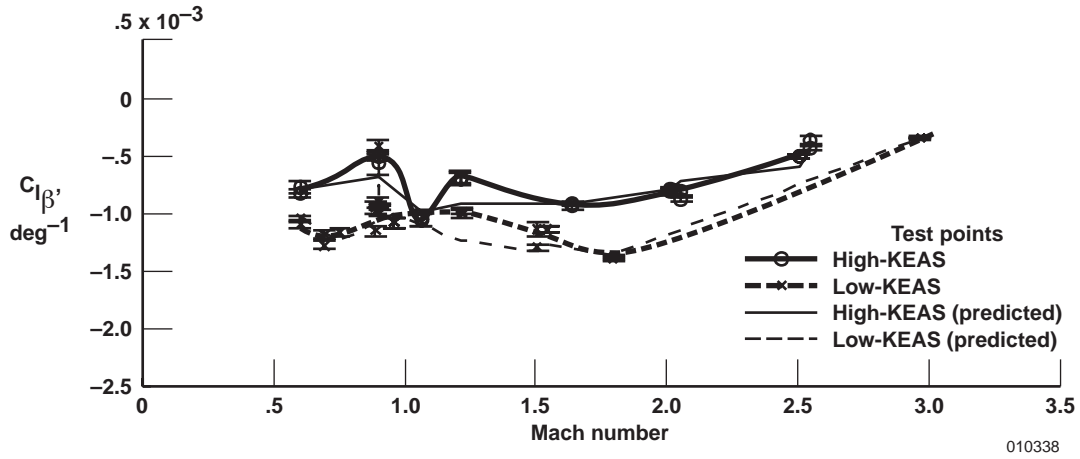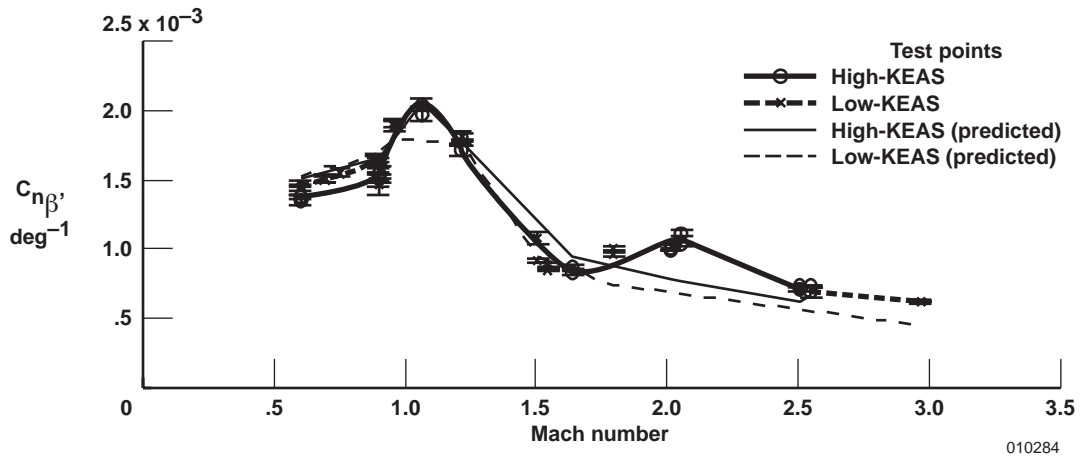
(c) C_{n_β} (moment reference at 0.25 c).

Figure 36. Predicted and flight-determined angle-of-sideslip derivatives (baseline configuration).
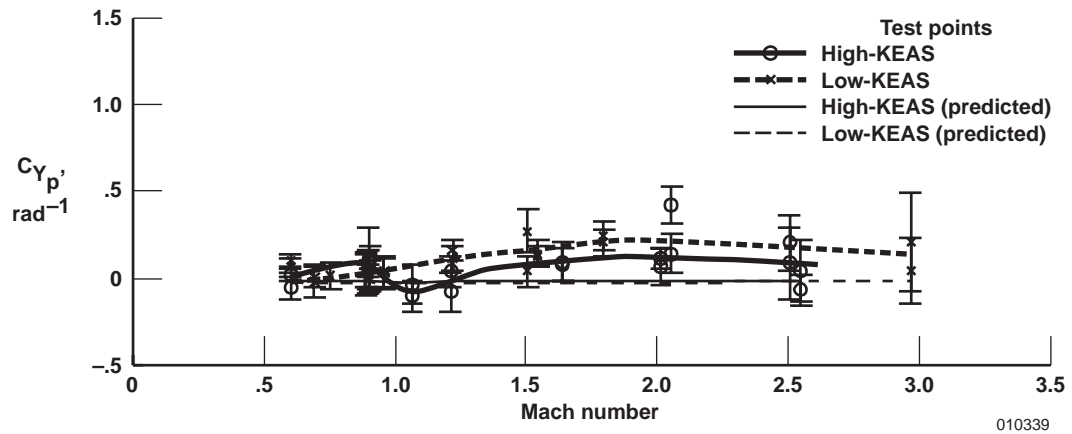
(a) C_{Y_p}.
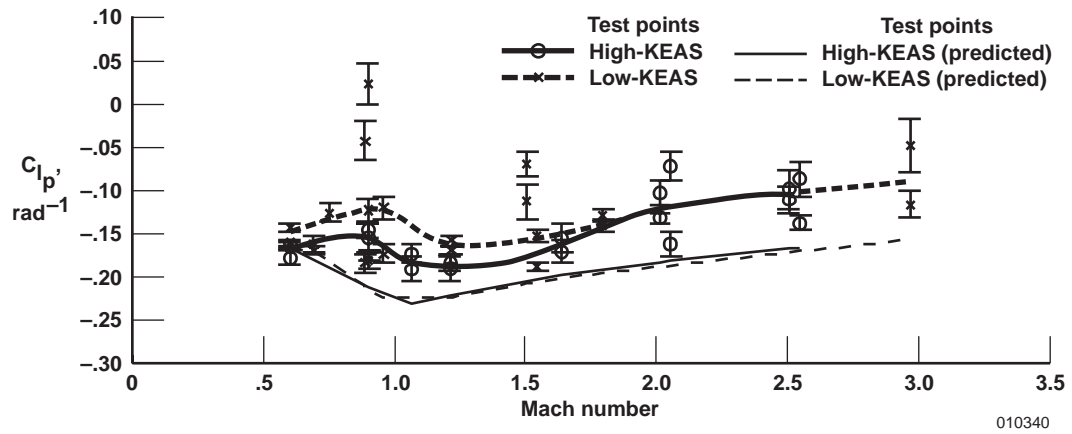
(b) C_{l_p}.
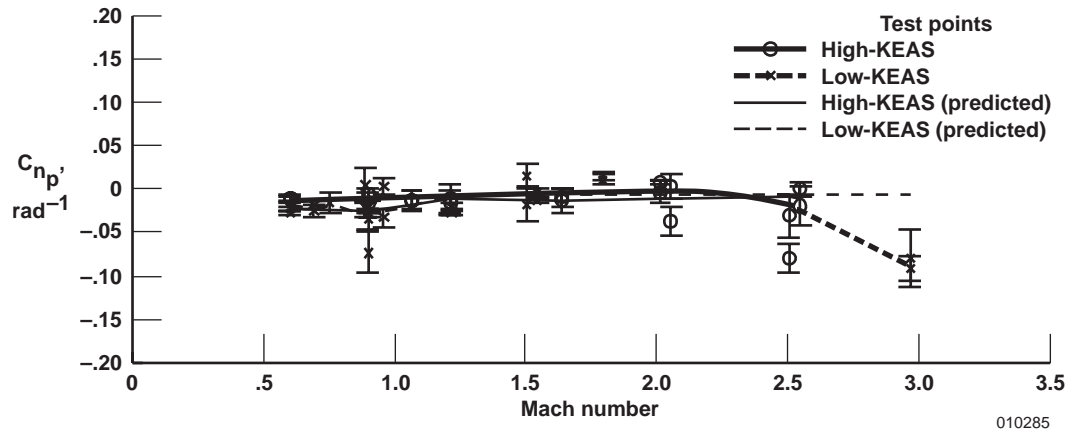
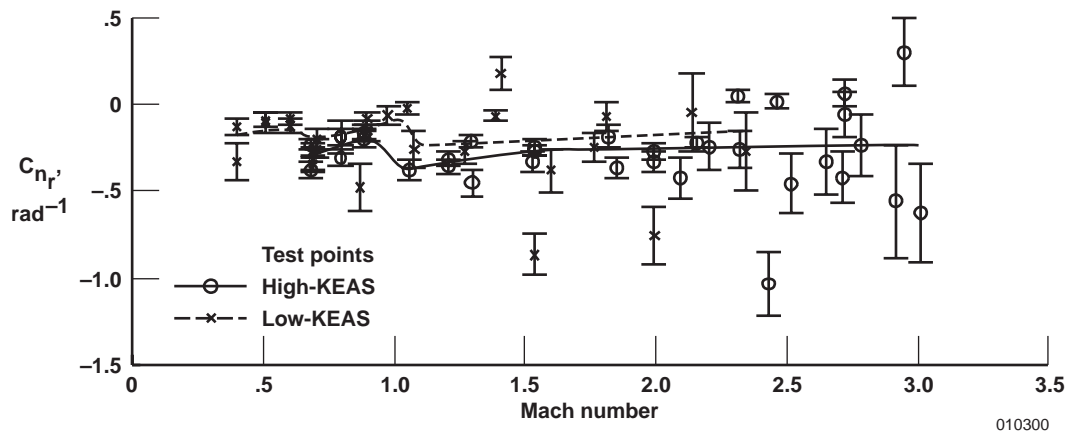(c) C_{n_p} (moment reference at 0.25 c).

Figure 37. Predicted and flight-determined roll-rate derivatives (baseline configuration).
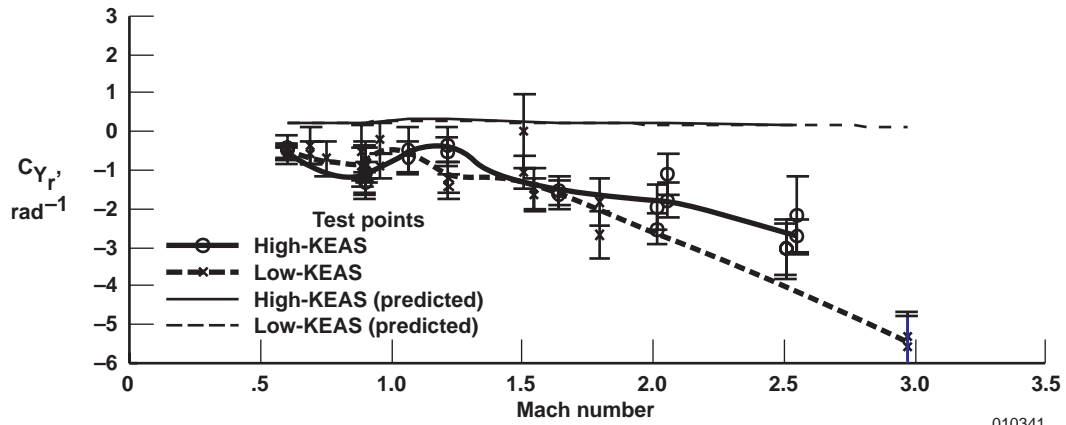
(a) C_{Y_r}.
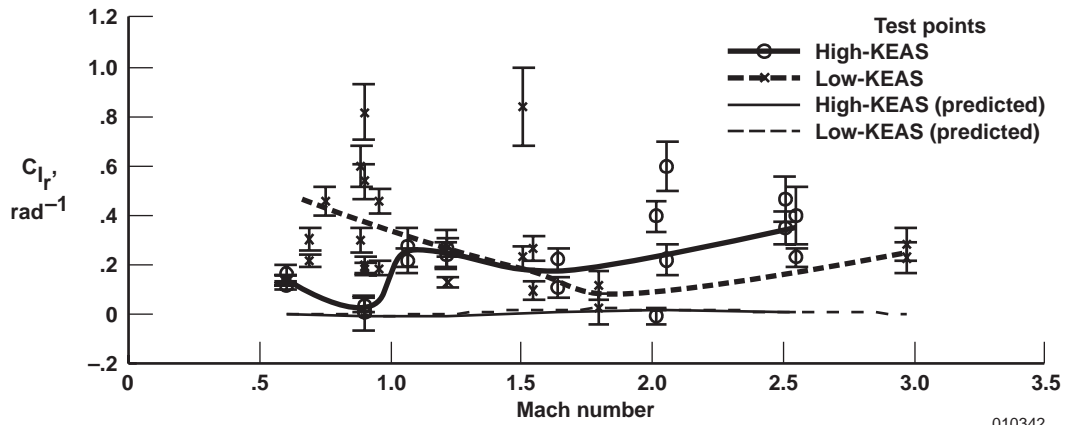
(b) C_{l_r}.
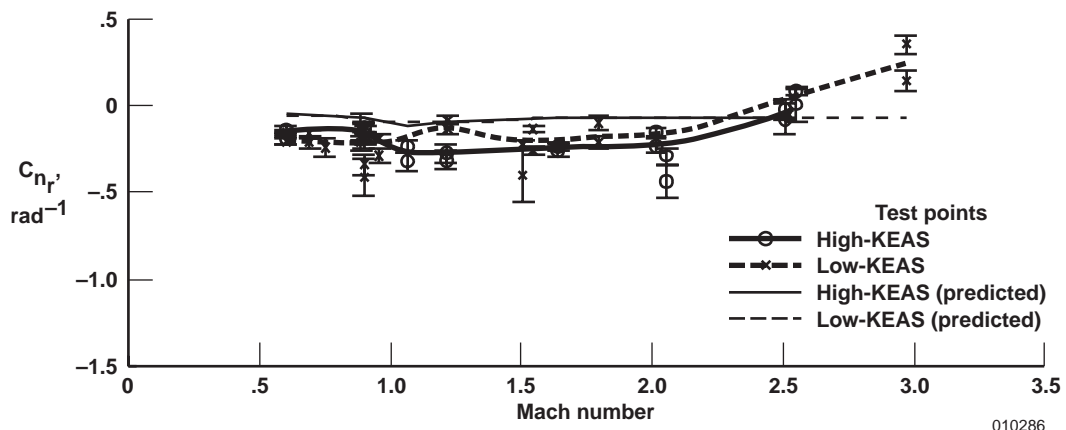
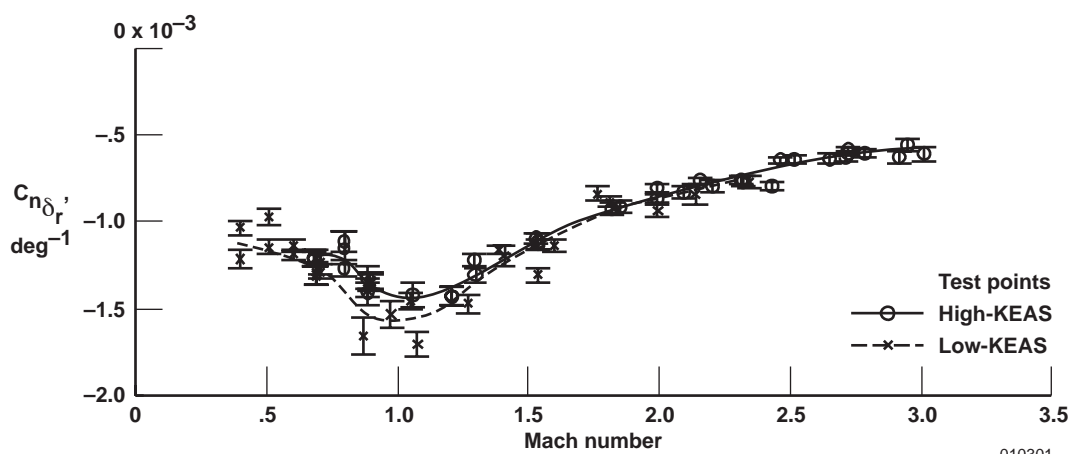(c) C_{n_r} (moment reference at 0.25 c).

Figure 38. Predicted and flight-determined yaw-rate derivatives (baseline configuration).

(a) $C_{Y_{\delta_r}}$.

(b) $C_{l_{\delta_r}}$.

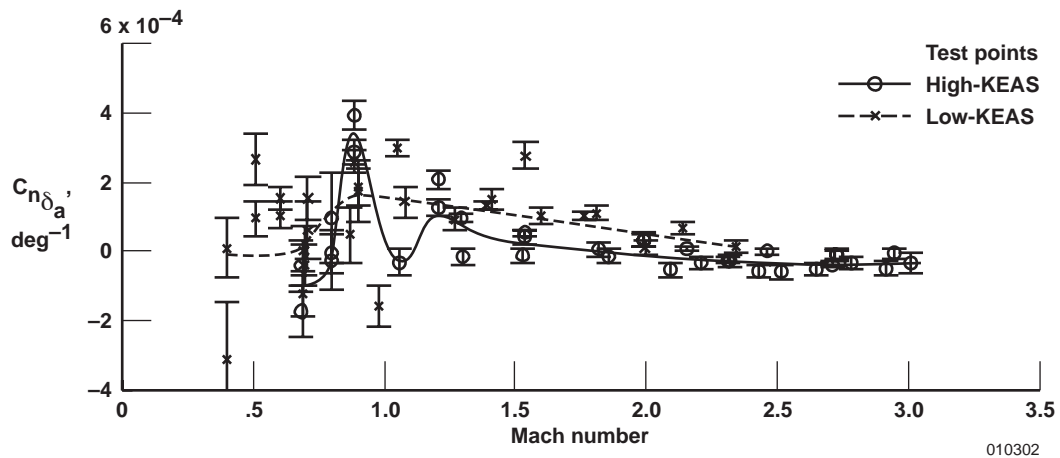(c) $C_{n_{\delta_r}}$ (moment reference at 0.25 c).
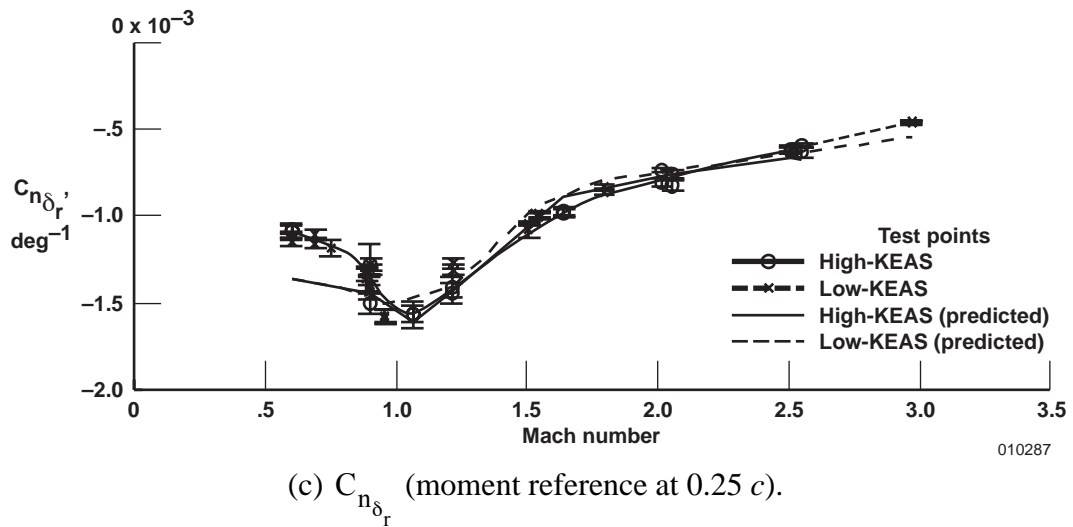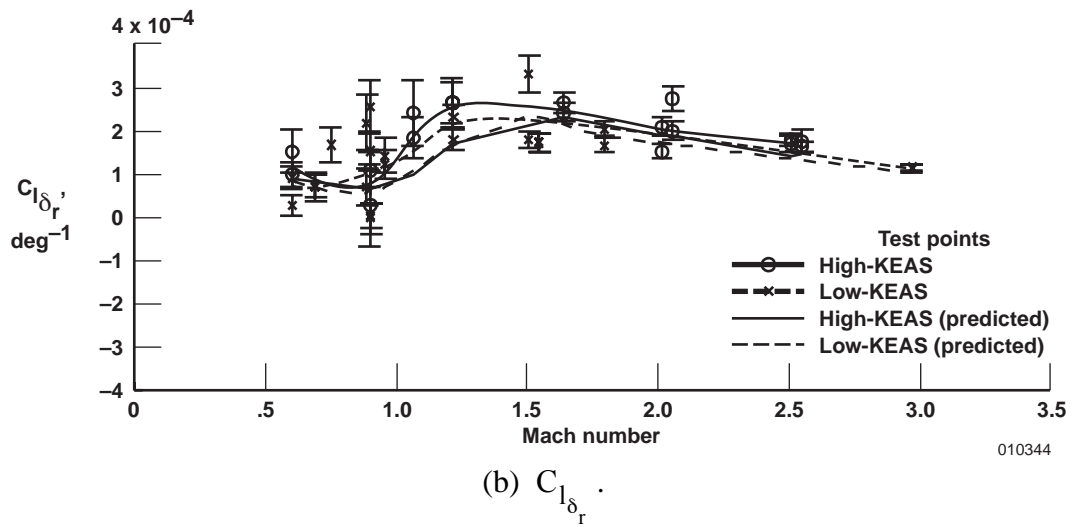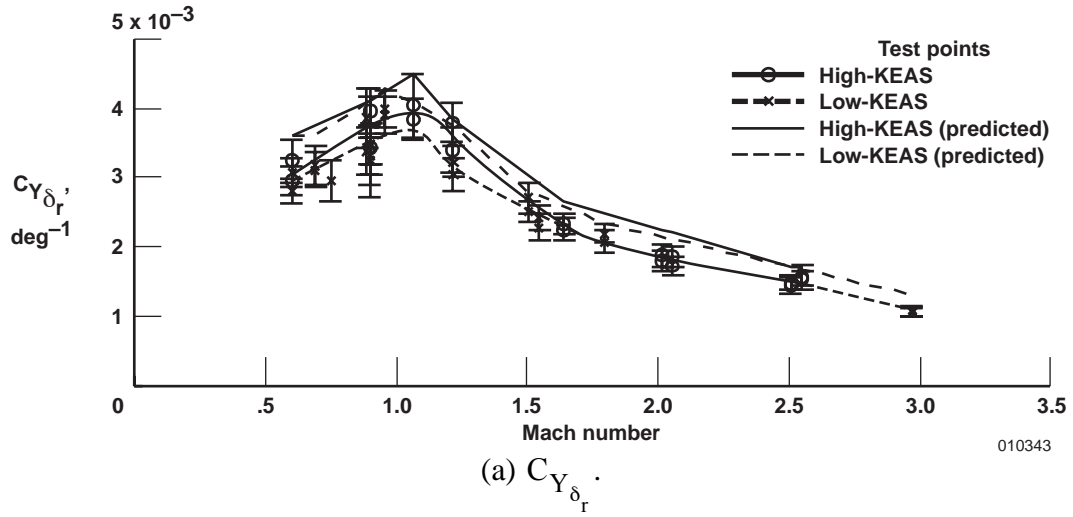
Figure 39. Predicted and flight-determined rudder derivatives (baseline configuration).
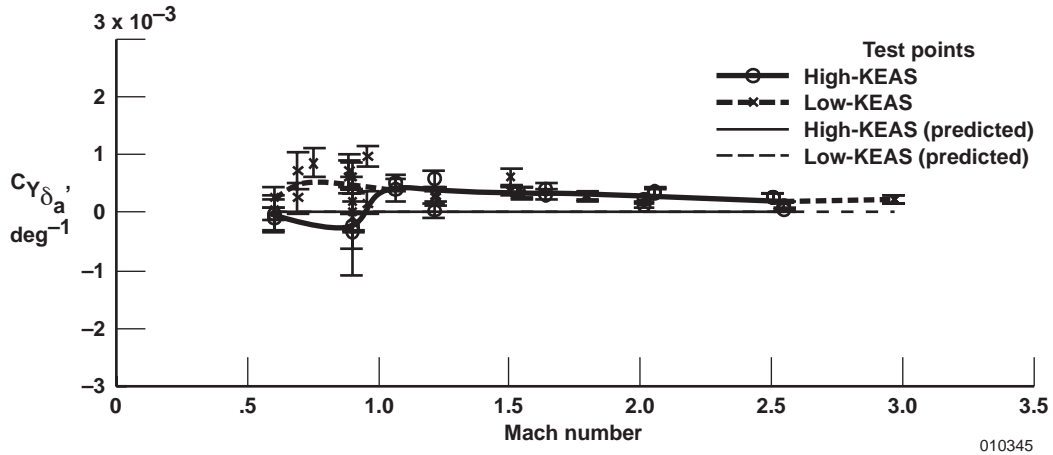
(a) $C_{Y_{\delta_a}}$.
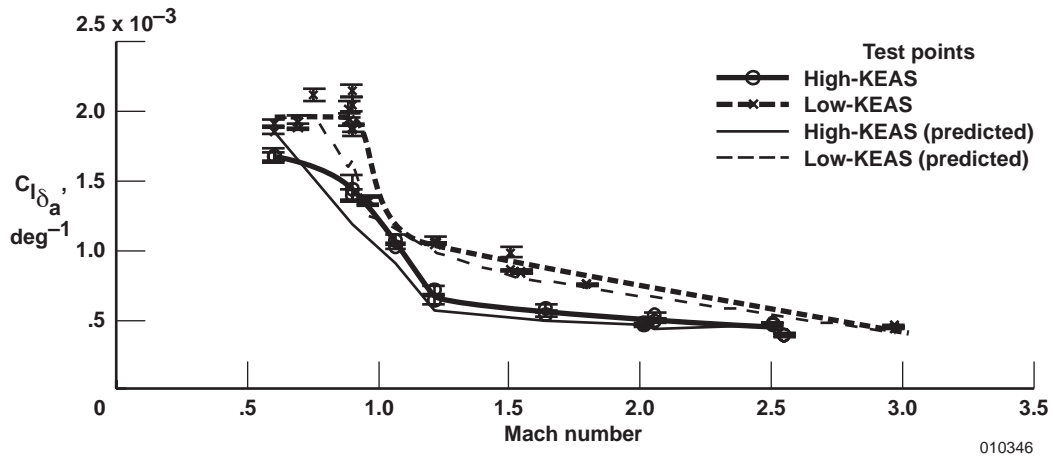
(b) $C_{l_{\delta_a}}$.
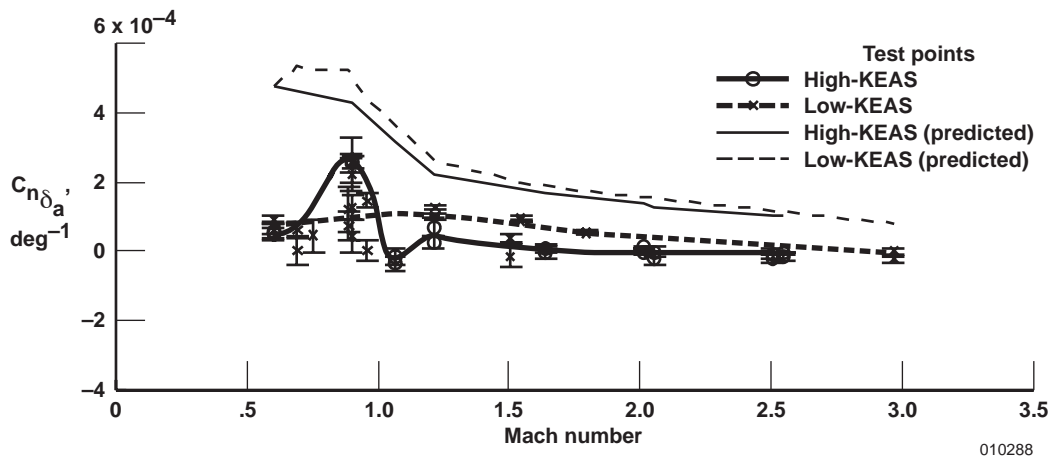
(c) $C_{n_{\delta_a}}$ (moment reference at 0.25 c).

Figure 40. Predicted and flight-determined aileron derivatives (baseline configuration).
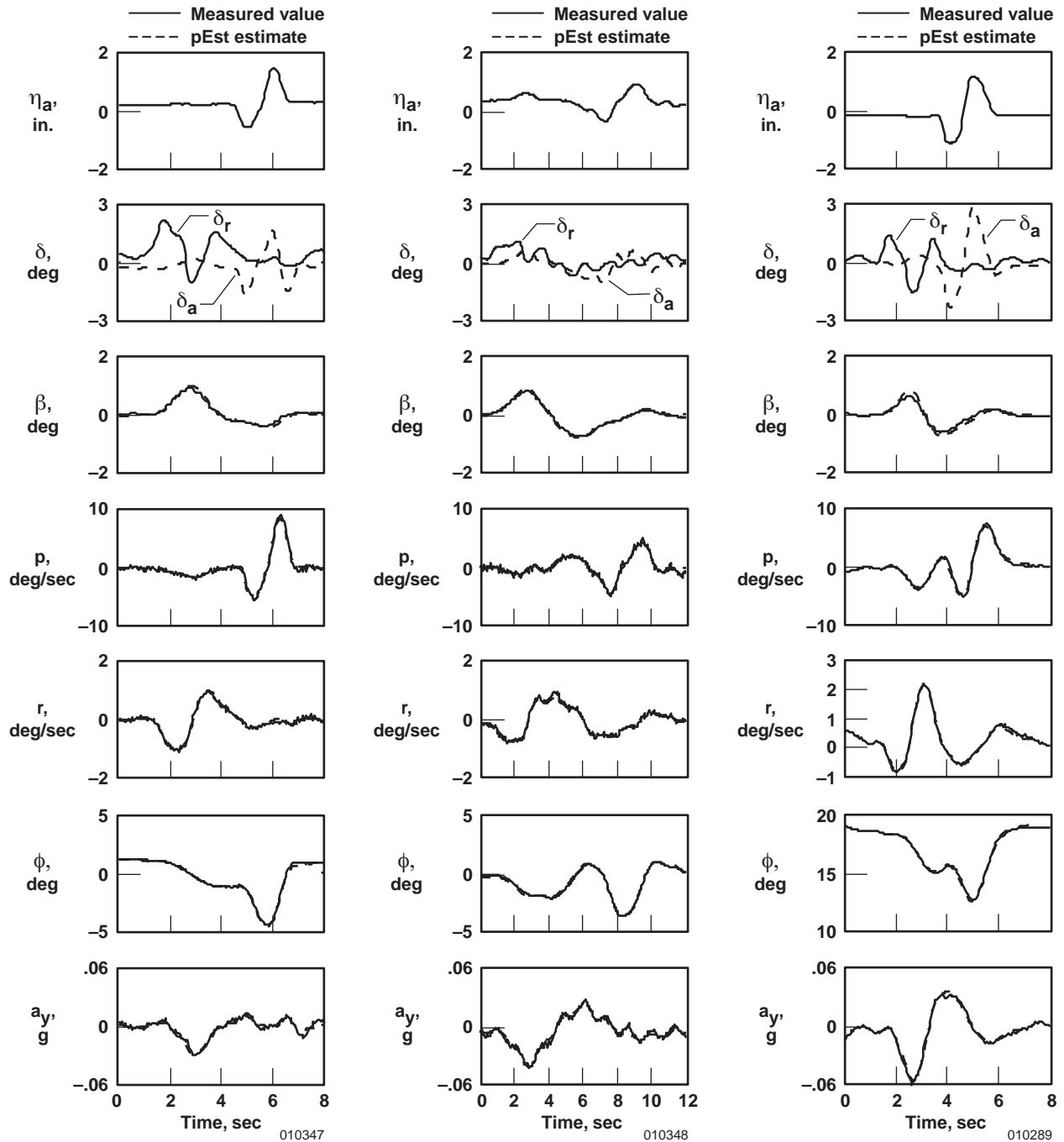
(a) Mach 0.60 and an altitude of 15,100 ft.

(b) Mach 0.95 and an altitude of 27,500 ft.

(c) Mach 1.74 and an altitude of 44,000 ft.

Figure 41. LASRE configuration lateral-directional maneuver time histories.
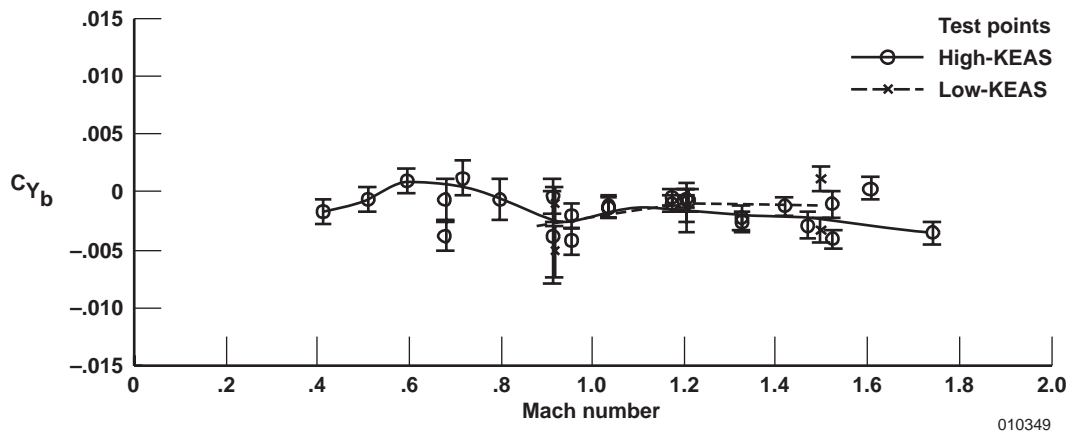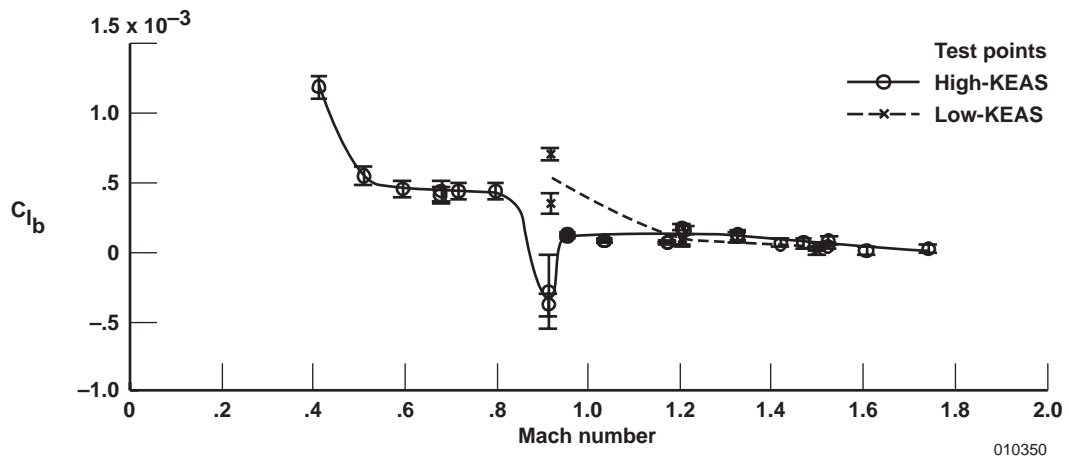
(a) C_{Y_b}.

(b) C_{l_b}.
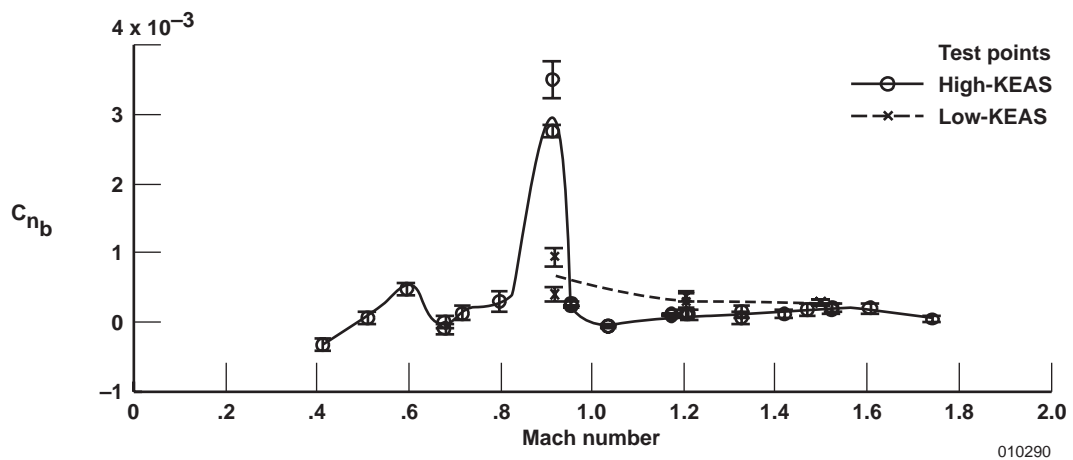
(c) C_{n_b}.

Figure 42. Flight-determined lateral-directional coefficient biases (LASRE configuration).

(a) C_{Y_β}.

010351

(b) C_{l_β}.

010352

(c) C_{n_β} (moment reference at 0.25 c).

010291
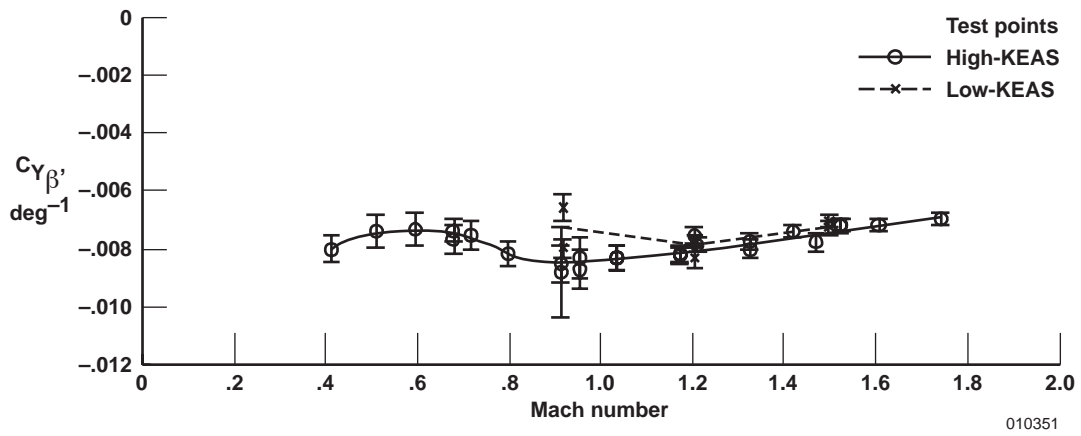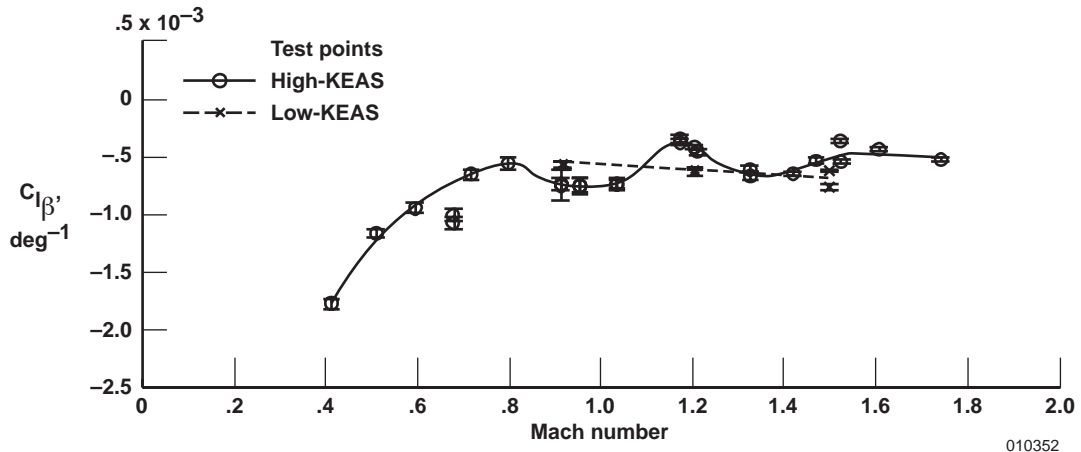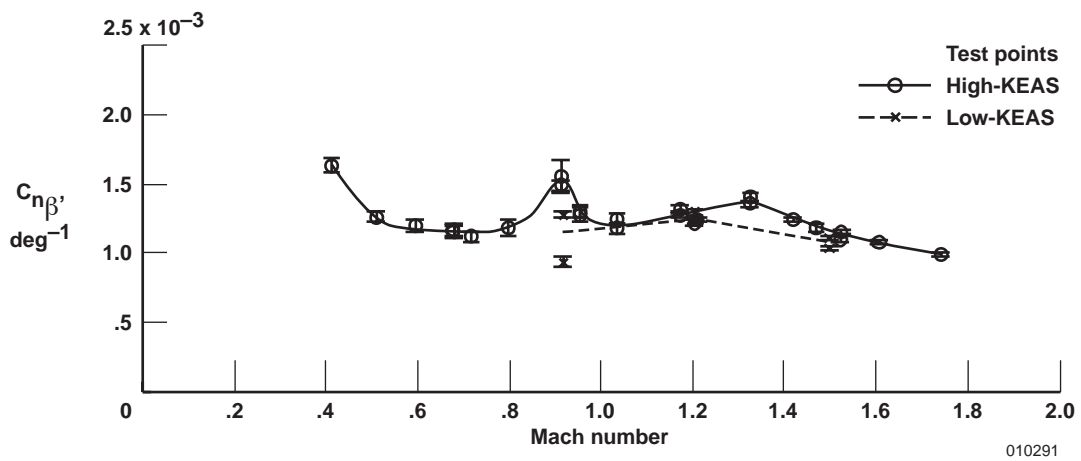
Figure 43. Flight-determined angle-of-sideslip derivatives (LASRE configuration).

69
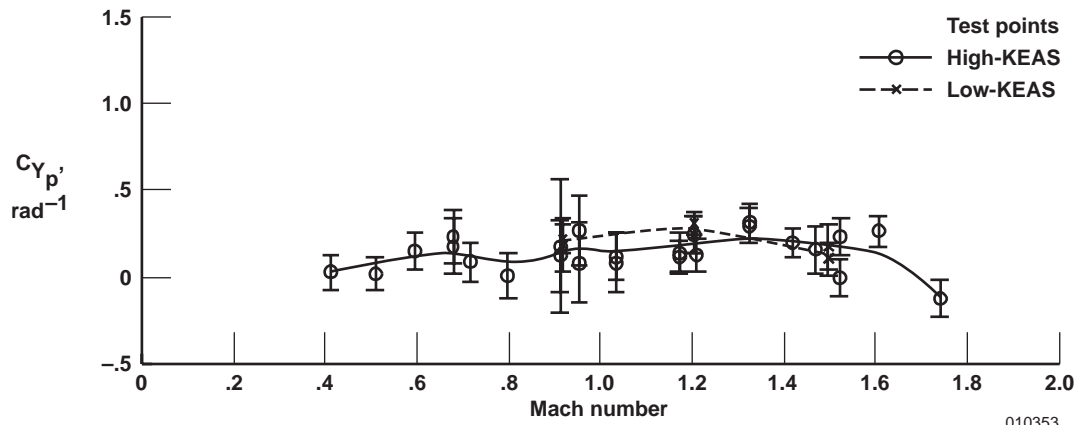
(a) C_{Y_p}.
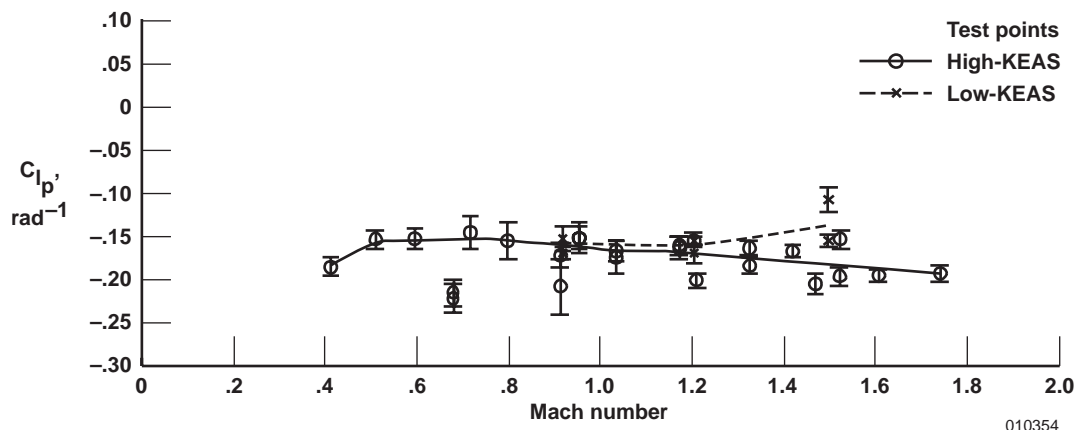
(b) C_{l_p}.
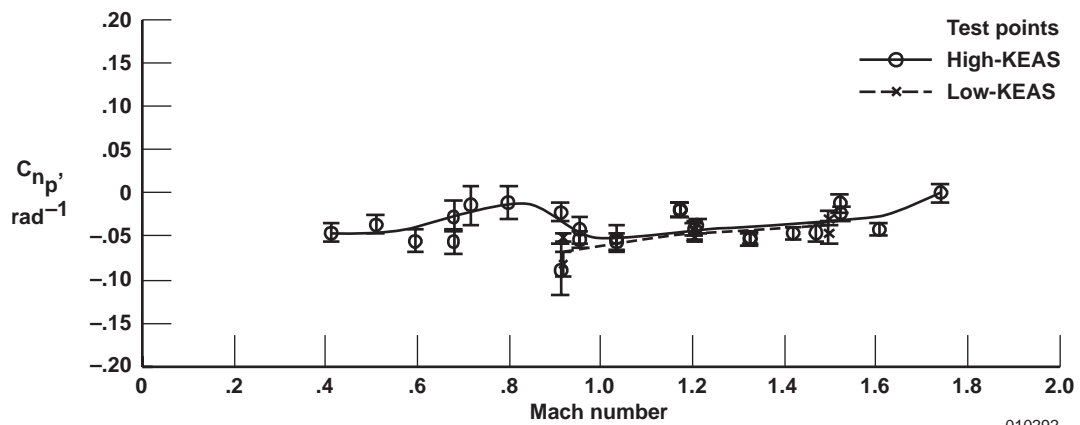
(c) C_{n_p} (moment reference at 0.25 c).

Figure 44. Flight-determined roll-rate derivatives (LASRE configuration).
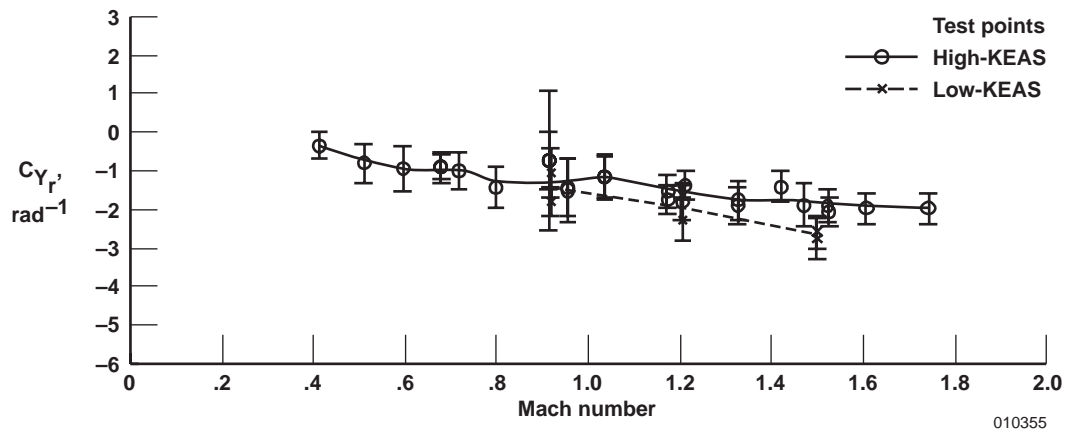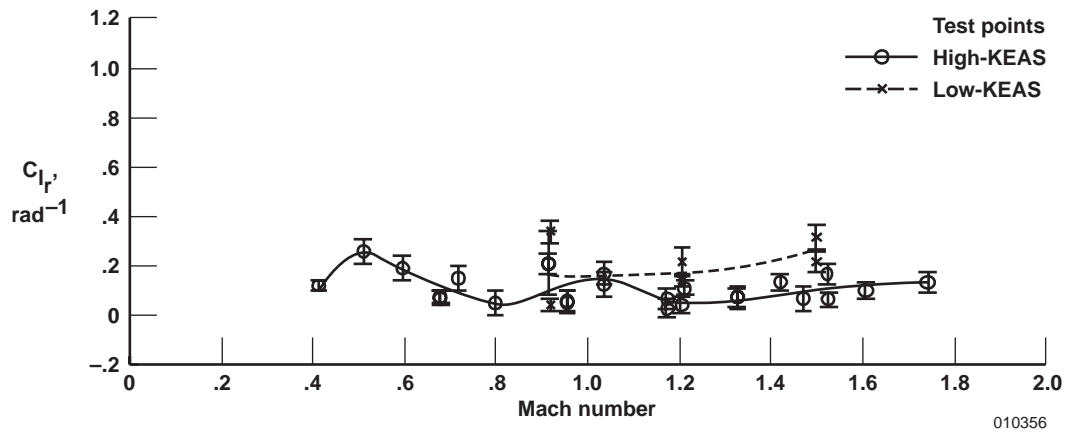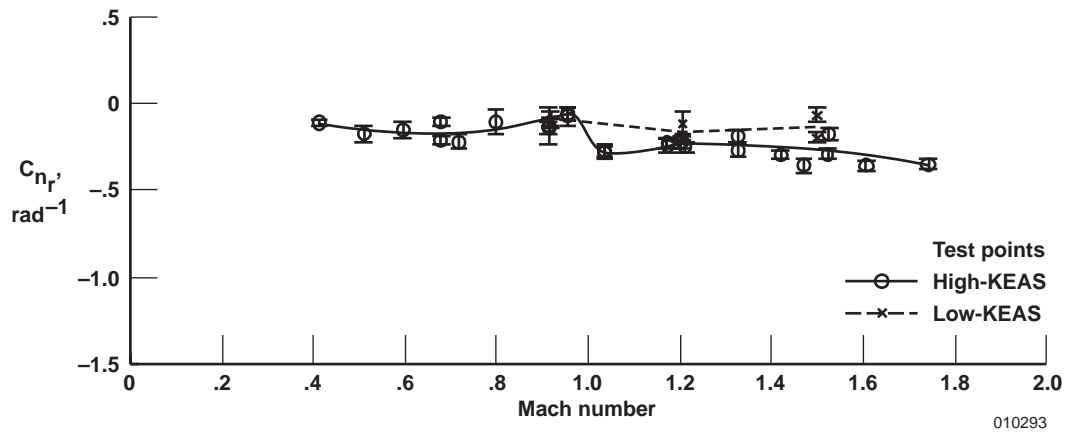
(a) C_{Y_r}.

(b) C_{l_r}.

(c) C_{n_r} (moment reference at 0.25 c).

Figure 45. Flight-determined yaw-rate derivatives (LASRE configuration).

71
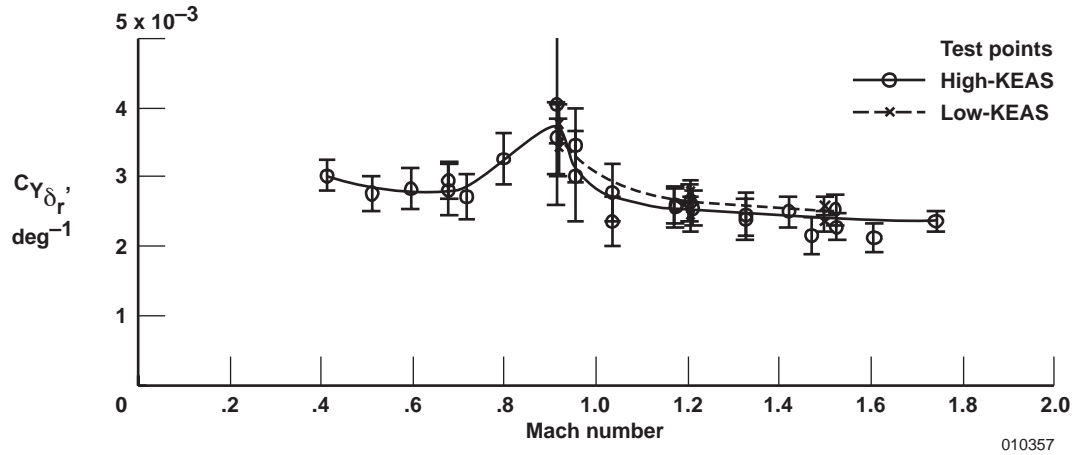
(a) $C_{Y_{\delta_r}}$.
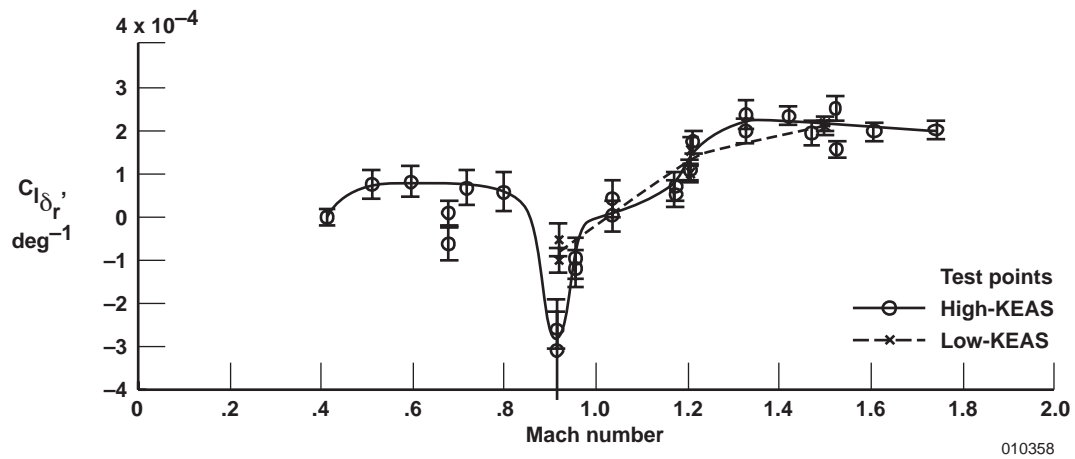
(b) $C_{l_{\delta_r}}$.
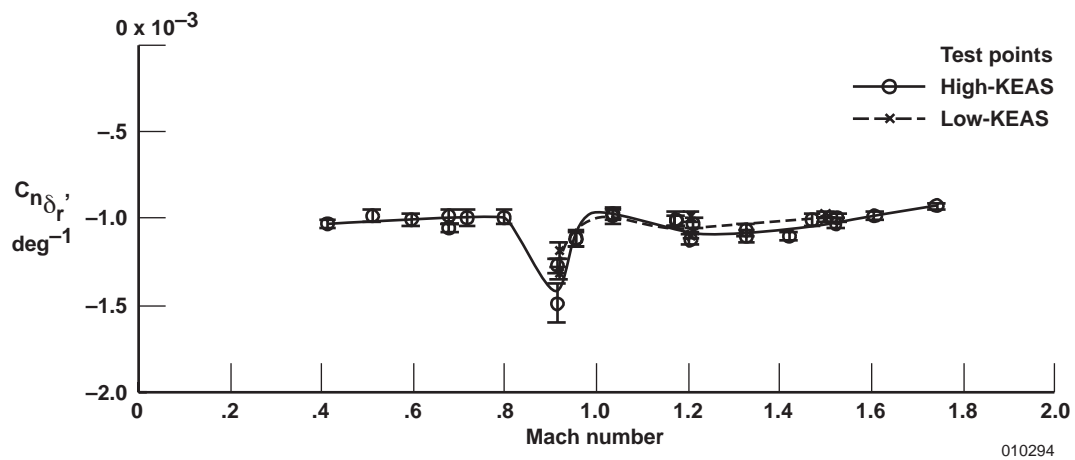
(c) $C_{n_{\delta_r}}$ (moment reference at 0.25 c).

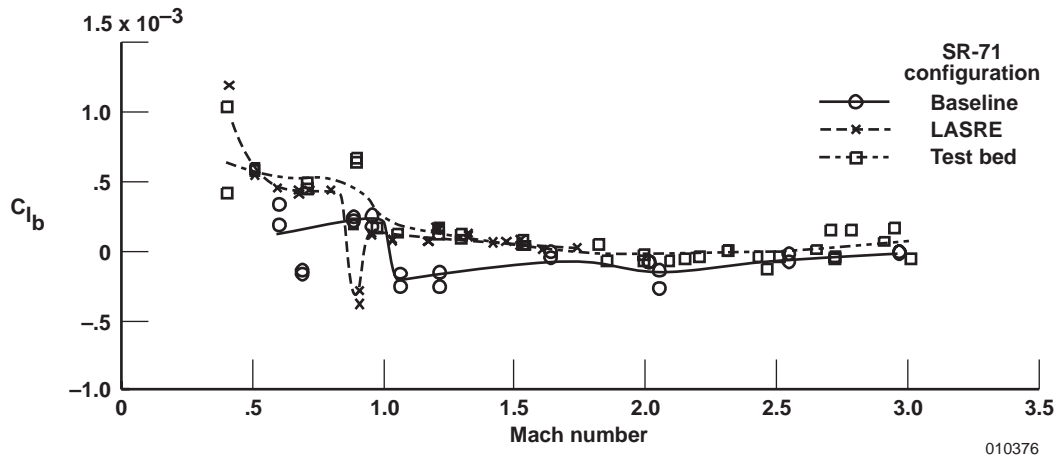Figure 46. Flight-determined rudder derivatives (LASRE configuration).
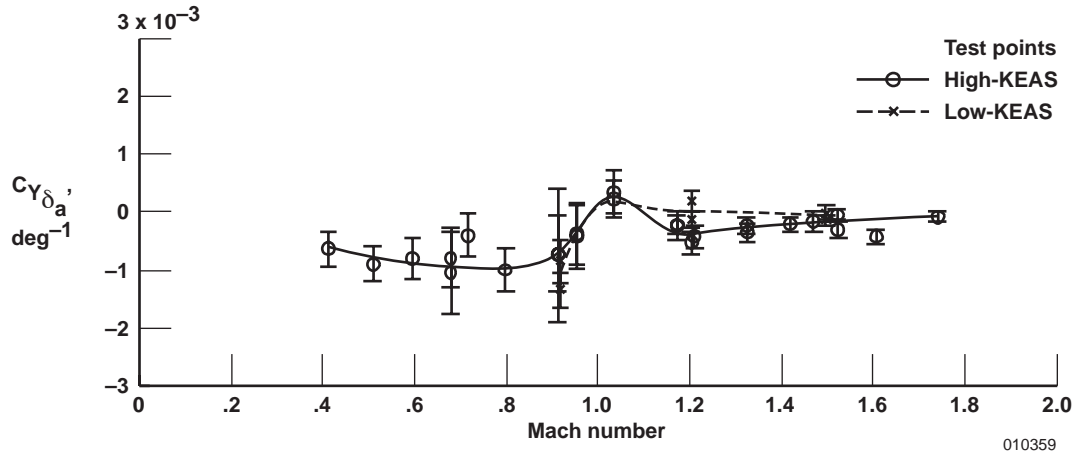
(a) $C_{Y_{\delta_a}}$.

(b) $C_{l_{\delta_a}}$.
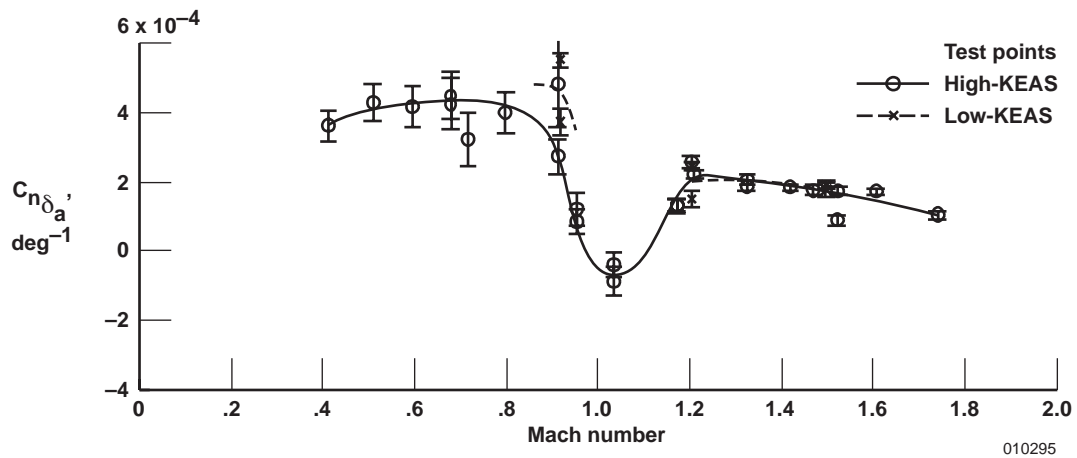
(c) $C_{n_{\delta_a}}$ (moment reference at 0.25 c).

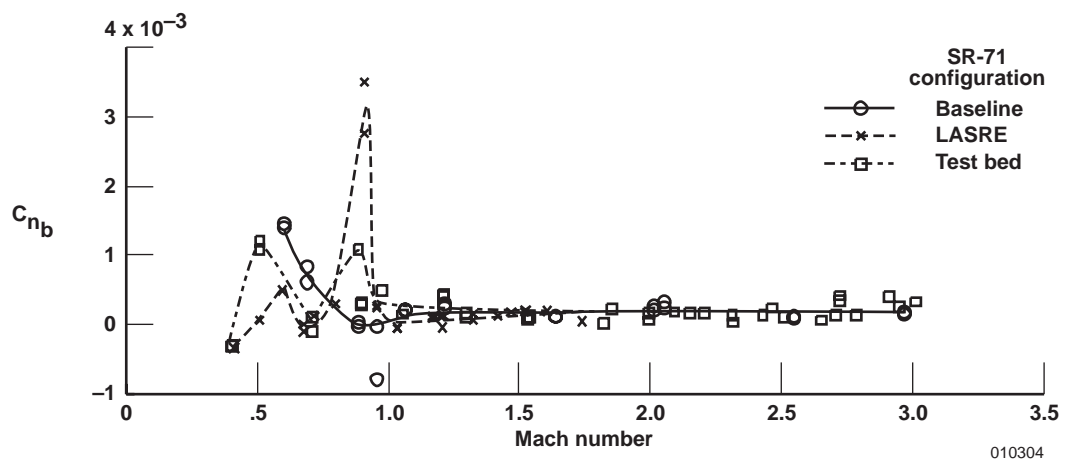Figure 47. Flight-determined aileron derivatives (LASRE configuration).

73
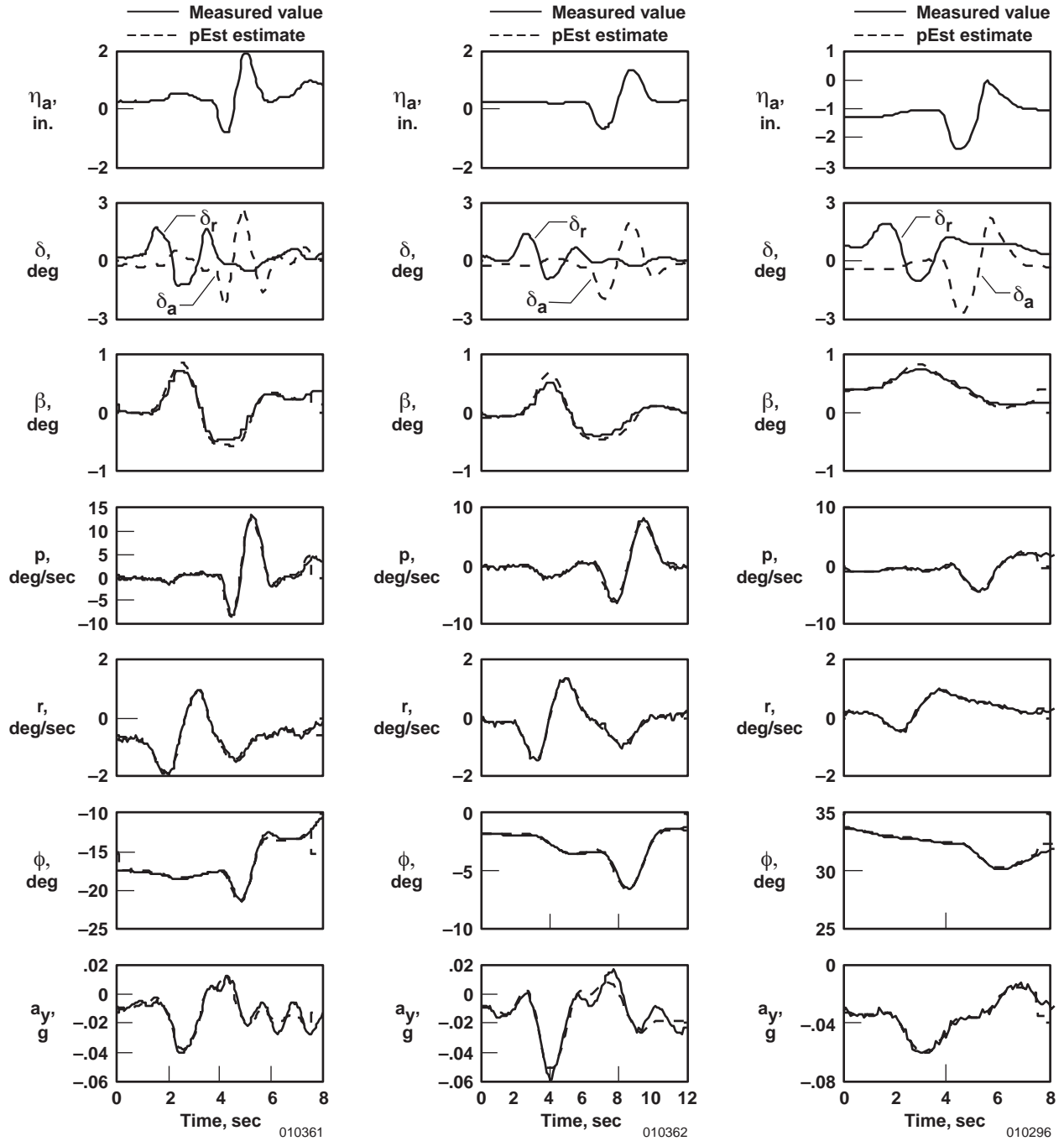
(a) Mach 0.71 and an altitude of 20,000 ft.

(b) Mach 1.06 and an altitude of 25,500 ft.

(c) Mach 3.01 and an altitude of 68,300 ft.

Figure 48. Test bed configuration lateral-directional maneuver time histories.
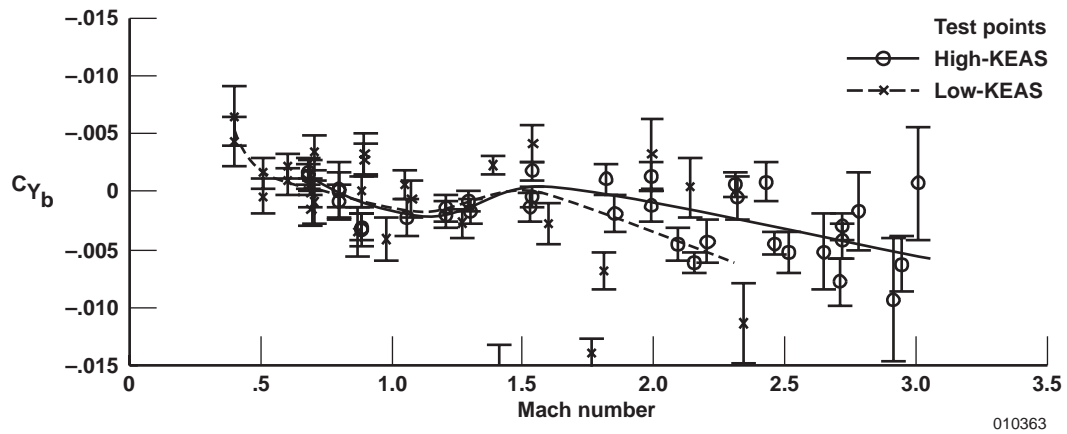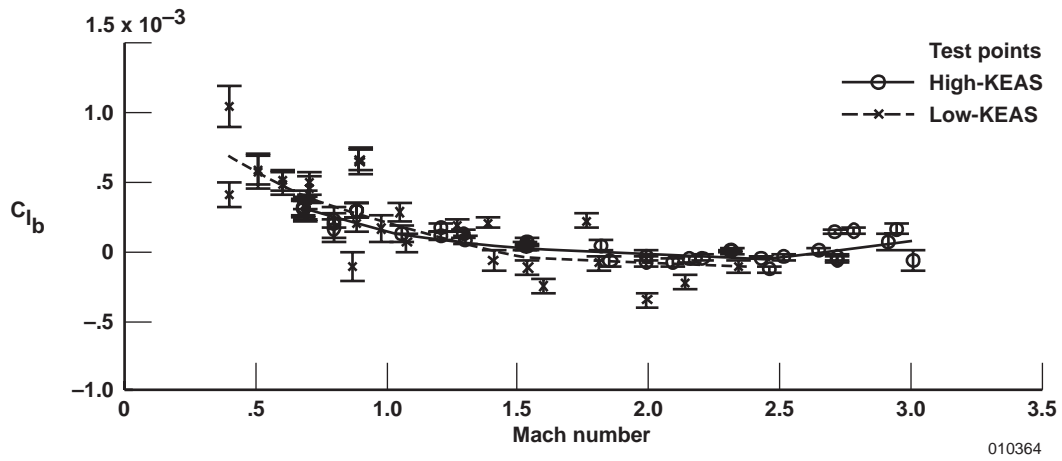
(a) C_{Y_b}.

(b) C_{l_b}.
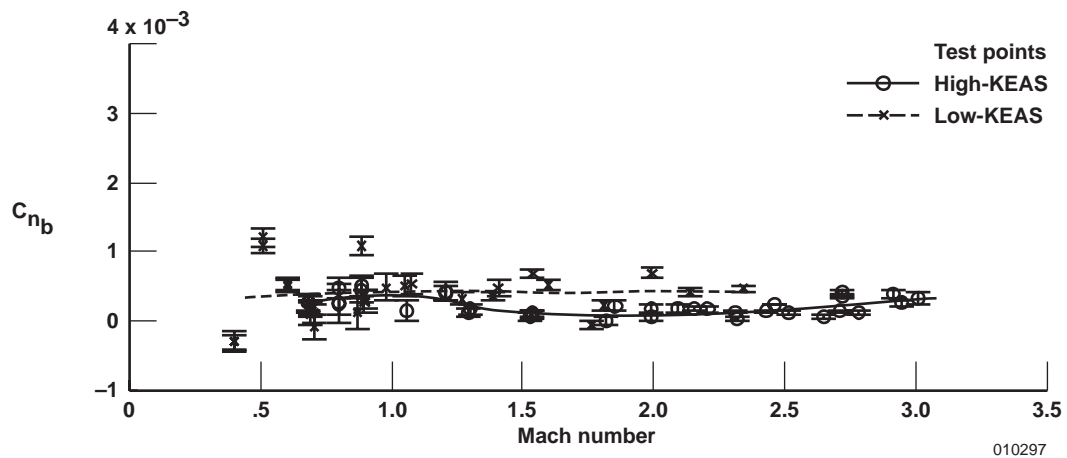
(c) C_{n_b}.

Figure 49. Flight-determined lateral-directional coefficient biases (test bed configuration).

(a) C_{Y_β}.

(b) C_{l_β}.
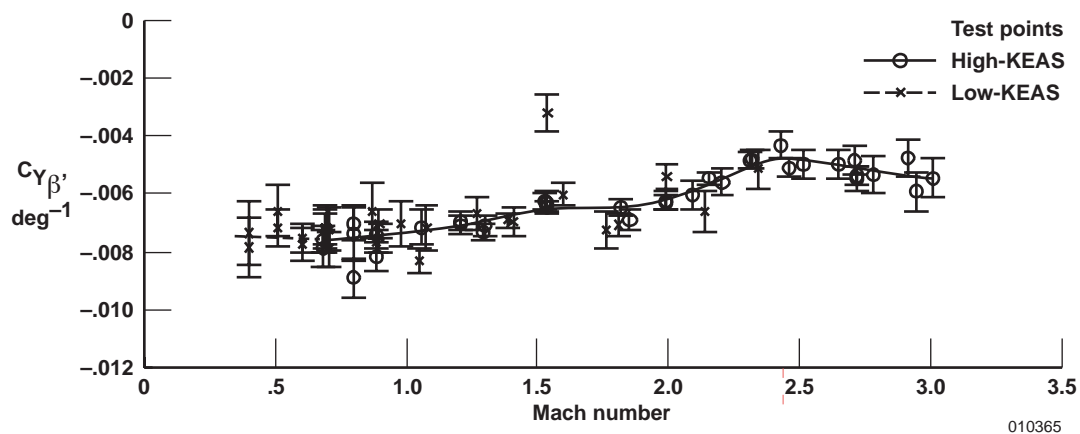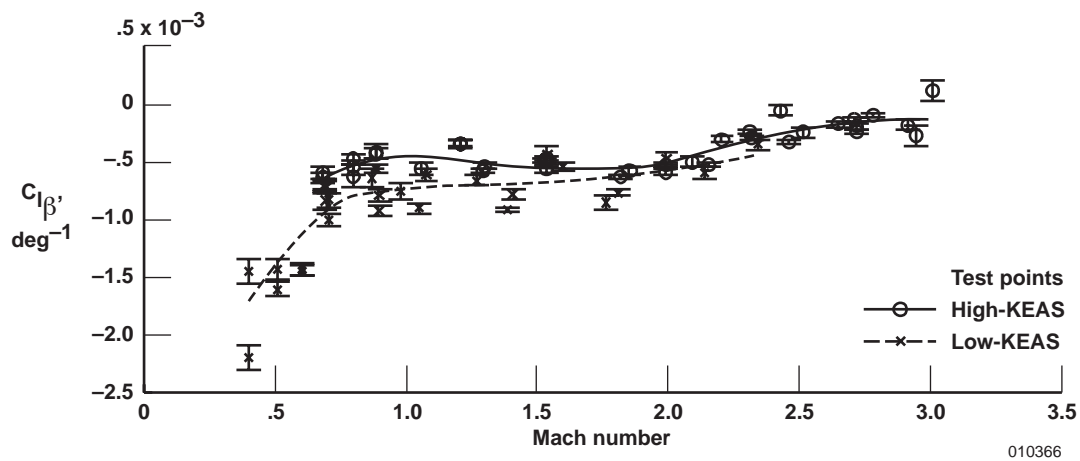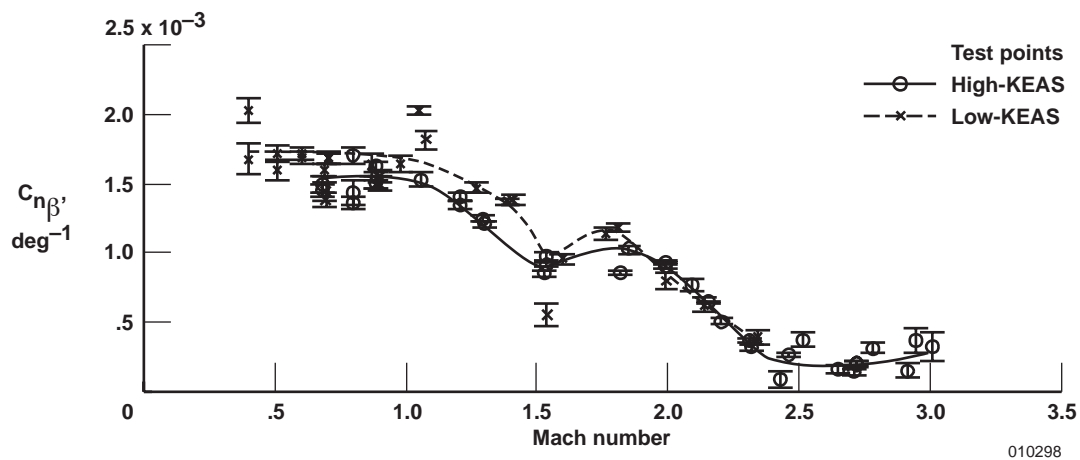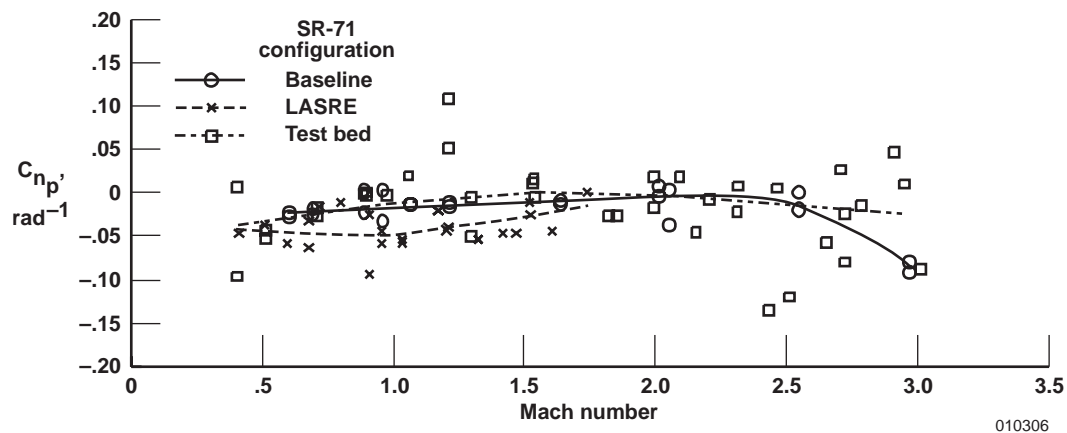

(c) C_{n_β} (moment reference at $0.25\,c$).

Figure 50. Flight-determined angle-of-sideslip derivatives (test bed configuration).
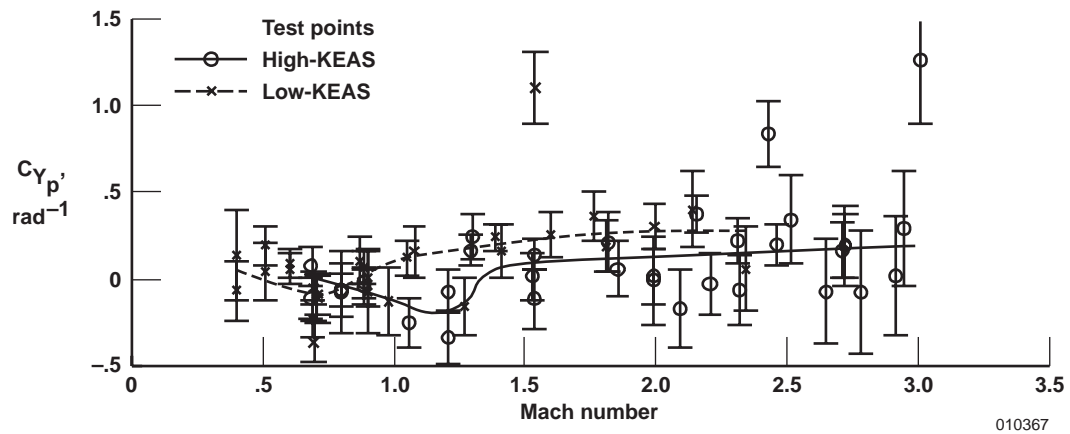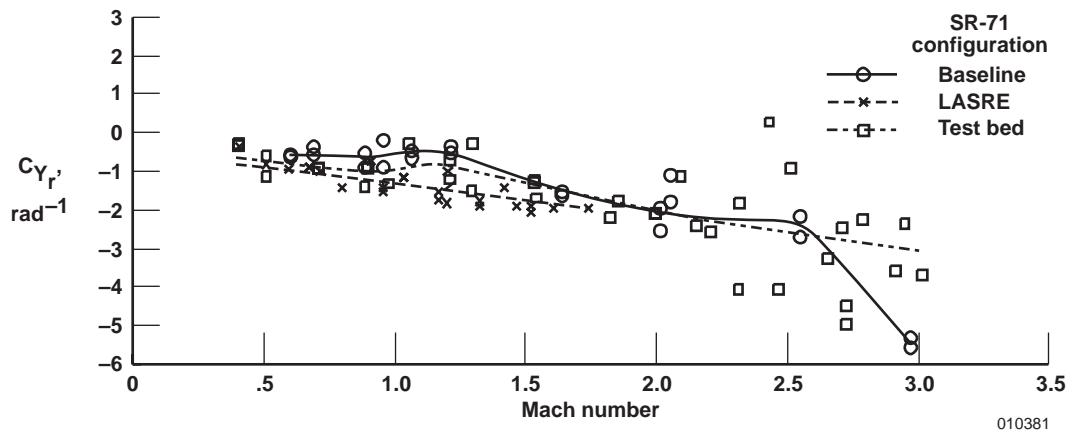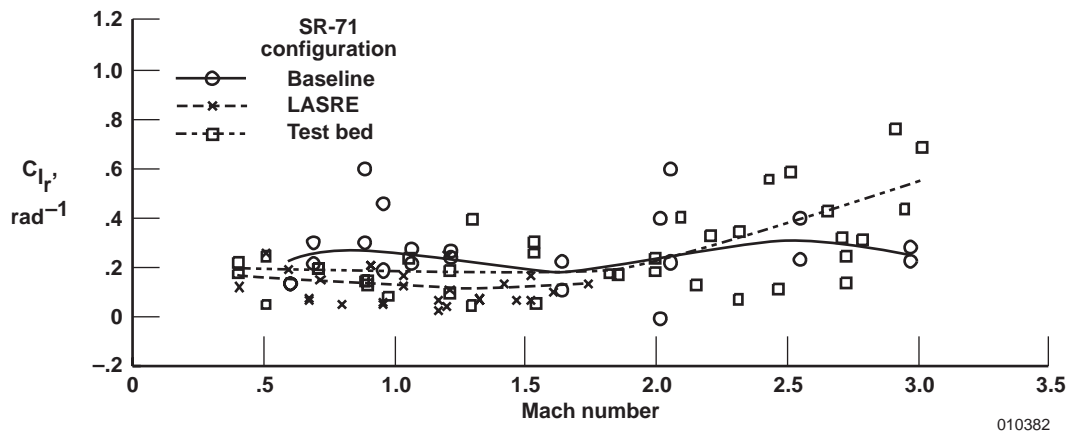
(a) C_{Y_p}.
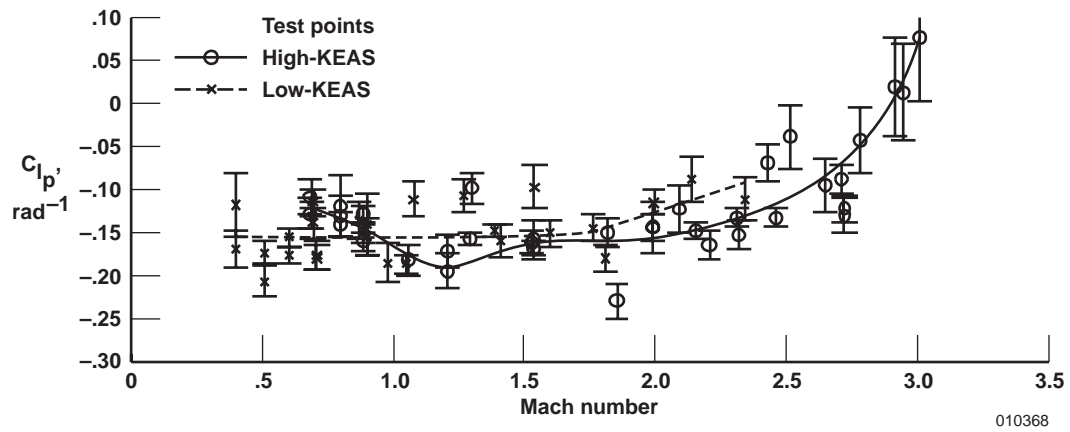
(b) C_{l_p}.
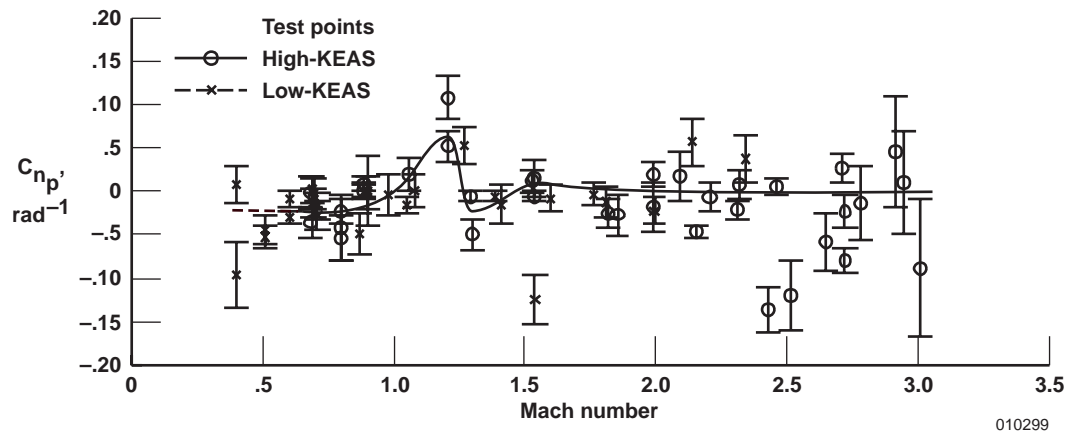
(c) C_{n_p} (moment reference at 0.25 c).

Figure 51. Flight-determined roll-rate derivatives (test bed configuration).
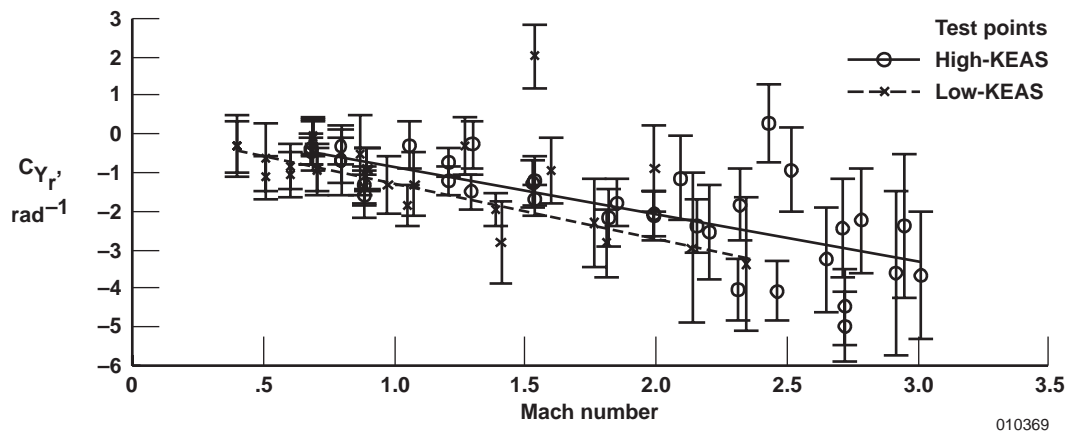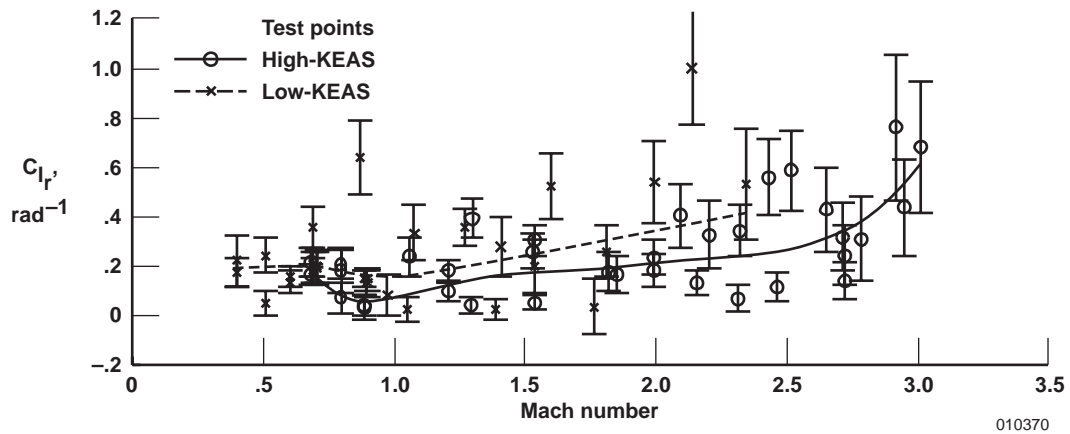
(a) C_{Y_r}.

(b) C_{l_r}.

(c) C_{n_r} (moment reference at 0.25 c).

Figure 52. Flight-determined yaw-rate derivatives (test bed configuration).

78
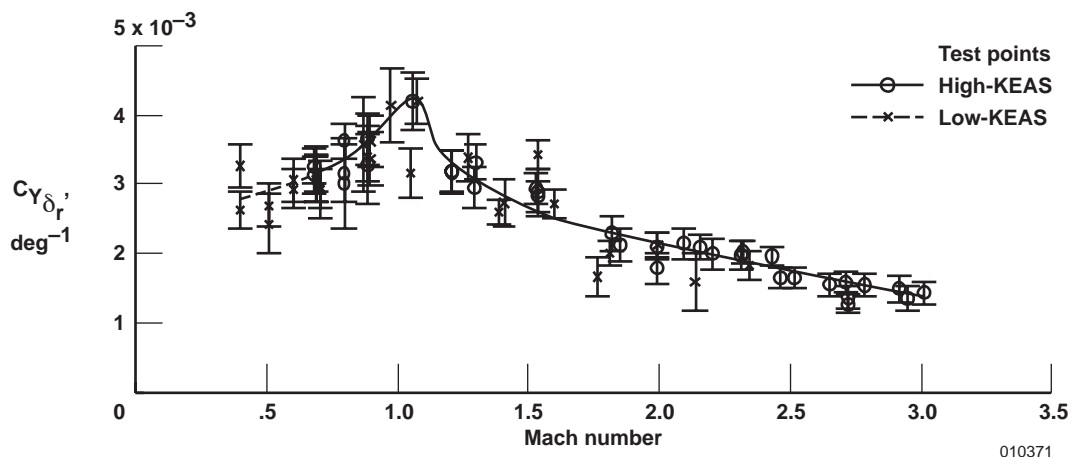
(a) $C_{Y_{\delta_r}}$.
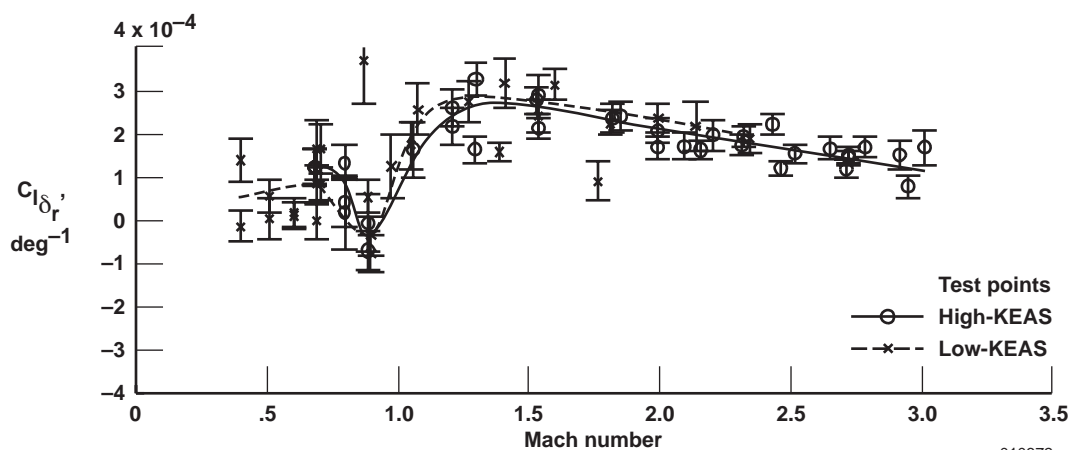
(b) $C_{l_{\delta_r}}$.

(c) $C_{n_{\delta_r}}$ (moment reference at 0.25 c).

Figure 53. Flight-determined rudder derivatives (test bed configuration).
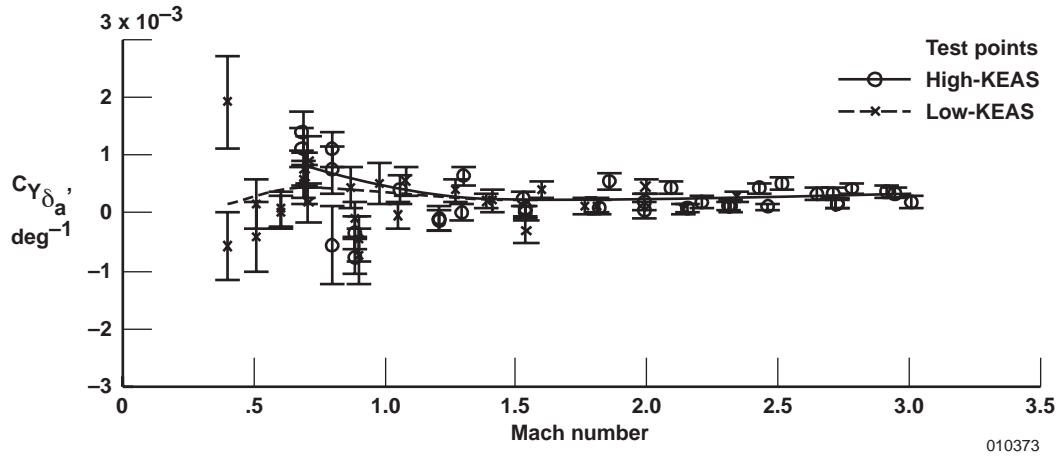
(a) $C_{Y_{\delta_a}}$.
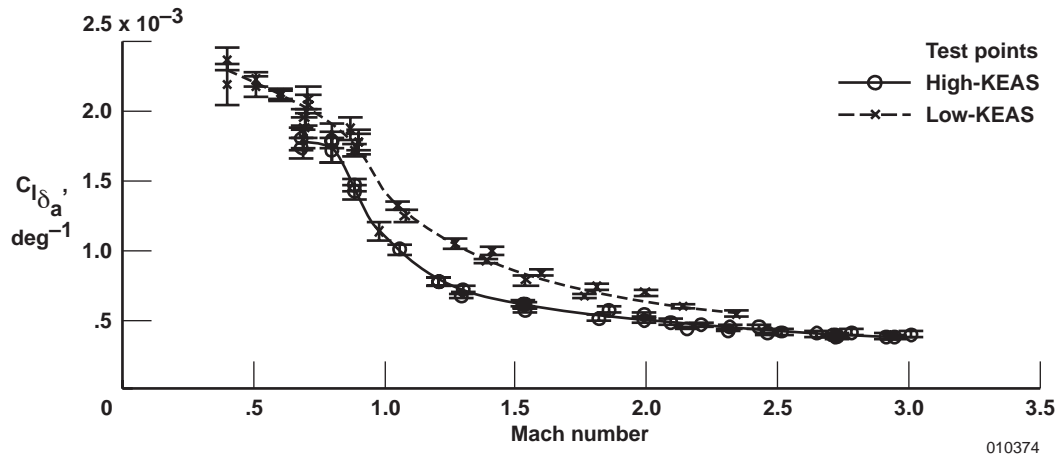
(b) $C_{l_{\delta_a}}$.

(c) $C_{n_{\delta_a}}$ (moment reference at 0.25 c).

Figure 54. Flight-determined aileron derivatives (test bed configuration).
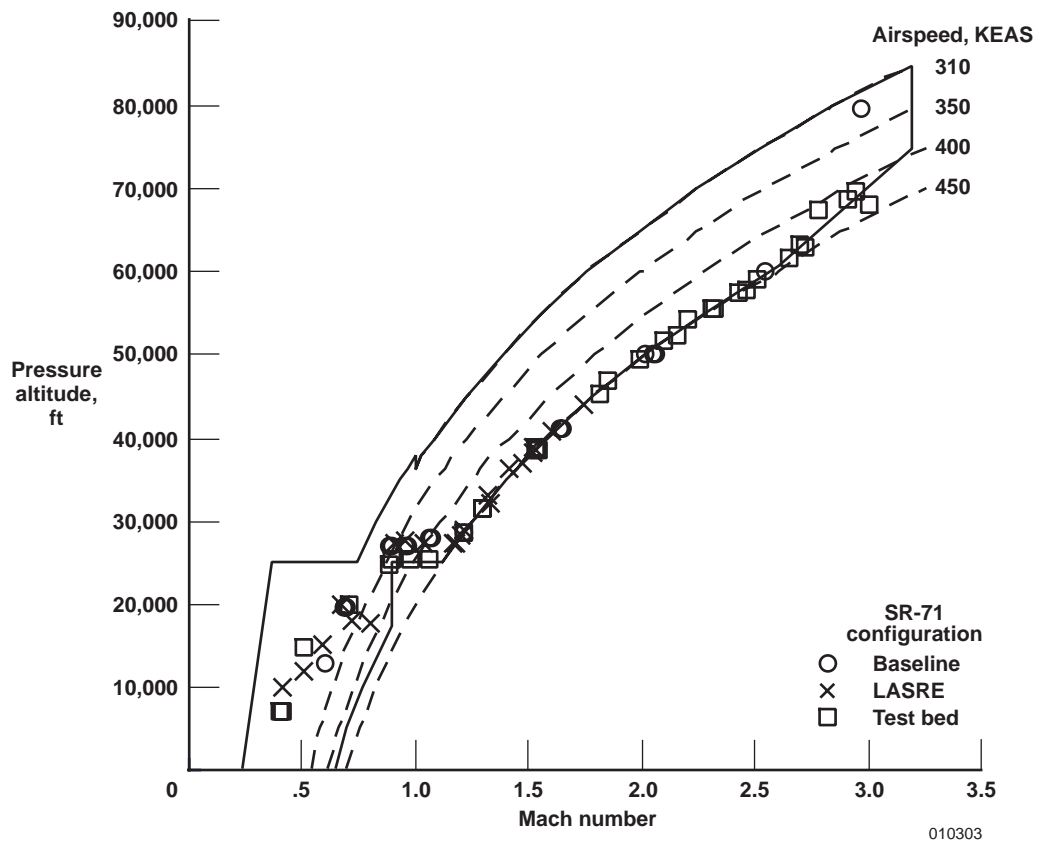
Figure 55. Flight conditions for comparison of configuration lateral-directional stability and control derivatives.

(a) C_{Y_b}.

010375

(b) C_{l_b}.

010376

(c) C_{n_b}.

010304
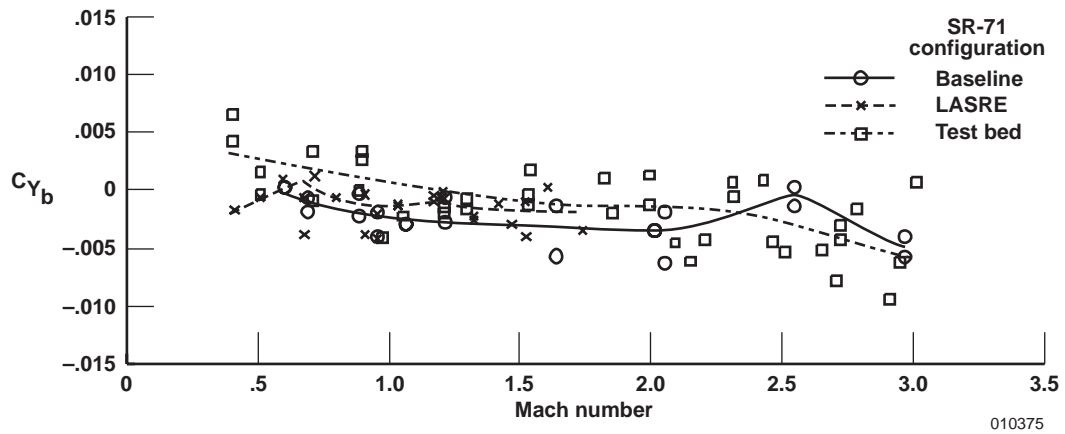
Figure 56. Flight-determined lateral-directional coefficient biases (all three configurations).

(a) C_{Y_β}.

(b) C_{l_β}.
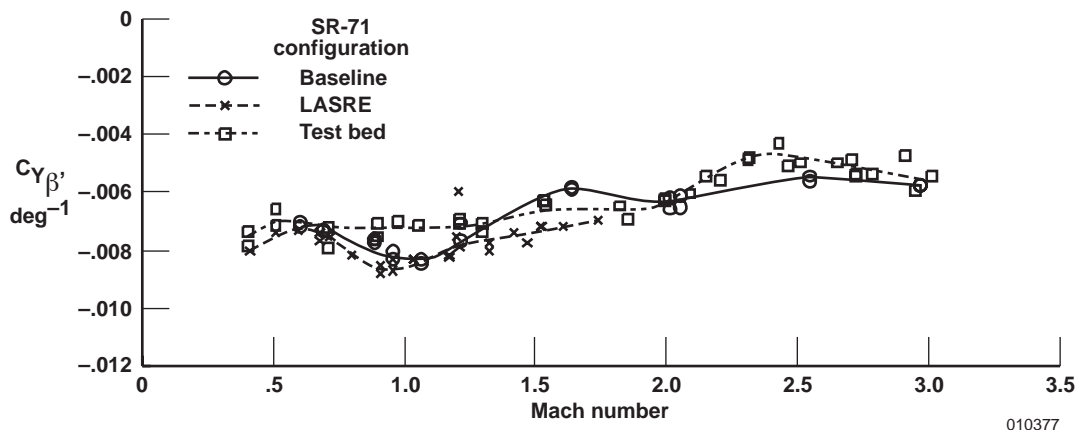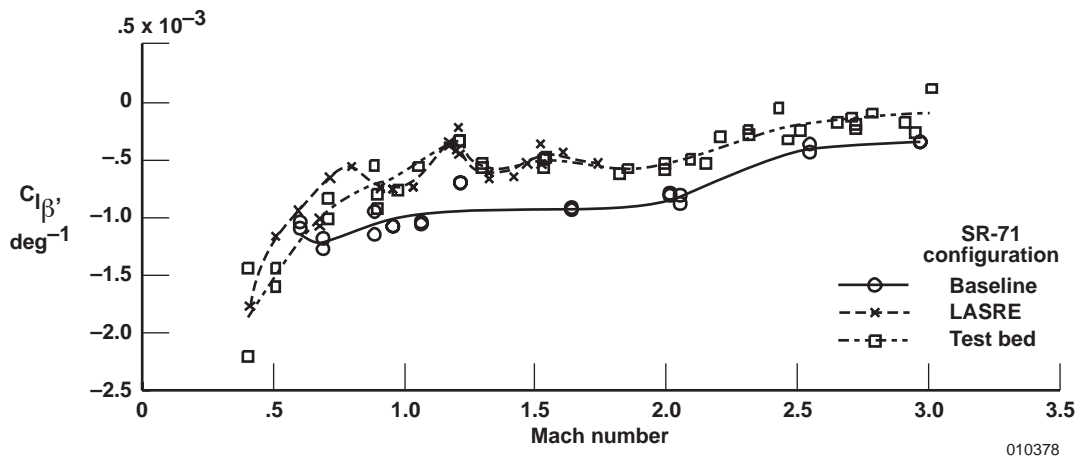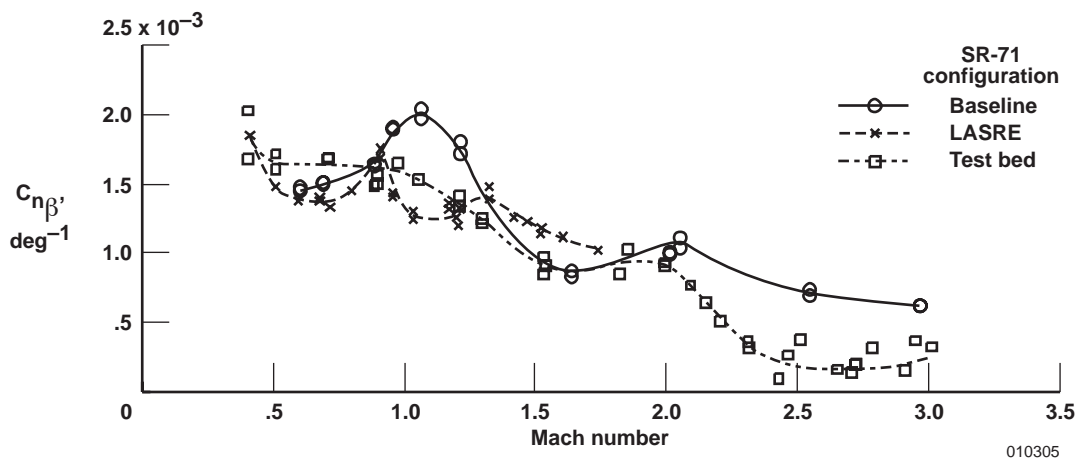
(c) C_{n_β} (moment reference at 0.25 c).

Figure 57. Flight-determined angle-of-sideslip derivatives (all three configurations).
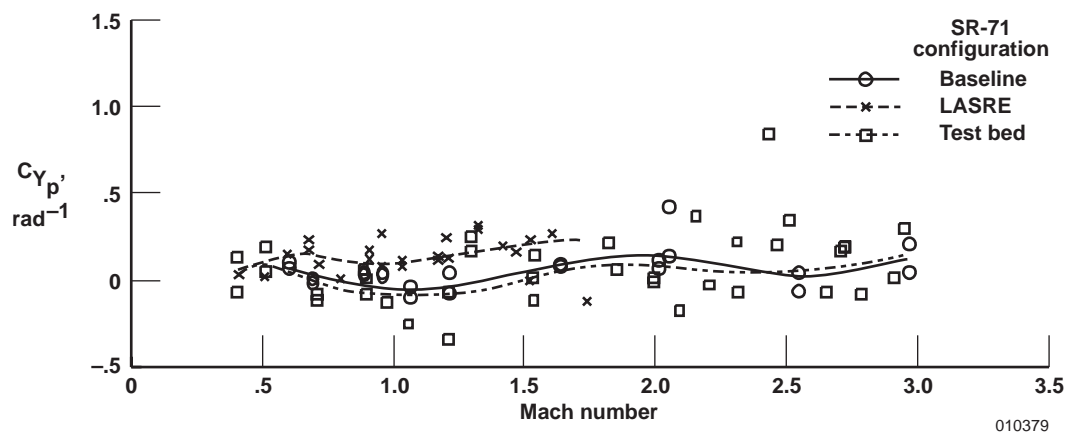
(a) C_{Y_p}.
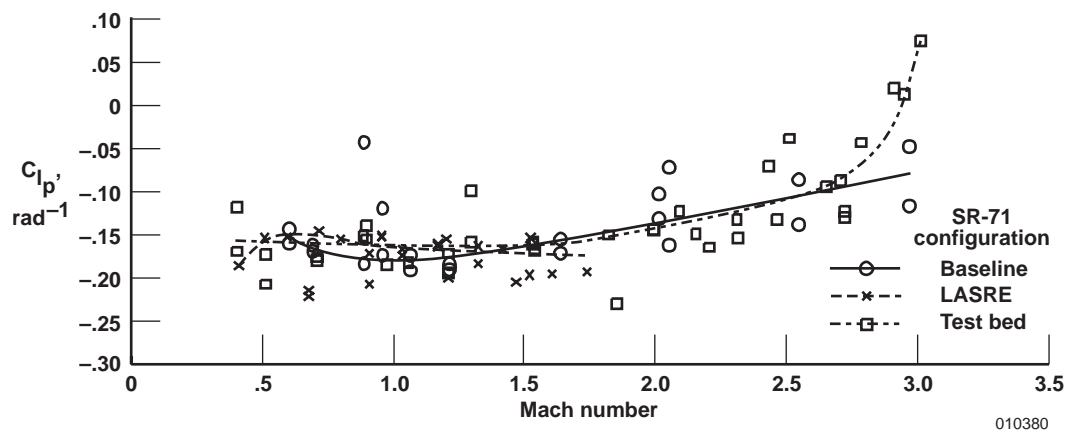
(b) C_{l_p}.

(c) C_{n_p} (moment reference at 0.25 c).

Figure 58. Flight-determined roll-rate derivatives (all three configurations).
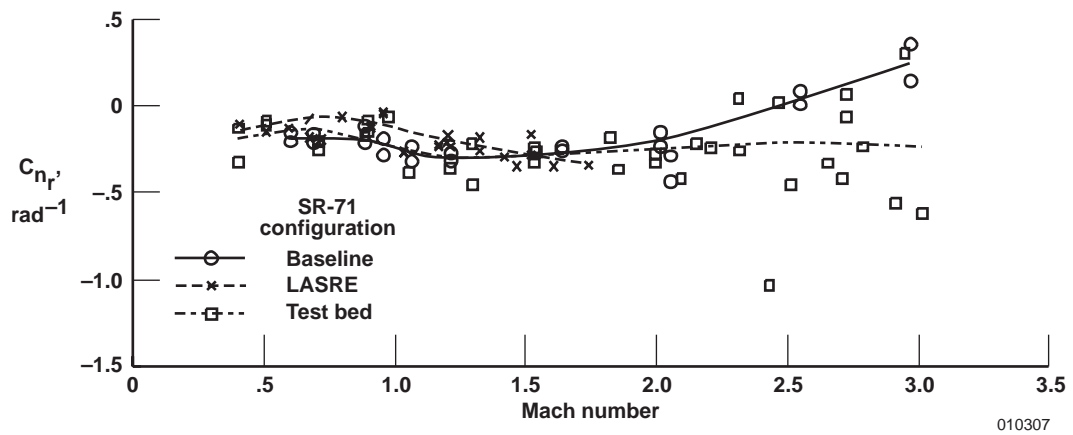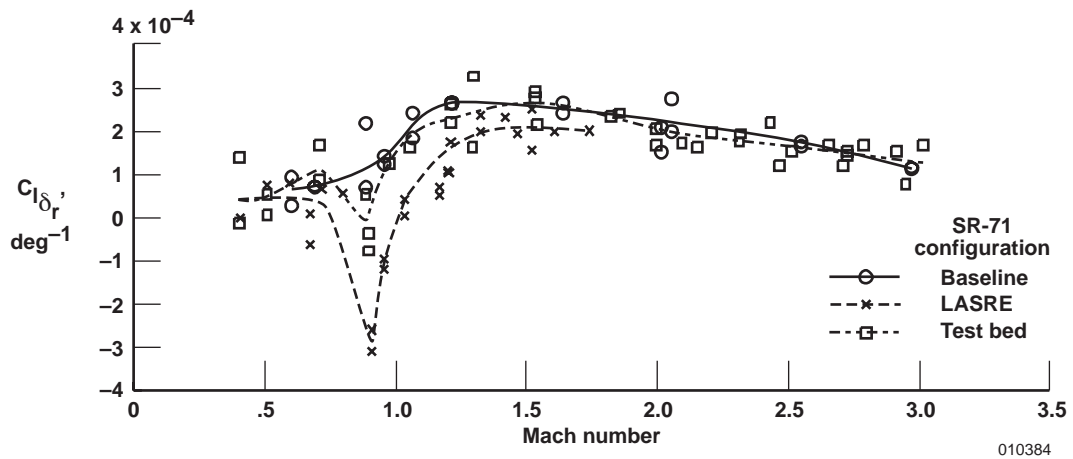
(a) C_{Y_r}.

(b) C_{l_r}.

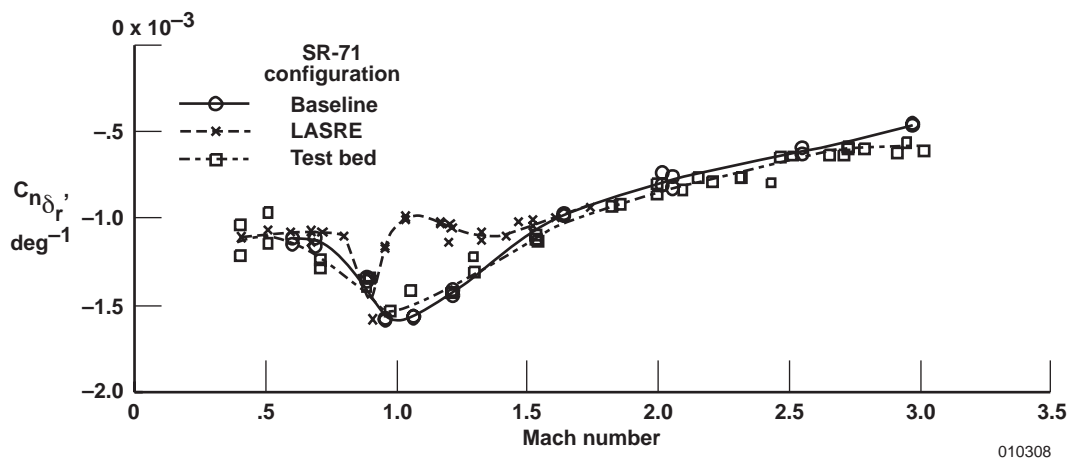
(c) C_{n_r} (moment reference at 0.25 c).

Figure 59. Flight-determined yaw-rate derivatives (all three configurations).
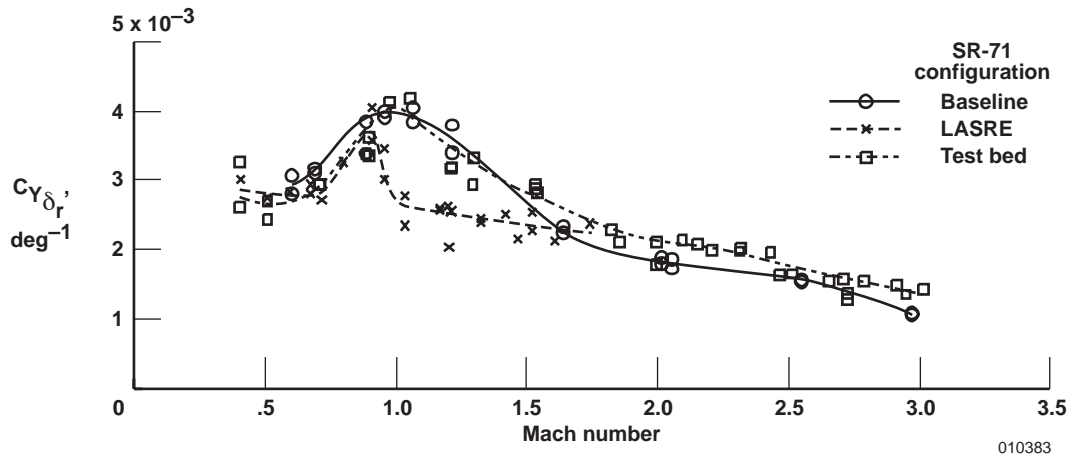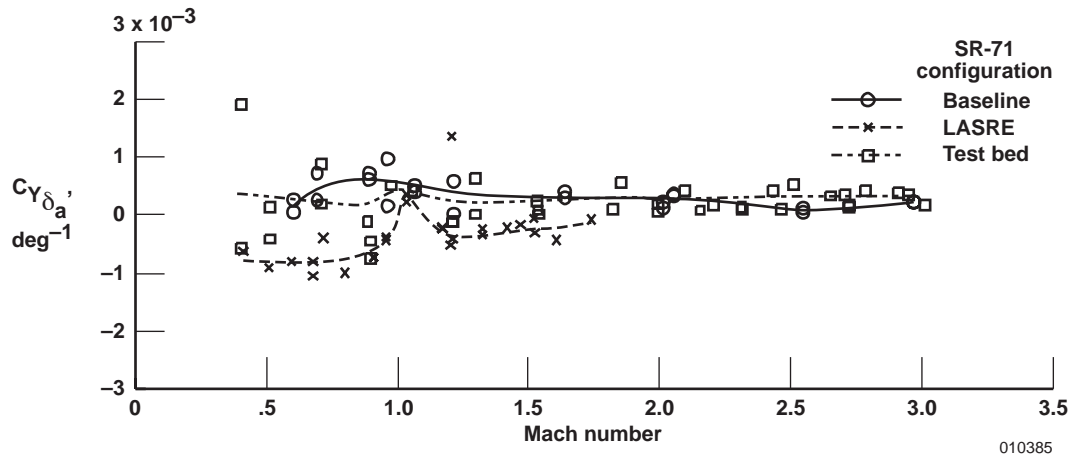
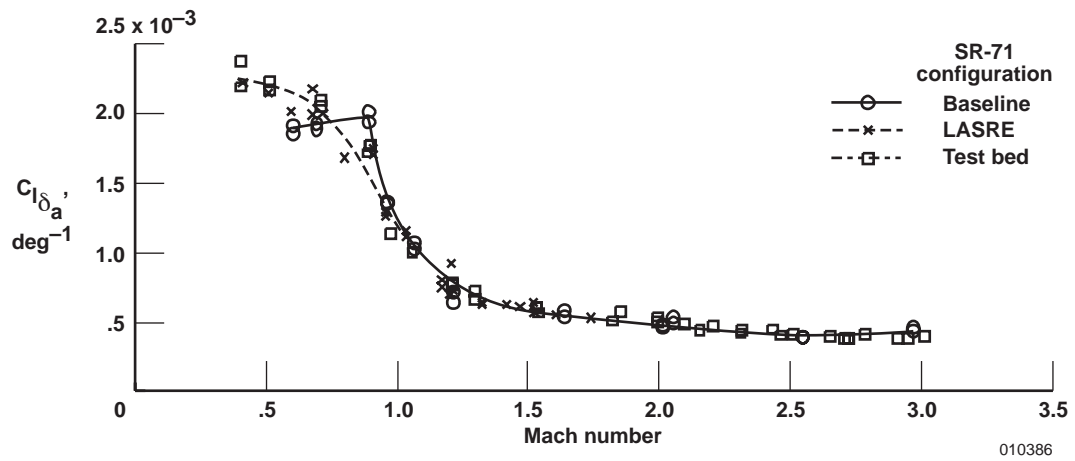(a) $C_{Y_{\delta_r}}$.

(b) $C_{l_{\delta_r}}$.

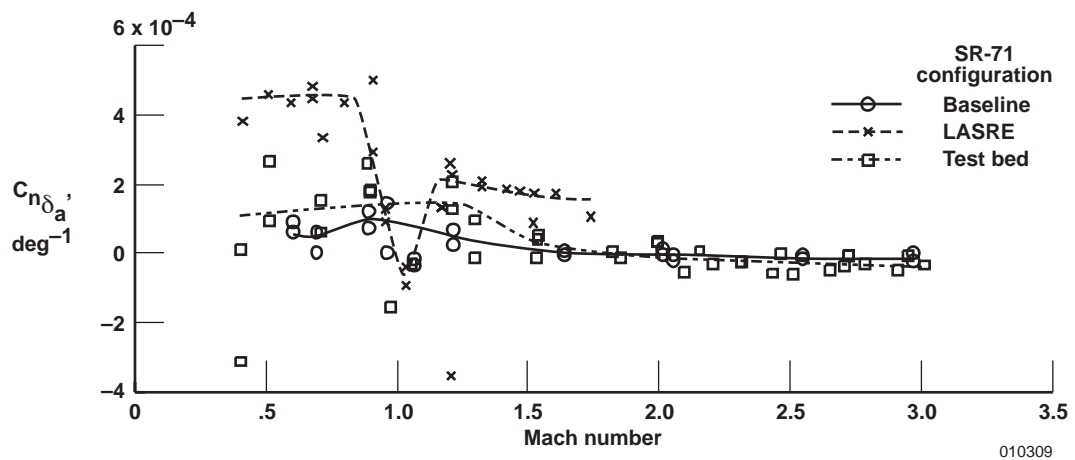(c) $C_{n_{\delta_r}}$ (moment reference at 0.25 c).

Figure 60. Flight-determined rudder derivatives (all three configurations).

(a) $C_{Y_{\delta_a}}$.

(b) $C_{l_{\delta_a}}$.

(c) $C_{n_{\delta_a}}$ (moment reference at 0.25 c).

Figure 61. Flight-determined aileron derivatives (all three configurations).

REPORT DOCUMENTATION PAGE

1. AGENCY USE ONLY (Leave blank)	2. REPORT DATE June 2002	3. REPORT TYPE AND DATES COVERED Technical Publication

4. TITLE AND SUBTITLE

Stability and Control Estimation Flight Test Results for the SR-71 Aircraft With Externally Mounted Experiments

6. AUTHOR(S)

Timothy R. Moes and Kenneth Iliff

5. FUNDING NUMBERS

WU 710-35-14-E8-OM-00-844

7. PERFORMING ORGANIZATION NAME(S) AND ADDRESS(ES)

NASA Dryden Flight Research Center
P.O. Box 273
Edwards, California 93523-0273

8. PERFORMING ORGANIZATION REPORT NUMBER

H-2465

9. SPONSORING/MONITORING AGENCY NAME(S) AND ADDRESS(ES)

National Aeronautics and Space Administration
Washington, DC 20546-0001

10. SPONSORING/MONITORING AGENCY REPORT NUMBER

NASA/TP-2002-210718

11. SUPPLEMENTARY NOTES

12a. DISTRIBUTION/AVAILABILITY STATEMENT

Unclassified—Unlimited
Subject Category 08

This report is available at http://www.dfrc.nasa.gov/DTRS/

12b. DISTRIBUTION CODE

13. ABSTRACT (Maximum 200 words)

A maximum-likelihood output-error parameter estimation technique is used to obtain stability and control derivatives for the NASA Dryden Flight Research Center SR-71A airplane and for configurations that include experiments externally mounted to the top of the fuselage. This research is being done as part of the envelope clearance for the new experiment configurations. Flight data are obtained at speeds ranging from Mach 0.4 to Mach 3.0, with an extensive amount of test points at approximately Mach 1.0. Pilot-input pitch and yaw-roll doublets are used to obtain the data. This report defines the parameter estimation technique used, presents stability and control derivative results, and compares the derivatives for the three configurations tested. The experimental configurations studied generally show acceptable stability, control, trim, and handling qualities throughout the Mach regimes tested. The reduction of directional stability for the experimental configurations is the most significant aerodynamic effect measured and identified as a design constraint for future experimental configurations. This report also shows the significant effects of aircraft flexibility on the stability and control derivatives.

14. SUBJECT TERMS

Control derivatives, Maximum likelihood estimates, Parameter identification, SR-71, Stability derivatives

15. NUMBER OF PAGES

94

16. PRICE CODE

A03

17. SECURITY CLASSIFICATION OF REPORT	18. SECURITY CLASSIFICATION OF THIS PAGE	19. SECURITY CLASSIFICATION OF ABSTRACT	20. LIMITATION OF ABSTRACT
Unclassified	Unclassified	Unclassified	Unlimited